The Investigation of the Electronic Properties of Si Based Heterojucntions: a First Principle Study of a-Si:H/c-Si and GaP/Si Heterojunctions

by

Reza Vatan Meidanshahi

A Dissertation Presented in Partial Fulfillment
of the Requirements for the Degree
Doctor of Philosophy

Approved November 2018 by the
Graduate Supervisory Committee:

Stephen M. Goodnick, Chair
Dragica Vasileska
Stuart Bowden
Christiana Honsberg

ARIZONA STATE UNIVERSITY

May 2019

ABSTRACT

In this dissertation, I investigate the electronic properties of two important silicon(Si)-based heterojunctions 1) hydrogenated amorphous silicon/crystalline silicon (a-Si:H/c-Si) which has already been commercialized in Heterojunction with Intrinsic Thin-layer (HIT) cells and 2) gallium phosphide/silicon (GaP/Si) which has been suggested to be a good candidate for replacing a-Si:H/c-Si in HIT cells in order to boost the HIT cells efficiency.

In the first part, the defect states of amorphous silicon (a-Si) and a-Si:H material are studied using density functional theory (DFT). I first employ simulated annealing using molecular dynamics (MD) to create stable configurations of a-Si:H, and then analyze the atomic and electronic structure to investigate which structural defects interact with H, and how the electronic structure changes with H addition. I find that H atoms decrease the density of mid-gap states and increase the band gap of a-Si by binding to Si atoms with strained bonds. My results also indicate that Si atoms with strained bonds creates high-localized orbitals in the mobility gap of a-Si, and the binding of H atoms to them can dramatically decrease their degree of localization.

In the second part, I explore the effect of the H binding configuration on the electronic properties of a-Si:H/c-Si heterostructure using density functional theory studies of models of the interface between a-Si:H and c-Si. The electronic properties from DFT show that depending on the energy difference between configurations, the electronic properties are sensitive to the H binding configurations.

In the last part, I examine the electronic structure of GaP/Si(001) heterojunctions and the effect of hydrogen H passivation at the interface in comparison to interface mixing, through DFT calculations. My calculations show that due to the

heterovalent mismatch nature of the GaP/Si interface, there is a high density of localized states at the abrupt GaP/Si interface due to the excess charge associated with heterovalent bonding, as reported elsewhere. I find that the addition of H leads to additional bonding at the interface which mitigates the charge imbalance, and greatly reduces the density of localized states, leading to a nearly ideal heterojunction.

To my dear family

ACKNOWLEDGEMENTS

I would like to express my sincere gratitude to my adviser and mentor, Prof. Stephen M. Goodnick for his appreciable patience and support. I am deeply indebted for his guidance and encouragement that helped me a great deal in the completion and success of this study. I would like also to thank my committee members, Prof. Dragica Vasileska, Prof. Stuart Bowden and Prof. Christiana Honsberg, for their invaluable comments. I also wish to thank Morteza Moghimi and Ebrahim Hashemi Amiri, without them I would not have such colorful memories to cherish. Last but not least, I would like to thank my parents for their unconditional love and sustained support which was my main source of motivation in the face of challenges.

TABLE OF CONTENTS

CHAPTER Page

CHAPTER Page

LIST OF TABLES

LIST OF FIGURES

Figure Page

Figure Page

LIST OF ACRONYMS

3D Three Dimensional

a-GaP Amorphous GaP

a-Si Amorphous Silicon

a-Si:H Hydrogenated Amorphous Silicon

c-Si Crystalline Silicon

CVD Chemical Vapor Deposition

DFT Density Functional Theory

DOS Density of States

EDOS Electronic Density of States

EPE Electrostatic Potential Energy

FB Floating Bond

FET Field Effect Transistors

GGA Generalized Gradient Approximation

HBT Heterojunction Bipolar Transistors

HIT Heterojunction with Intrinsic Thin Layer

IBC Integrated Back Contact

IDOS Integrated Densities of States

IPR Inverse Participation Ratio

ITRPV International Technology Roadmap for Photovoltaic

KS Kohn-Sham

LCOE Levelized Cost of Electricity

LDA Local-Density Approximation

LED Light Emitting Diodes

LPE Liquid Phase Epitaxy

MBE Molecular Beam Epitaxy

MD Molecular Dynamics

MOCVD Metalorganic Chemical Vapor Deposition

MOS Metal Oxide Semiconductor

PDOS Projected Densities of States

PECTD Plasma Enhanced Chemical Transport Deposition

PV Photovoltaics

RDF Radial Distribution Function

RF Radio Frequency

SB Strained Bond

SHJ Silicon Heterojunction

SPE Solid Phase Epitaxy

SWE Staebler-Wronski Effect

VPE Vapor Phase Epitaxy

XC Exchange and Correlation

Chapter 1

SILICON BASED HETEROJUNCTION SOLAR CELL TECHNOLOGY

With a global market share above 90%, crystalline silicon (c-Si) based photovoltaics (PV) is by far the most important solar cell technology today. The implementation of new concepts, advanced cell technologies and the use of improved materials in c-Si solar cells could result in cheaper and more universal solar power generation products which are able to compete with and replace fossil energy sources. While costs associated with cell processing typically account for less than 20% of the total module cost and only about 10% at the system level [1], increasing the power conversion efficiency of the solar cell offers a direct pathway to further reducing the levelized cost of electricity (LCOE) [9, 10]. One of the best strategies which has demonstrated a great potential in improving the efficiency is the use of heterojunctions with Si. In this regard, a-Si:H/c-Si heterojunction solar cells have achieved the world efficiency record for Si solar cells of 26.6% [11]. In this chapter, we first briefly discuss advanced concepts in improving silicon solar cell technology. We then specifically concentrate on the idea of increasing the conversion efficiency of silicon solar cells by employing novel heterojunction designs, tandem multi-junction architectures, and carrier-selective passivating contact schemes and, finally we explain the motivation of our work in the context of c-Si heterojunction solar cells. The reader who is interested in more details in the status and perspective of all aspects of crystalline silicon solar cell technology is refered to several good reviews by Battaglia, Saga, Glunz, and Frischknecht [2, 12–14].

1.1 Approaches

The topics within the value chain of Silicon solar cells are split into three areas: materials, processes, and products:

Materials: Reducing the consumption or replacing of some materials is necessary in order to ensure availability, avoid environmental risks, reduce costs, and increase efficiency. Price development plays a major role in making PV-generated electricity competitive with other renewable and fossil sources of energy.

Processes: New technologies and materials, and highly productive manufacturing equipment, are required to reduce production costs. By providing information on key production figures, as well as details about processes designed to increase cell efficiency and module power output, this roadmap constitutes a guide to new developments and aims to support their progress. The section on processes identifies manufacturing and technology issues for each segment of the value chain. Manufacturing topics center on raising productivity, while technological developments aim to ensure higher cell and module efficiencies.

Products: Each part of the value chain has a final product. The product section therefore discusses the anticipated development of key elements such as ingots, wafers, c-Si solar cells, modules and PV systems over the coming years.

Here we only discuss the products area which by our devision includes the heterojunction solar cell technology.

1.2 Products

One of the most important product of todays wafer market for c-Si solar cell manufacturing is mono-crystalline silicon solar cells. Monocrystalline solar panels have the highest efficiency rates since they are made out of the highest-grade silicon. On October 2015, SolarCity announced that it has developed the worlds most efficient solar panels. The new panels convert more than 22% of sunlight into electricity. Just days later Panasonic announced it had trumped that achievement, with a new world record module conversion efficiency of 22.5% on a commercial sized prototype using solar cells based on mass production technology. The test results were confirmed by

the Japanese National Institute of Advanced Industrial Science and Technology. The 72-cell, 270-watt prototype incorporates newly developed enhanced technology that will eventually be scaled into volume production. However, monocrystalline solar panels are the most expensive. In recent years, improvements in polycrystalline ingot, cell and module production efficiencies have lead to polycrystalline solar panels becoming more widespread due to the benefits from costs advantages over mono Si panels. The process used to make polycrystalline silicon is simpler and costs less. The amount of waste silicon is less compared to monocrystalline. Most monocrystalline panel manufacturers that still make are forced to increase performance in order to compete with polycrystalline panels. One approach to boost the performance of monocrystalline cell is employing heterojunction designs.

The silicon heterojunction (SHJ) solar cell was pioneered in the early 1990s by Sanyo (acquired in 2010 by Panasonic) and has been commercialized under the HIT trademark (heterojunction with intrinsic thin layer) [15]. Using this concept, Kaneka, Japan, achieved a cell efficiency of 25.1% in 2015. Very recently, Yoshikawa et al. [11] demonstrated a new world record efficiency of 26.6% by combining the HIT cell with interdigitated back contacts. The current edition of the International Technology Roadmap for Photovoltaic (ITRPV) predicts a mainstream market for SHJ cells with double-sided contacts [1]. Within this market, heterojunction (HIT/SHJ) cells are projected to reach significant market share over conventional mono silicon cells by 2027, as can be seen in Fig. 1.1. Similar to HIT/SHJ cells, Si-based tandem cells are also expected to appear in mass production operations after 2019.

1.3 Silicon Heterojunction Solar Cells

A schematic of a silicon heterojunction cell is depicted in Fig. 1.2. The silicon heterojunction concept is based on two critical innovations. First, it makes use of

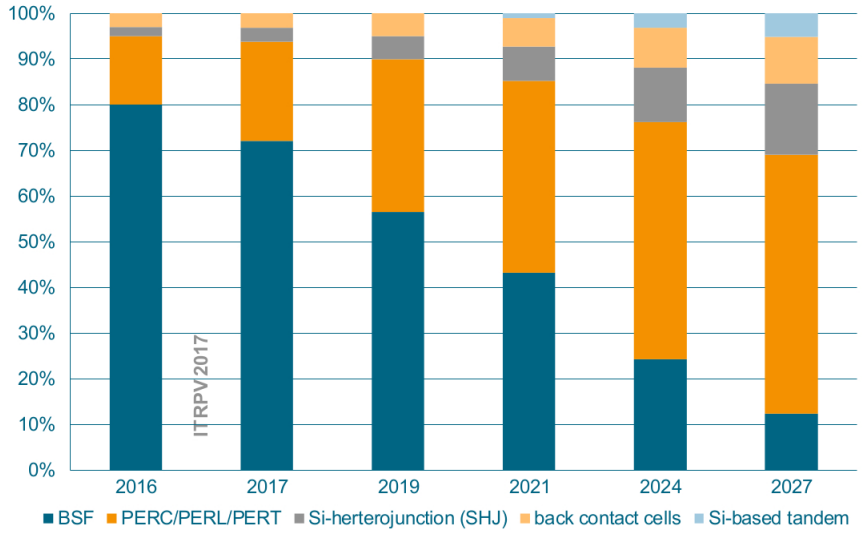

Figure 1.1: Worldwide market shares for different cell technologies [1].

a thin hydrogenated amorphous silicon layer to achieve excellent surface passivation [16, 17]. To ensure such passivation, it is critical that deposition processes be tuned to obtain atomically sharp interfaces between the wafer and buffer layers, devoid of any unintentionally grown epitaxial silicon [18–21]. Second, this thin passivating film is inserted underneath the electron-selective and hole-selective contact layers [15], yielding virtually recombination-free surfaces, even for the areas contacted by the metal electrodes (Fig. 1.2). This translates into a very high open-circuit voltage [22], with values as high as 750 mV, obtained by Panasonic for a two-side-contacted cell with an efficiency of 24.7% [23]. Note that the theoretical, Auger-limited open-circuit voltage for a wafer with similar thickness (110 um), is 761 mV [24, 25], underlining the remarkable passivation achieved with this technology.

The fabrication process sequence starts with surface texturing and cleaning, followed by passivation of both sides of the silicon wafer with a thin layer of intrinsic hydrogenated amorphous silicon [26]. These films are usually deposited by plasma-enhanced chemical vapor deposition and are only about 5 nm in thickness

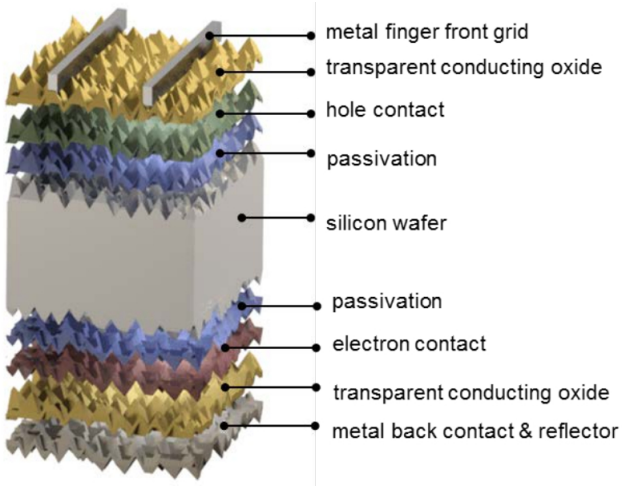

Figure 1.2: Schematic of the components of a silicon heterojunction cell [2].

[19, 27, 28]. These films can be considered the heart of the silicon heterojunction solar cell, as they yield very effective passivation, while simultaneously being transparent for charge carrier transport. As a consequence, their electronic [29–32] and microstructural [33, 34] properties as well as their deposition processes [35–38] have been extensively studied. Rather than relying on dopant diffused regions of the same material (crystalline silicon) to separate the charge carriers, in silicon heterojunction technology such separation is achieved by a combination of doping and use of a wider band gap material, producing nearly ideal carrier-selective contacts. To form these, doped amorphous silicon layers with thicknesses of about 10 nm are deposited on top of the intrinsic layer. Boron is used as a dopant to obtain a p-type layer for transporting the holes, and phosphorus is used to obtain an n-type layer for conducting the electrons. Both dopants are incorporated into the films by adding relevant precursor gasses during film deposition, such as trimethylboron and phosphine. Direct deposition of the doped layers on the crystalline silicon surface degrades passivation, as dopant incorporation generates a significant amount of recombination-active defects in amorphous silicon, explaining the need for intrinsic buffer layers in this technology

[39, 40]. The doped layers may alter the surface passivation when deposited on the intrinsic buffer layers because they can change the carrier concentrations inside the wafer (this is evidenced in Fig. 1.3 by a bending of the energy bands in equilibrium) [41]. Interestingly, the silicon heterojunction process sequence can be easily applied to either n-type or p-type wafers [42], with n-type wafers delivering slightly higher efficiencies due to the fact that such surfaces are usually easier to passivate than their p-type counterparts. With this technology it is also fairly straightforward to change the polarity of the device [43, 44]. Due to the asymmetric band offsets at the amorphous/crystalline silicon interface, holes usually face a larger barrier than electrons, potentially hindering efficient carrier collection (see Fig. 1.3). Full-area contacts are formed by sputtering an indium tin oxide transparent front electrode. As the lateral conductivity of the doped amorphous silicon films is relatively poor, lateral current transport to the metal fingers needs to be provided by the transparent conductive oxide film, requiring a relatively low sheet resistivity of about 50-100 Ω/m, similar to that of a typical diffused region in classic crystalline silicon solar cells. Thanks to its low refractive index of about 2, this layer is also well suited as an antireflection coating (sometimes in conjunction with a second layer of magnesium difluoride to further minimize reflection losses). The transparent conductive oxide is also important to guarantee a sufficiently low contact resistivity, explaining its use at the rear side as well. There, it also helps to reduce the parasitic plasmonic absorption of light at the silver back contact, in case this metal is deposited as a blanket layer. The cells are finalized by screen printing a silver finger and busbar grid on the front side; copper-plated metallization is an attractive alternative [45–47].

Compared to the IBC concept, which produces a current density of 41.8 mA/cm^2 , the silicon heterojunction cell from Kaneka, featuring contacts on opposite sides, delivers a slightly lower short-circuit current density of 40.8 mA/cm^2 .

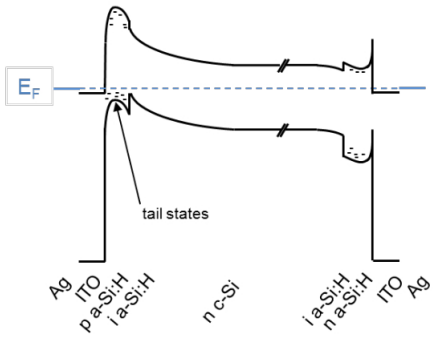

Figure 1.3: Energy band diagram of a silicon heterojunction solar cell [2].

These losses are caused not only by grid shading, but also by parasitic absorption in the window layers. At the front side, parasitic absorption in the doped and intrinsic amorphous silicon layers with a relatively narrow band gap of about 1.8 eV represents the main contribution to current losses in the blue and ultraviolet part of the spectrum. In the red and infrared part of the spectrum, current is lost mainly through free-carrier absorption in the front and back indium tin oxide electrodes as well as through parasitic plasmonic absorption in the silver back reflector. Several approaches to improve the short-circuit current of silicon heterojunction cells have been explored, including the replacement of the doped amorphous silicon layers by wider band gap hydrogenated amorphous silicon oxide [48, 49] or silicon carbide layers, transparent [50] or by replacing the indium tin oxide with higher mobility conductive oxides such as hydrogen-doped indium oxide [51, 52], tungsten-doped indium oxide [53], cerium-doped hydrogenated indium oxide [54], and amorphous indium zinc oxide [55]. While such transparent conductive oxides clearly lead to an increase in the current density, the use of hydrogenated amorphous silicon oxide or silicon carbide often results in a reduced fill factor, and neutralizes the gains in short-circuit current. In general, fill factor losses related to transparent conductive oxides are due to a suboptimally matched work function [56, 57], or to increased sheet or contact resistances between the transparent conductive oxide and the doped amorphous sili-

con layers [58]. Transparent conductive oxides typically exhibit n-type conductivity and consequently readily form an Ohmic contact to n-type hydrogenated amorphous silicon. As p-type transparent conductive oxides suffer from relatively low hole mobilities caused by the large effective hole mass of most oxides [59], contact to p-type amorphous silicon is also commonly established with n-type transparent conductive oxides [60]. This recombination junction requires a relatively high carrier concentration in the oxide at least near the interface with p-type amorphous silicon to enable tunneling of carriers across the interface and avoid fill factor losses. The deposition process for transparent conductive oxides, such as sputtering, may also lead to undesired performance losses [61]. These combined factors motivate the engineering of gently deposited, well-tuned transparent conductive oxides, possibly as multi-layer stacks [62]. An alternative approach has made use of a perforated insulating magnesium difluoride layer between the amorphous silicon and transparent indium oxide back electrode, which improves the infrared response significantly as the reflection is increased due to higher refractive index contrast [63]. Finally, conformal atomic layer deposition of transparent conducting oxides on black silicon has been demonstrated [64], possibly offering optical advantages. It remains to be seen whether similarly conformal amorphous silicon layers can be produced, yielding efficient devices.

1.4 Motivation of the Present Work

Since HIT cells have demonstrated the world record efficiency among Si based solar cells, we initially aim to investigate the electronic and microstructural properties of a-Si:H at the heart of HIT cells. As mentioned previously, one of the key roles of a-Si:H in HIT cells is providing an excellent passivation layer which results in removing midgap states. Due to its amorphous nature, an a-Si:H layer by itself could contain many defect and midgap states which also negatively affect its transparency and its stability under light illumination. Therefore, in the first step of our project which is

discussed in Chapter 4, we investigate the electronic properties of a-Si:H and the microstructural origin of the possible defect and midgap states in its electronic structure using ab initio methods combined with molecular dynamics simulation. This subject is fundamentally important for photovoltaic applications. In the second step of the project which is discussed in Chapter 5, we investigate the effect of a-Si:H layers on c-Si substrates as a passivation layer. We therefore examine the electronic structure of a-Si:H/c-Si heterojunction using methods based on molecular dynamics (MD) and density functional theory (DFT). We check different H configuration in the a-Si:H layer to see if an ideal a-Si:H/c-Si heterojunction without any interface and midgap states can be obtained. The final step in the project which is discussed in Chapter 6 is to see if an ideal heterojunction can be obtained by replacing a-Si:H in a-Si:H/c-Si heterojunction with a GaP layer. GaP has been suggested as a good candidate for the replacement of a-Si:H in a-Si:H/c-Si heterojuntions mainly due to its close lattice match to silicon and its large band gap. These two properties could potentially make GaP a good passivation layer and a transparent layer on top of c-Si, respectively. To check if GaP is really able to behave as a passivation and transparent layer on top of c-Si, we calculate the electronic structure of GaP/Si heterojunction using DFT and compare the results with the electronic structure of a-Si:H/c-Si heterojunctions as a nearly ideal heterojunction. Before discussing our results, in the next two chapters, we give a brief introduction of the electronic structure of semiconductor heterojunctions and the method that we used in this dissertation for calculating the electronic structure.

Chapter 2

SEMICONDUCTOR HETEROJUNCTION

A heterojunction is a junction between two different materials that differ due to having either different atomic composition or different atomic structure. GaP/Si and a-Si/c-Si are good examples of these two types of heterojunctions. In the case of a semiconductor heterojunction, the two semiconductor have unequal band gaps as opposed to a semiconductor homojunction. The earliest electronic devices were mostly based on homojunctions whose electronic properties were engineered by tunning the spatially concentration of dopant impurities. These so-called homojunction devices include bipolar transistors, MOS transistors, and diffused homojunction solar cells which approached their practical efficiency limits. In the last decades, heterojunction devices have gained a tremendous attention in many different applications including lasers, solar cells, light emitting diodes (LED), heterojunction bipolar transistors (HBT) and field effect transistors (FET), due to their electronic and optical properties. In laser applications, heterojunctions are used in order to efficiently confine carriers in the optical cavity corresponding to a small direct band gap material sandwiched between two larger band gap materials, so that lasing can operate at low temperature with low threshold current. Semiconductor diode lasers used in CD and DVD players and fiber optic transceivers are manufactured based on alternating layers of different III-V and II-VI semiconductors to form heterojunction lasing. In transistors applications, heterojunctions provide high electron mobility allowing transistors operate at significantly higher frequencies. The modulation doping profile with the proper band alignment gives rise to extremely high electron mobilities by creating a two dimensional electron gas within a dopant free region where very little scattering can occur. In solar cell applications, heterojunctions cause more absorp-

tion in different part of solar spectrum due to providing several band gaps and also result in better charge separation due to providing strong driving fields across the solar cell. One of the most important factors in a semiconductor heterojunction solar cells, is its interface. In principle, an interface is characterized by lattice mismatch, band offset, band bending, and interface states. These parameters significantly affect the charge transport across the interface and interface recombination which in turn affects the efficiency of the solar cell. This chapter gives a brief introduction of these four parameters (lattice mismatch, band offset, band bending, and interface states) in heterojunctions, especially Si based heterojunctions and their effect on heterojunction solar cells functionality. Since the present work is mostly mostly related to two specific heterojunctions, GaP/Si and a-Si/c-Si for solar cell applications, the end of this chapter is devoted for introducing their constituent semiconductors.

2.1 Atomic Structural Properties of Heterojunctions: Lattice Matched Heterojunctions

Heterojunction functionality relies on differences in the electronic structure of the constituent semiconductors. When a free charge carrier reaches a heterojunction interface, it should be ideally affected only by this electronic structure difference and should not be trapped or scattered by the interface. In general, this means that the atomic bonding of the constituent semiconductors needs to be kept the same without interruption across the heterojunction. This condition, in turn, will be partially met if both the atomic arrangement and atomic spacing of the constituent semiconductors are essentially identical. Therefore, an ideal heterojunction consists of two semiconductors with the same lattice structure and the same lattice constant in which the atoms participating in the interface change abruptly. This type of heterojunction is called lattice matched heterojunction. In a lattice matched heterojunction, the interface lacks misbonded or strained bonded atoms which are the main source of interface

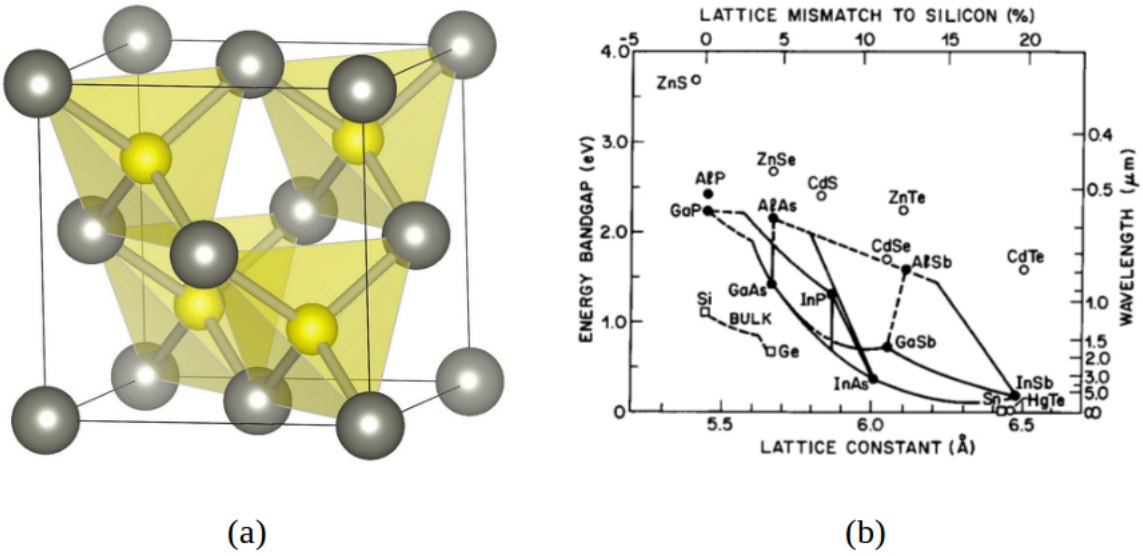

Figure 2.1: (a) A zinc blende structure (b) Plot of the semiconductor lattice constant versus band gap for common semiconductors mostly crystalized in zinc blende or diamond structure [3].

states.

The zinc blende or diamond (if both basis atoms are identical) lattice structure is one of the most abundant semiconductor crystal structures. Most III-V (GaP, AlP, GaAs, InP), some of II-VI (ZnS, ZnTe, CdTe) binary compounds, and group IV semiconductors (Si, Ge and their alloys) are crystallized in zinc blende or diamond lattice structure. The unit cell of the zinc blende lattice is illustrated in Fig. 2.1. In this structure, cations (gray spheres) are arranged in a face centered cubic unit cell. The length of the edge of the unit cell is the non-primitive cubic lattice constant. Anions (yellow spheres) occupy four tetrahedral sites (out of 8 available tetrahedral sites) with a fourfold coordination number. If this unit cell is repeated in 3D space, each cation is surrounded with four anions in a tetrahedral geometry. Therefore, cations and anions are present in equivalent positions in the zinc blende structure. A diamond structure will occur when onions and cations in zinc blende structure are replaced with identical atoms. The most common semiconductor, Si, crystallizes

in the diamond structure with a lattice constant of 5.43Å. Therefore, for an ideal Si heterojunction, a semiconductor deposited on a Si substrate should have either a zinc blende or a diamond structure with a lattice constant close to 5.43Å. Ideal semiconductors for fabricating high quality heterojunctions are the ones lying along a vertical line in Fig. 2.1b. Historically, an ideal heterojunction occurs between GaAs and AlAs. These materials not only contain one constituent atom in common but also are very nearly lattice-matched with a lattice mismatch of only 0.13%. Beyond that, GaAs and AlAs can be combined to realize the ternary alloy, $Al_xGa_{1-x}As$, which provides a range of bandgaps from 1.5 to over 2 eV. A Si-based analog of GaAs/AlAs could be fabricated with depositing either GaP, AlP or ZnS on a silicon substrate (Fig. 2.1b).

Both lattice-matched and lattice-mismatched heterojunctions are generally fabricated using heteroepitaxial growth processes. The most established heteroepitaxial techniques which are widely used include Vapor Phase Epitaxy (VPE), Liquid Phase Epitaxy (LPE), Solid Phase Epitaxy (SPE), and Molecular Beam Epitaxy (MBE). In addition, Chemical Vapor Deposition (CVD) and Metalorganic Chemical Vapor Deposition (MOCVD) are widely used in heterojunction growth. In some important cases, the specific device design relies on combinations of various materials where the lattice mismatch between the different materials can introduce problems for device performance and the deposition processes. However, there exist various technology solutions to produce high quality materials including using buffer layers or composition grading between two lattice-mismatched semiconductors. Recently, the fabrication of high quality lattice mismatched heterojunctions using direct fusion boding methods has been reported [65].

. The examples of heterojunctions cited so far involve semiconductors with a well defined lattice structure. It is also possible to grow heterojunctions between

amorphous and crystalline materials, and such junctions were widely studied early in the development of HIT solar cells technology. The effects on lattice-mismatch are not obviously an important issue in these type of heterojunctions, since the lattice structure and lattice constant are not defined in amorphous materials. In the next section, we discuss the radial distribution function concept which can be used for describing the atomic structure of amorphous materials and the heterojunctions between amorphous and crystalline materials.

2.2 Electronic Properties of Heterojunctions

2.2.1 Band Discontinuity

One of the most important features in the study of semiconductor heterojunctions is the band discontinuity at the interface, which strongly affects charge confinement and career transport at the heterojunction. These discontinuities are the origin of the most of the useful properties of heterojunctions.

For picturing the band discontinuity, consider two semiconductors, 1 and 2, with different bandgaps E_{g1} and E_{g2}. Now, we bring them together by chemical bonding at the interface. Since the bandgaps are discrete values, it is obvious that the valence and conduction band edges will change abruptly. Now the question is how the band alignment should be at the junction. The only way to determine the correct band alignment is measuring the conduction and valence band energies with respect to a single reference. This reference can be provided by the vacuum level. The vacuum level denotes the energy of a free electron (an electron liberated from the bulk semiconductor) which is at rest with respect to the semiconductor. The required energy to kick out an electron from the bottom of the conduction band of a semiconductor to the vacuum level is called electron affinity (usually expressed in eV) and is characteristic of a semiconductor. Based on this definition, the band alignment of a heterojunction between two semiconductors can be determined by their electron

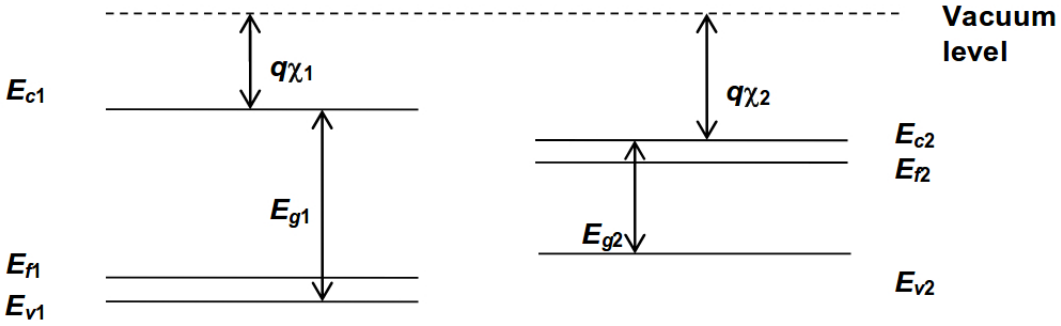

Figure 2.2: Band alignment of two typical semiconductors.

affinities, as illustrated in the Fig. 2.2. The electron affinity rule implies that the conduction band offset at a heterojunction interface is equal to the difference in the electron affinities between the two semiconductors. Based on the electron affinity rule, the conduction band offset (ΔE_c) and valence band offset (ΔE_v) are equal to $q(\chi_1 - \chi_2)$ and $\Delta E_g - \Delta E_c$, respectively.

Depending on the difference between electron affinities, three types of band alignment can be imagined in semiconductor heterojunctions. Figure 2.3 illustrates these three possible different type of band alignment which are referred as the type I, type II, and type III. In type I heterojunctions, the band gap of one of the semiconductors is entirely within the band gap of the other one. An example of type I heterojunction is GaAlAs/GaAs. Both heterojunctions studied in this thesis, GaP/Si and a-Si:H/c-Si, are type II semiconductor heterojunctions. In type II (staggered gap) heterojunctions, $E_{v2} > E_{v1}$ and $E_{c2} > E_{c1}$. This condition does not necessarily means $E_{g2} > E_{g1}$. Both the valence band edge and the conduction band edge of one of the semiconductors is higher than those of the other, therefore holes are confined in one of them, while electrons are confined in the other one. In type III (broken gap) heterojunctions, $E_{v2} > E_{c1}$. An example of a type III heterojunction is GaSb/InAs.

There are several theoretical methods that have been successfully employed

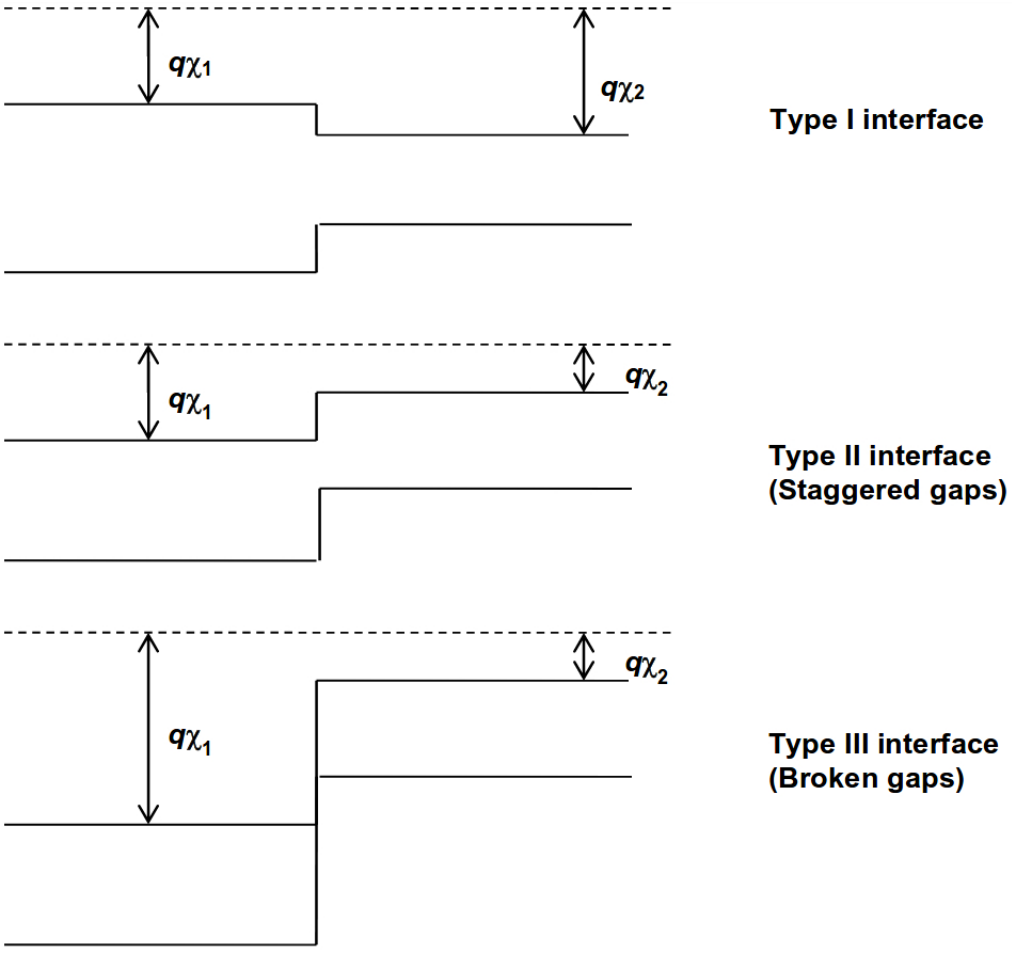

Figure 2.3: Band alignment between two semiconductors.

for calculating the band structure of an isolated semiconductor; The problem with using these methods for heterojunctions is finding a way to align the calculated band structures across the interface. One way is calculating the band structure of semiconductor A or B relative to their own average of the electrostatic potentials as reference levels (Fig. 4). Then, the valence (conduction) band offset would be the difference in the relative valence (conduction) band edges between A and B, ΔE_v (ΔE_v) in Fig. 4. The problem would therefore be solved if we are able to determine the positions of the average electrostatic potentials of A and B with respect to an absolute energy scale, e.g. with respect to the vacuum level. Here we mean the "potential energy" by

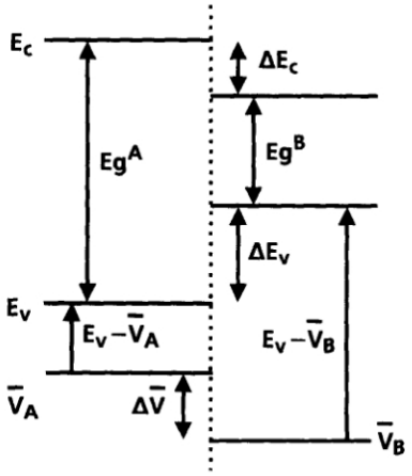

Figure 2.4: Schematic illustration of the band structure lineup problem between semiconductors A and B. The positions of the valence and conduction bands are indicated.

"energy", which is (to within a constant factor) equivalent to the potential.

It may seem that if we can perform the band structure calculations for the two semiconductors in the bulk phase, then the problem would be solved, since these calculations will give us the necessary information about the energy of $\bar{V}_A$ and $\bar{V}_B$. Unfortunately this is not the case. The fundamental problem is that it is impossible to define an absolute reference for the average potential for an infinite solid. This problem is due to the long-range nature of the Coulomb interaction [66]. The fact that the average potential in an infinite solid is not a well-defined and is often described by associating single particle-energies with "removal energies". Because in an infinite material there is nothing meaningful as "elsewhere" (e.g., a vacuum level) to kick an electron to, thus the single-particle energies in an infinite material cannot be scaled based on an absolute energy. If we have short-range interactions, the average potential of a macroscopic but finite material would not depend on the shape of the solid or surface effects, and would therefore have a well-defined thermodynamic limit. It is exactly the long-range feature of the Coulomb interaction that causes the removal

energies to be dependent on the detail atomic structure of the surface or, in the case of an interface, causes the effect of dipoles at an interface to move the energy levels throughout the semi-infinite solid on both sides. Therefore it becomes clear that a band structure calculation for an isolated semiconductor cannot provide sufficient information about the absolute value of the average potential. This argument literally reveals that, at least in principle, the details of the atomic structure near the interface affect the potentials far away, and hence the band-lineup. In this thesis we will show how the detailed atomic structure at the interface strongly affects the band line-up of a-Si:H/c-Si and GaP/Si heterojunctions.

In order to solve the heterojunction problem, an obvious approach is to carry out calculations on a system which contains both semiconductors joined at the junction. This approach guarantees that the electrostatic potentials of both semiconductors are calculated with respect to the same reference, and provides the possibility to directly extract $\Delta\bar{V}$ and therefore band discontinuities. Several theoretical approaches have addressed the problem from this perspective, with great success for a number of very well-known interfaces. These theoretical approaches can be categorized in to four classes: (1) fully self-consistent *ab initio* calculations; (2) linear -response theory; (3) calculations based on simplified, approximate Hamiltonians; and (4) simple models. Here, we only discuss *ab initio* approaches which are used in this thesis in order to calculate the band offsets.

"*Ab initio*" or "first-principles" methods are methods that solve the quantum-mechanical equations for a many body system, without any experimental input. DFT is an *ab initio* technique that has been widely used in the study of semiconductor heterojunctions. The DFT method aims to calculate the ground-state energy of a many body system using self-consistent solution of a one-particle Schrödinger equa-

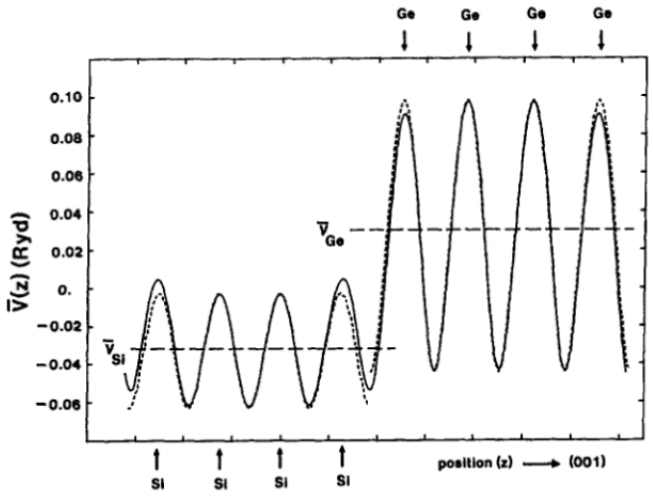

Figure 2.5: Variation of the plane-averaged potential across a Si-Ge(001) interface, calculated in a 4 + 4 superlattice with unstrained Si and strained Ge [4].

tion [67, 68]. Electron-electron interactions are considered using an exchange and correlation (XC) functional to the Hartree potential; the XC functional is described as a functional of the charge density of the system. In the local-density approximation (LDA), the XC functional is simplified to a function of the local charge density of the system. Performing the ground-state energy calculation of a given system is an crucial aspect of the study of junctions, because finding a stable structure is the first step in the theoretical and computational analysis. This step is refereed to the optimization step. After optimizing, DFT calculations can provide detailed information about the electronic structure of the system, and consequently provide information about band offsets.

An example of DFT results for the band-lineup is illustrated in Fig. 2.5 for the case of a SiGe heterojunction. For the purpose of calculating the band-lineup, we only focus on the behavior of the potential as we move along the axis perpendicular to the interface (z axis); the two other coordinates (x,y) are eliminated by averaging

in planes parallel to the interface:

$$\bar{V}_z = \frac{1}{S}\int_S V(x,y,z)dxdy \tag{2.1}$$

where S is the area of the plane parallel to the interface in the considered unit cell. We are therefore dealing with a z-dependent function, which is still periodic variations in the z direction. As illustrated in Fig. 2.5, this function quickly recovers its "bulk-like" behavior in both of the two semiconductors building the junction as we move away from the interface; however, the positions of the average potential are shifted in the bulk-like regions with respect to one another, giving exactly the values of $\bar{V}_A$ and $\bar{V}_B$ needed for obtaining the band-lineup. A similar procedure for determining band offsets is followed in XPS experiment (see Section 2.3). In XPS, typically, the energy differences between two core levels is measured across the junction; in another XPS experiment, the energy difference between the valence-band maximum and the core levels in each bulk semiconductor are measured. The core level difference is then used to line up the valence bands and obtain the band offsets.

It is important to note that in DFT, the calculated eigenvalues are not necessarily quasiparticle energies. This deficiency of DFT cause the well-known failure of DFT to correctly predict the band gaps. It is therefore very important to realize that corrections beyond DFT may be necessary to compute the exact band positions (relative to the average electrostatic potential). We also acknowledge, however, that the computed potential lineup value ($\Delta\bar{V}$) depends only on the charge density of the heterojunction, and because it is a ground-state property, DFT is able to give us reliable results in the case of the valence band offset.

2.2.2 Electronic Interface States

The general pattern of the chemical bonds in the bulk is perturbed at the interface of a semiconductor heterojuction. This perturbation cause the formation of unsaturated

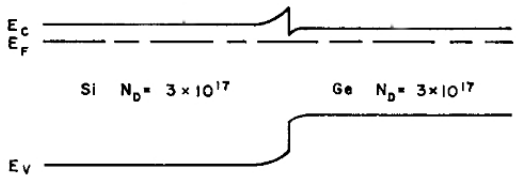

Figure 2.6: The energy band diagram of a Ge/Si heterojunction in equilibrium. An electron affinity difference of 0.18 eV is assumed and interface state effects are ignored [5].

or strained bonds at the interface, and subsequently the formation of highly localized electronic interface states that mostly appear in the forbidden gap of the electronic structure. In this section, we briefly discuss interface states and their effects on the electronic properties of the heterojunction.

2.2.2.1 Electronic Interface State Effects on the I-V Characteristics of a Heterojunction

The energy bands at the interface are free to move up or down due to the interface state density distribution,and occupancy. Figure 2.6 illustrates the band diagram of a Ge/Si heterojunction without interface states at the junction. The band diagram is obtained by the requirement that the net charge be equal to zero. Since the electrostatic potential should be continuous [69], the usual Schottky boundary condition restricts the conduction band to be discontinuous by the amount of the electron affinity difference of the two semiconductors. The positive charge in the depletion region of Si needs to be equal to the negative charge in the accumulation region of Ge. If, however, the junction contains interface states, the electronic bands at the junction are able to move up or down since the necessary charges can be supplied by electrons or holes in the interface states. The conduction and valence band discontinuities are still the same; however, the height of the conduction and valence band edge at the interface is clearly determined by the interface states distribution. As an example, Fig. 2.7(a) illustrates the energy band diagram of the same Ge-Si heterojunction

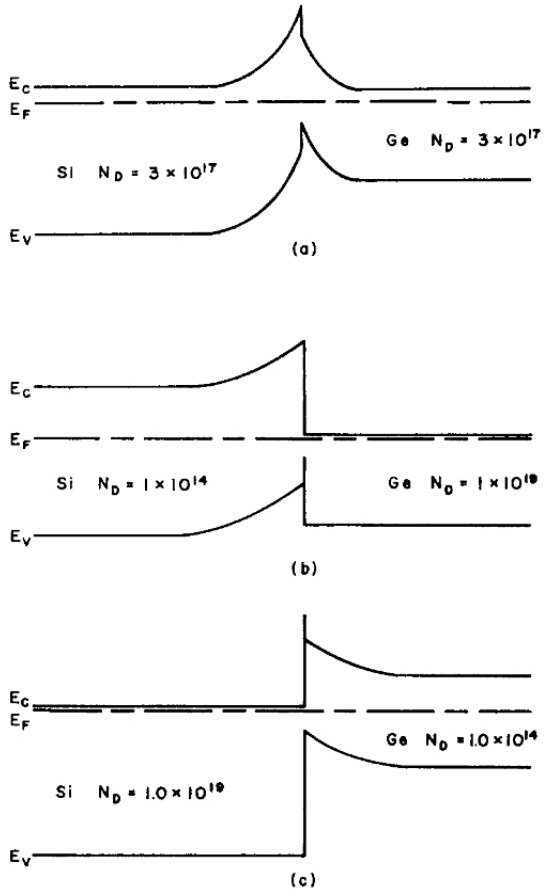

Figure 2.7: Equilibrium energy band diagrams at Ge/Si heterojunctions including interface states with different doping [5].

as Fig. 2.6, but with a distribution of interface states similar to that of a clean Si surface. It is observed that both sides of the interface can be depleted due to the acceptor nature of the interface states. The effect of different doping levels on the band bending are also of interest. Figure 2.7(b, c) illustrates the band diagram of a Ge/Si heterojunction for the same values of $\Delta\chi$ and interface state distribution as Fig. 2.7(a).

Any dense set of interface states in the band gap of the semiconductor heterojunction would create the double depletion (accumulation) similar to that discussed here. An $n-n$ or $p-p$ heterojunction with double depletion may show rectification

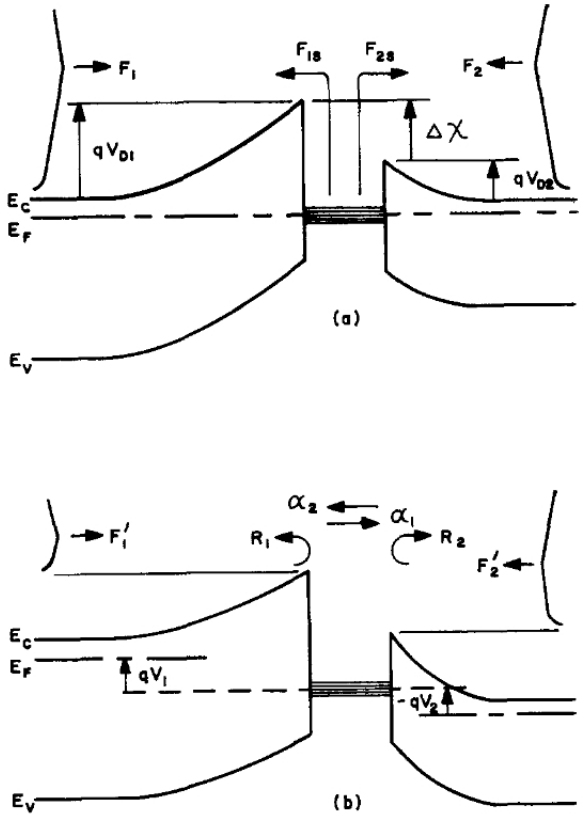

Figure 2.8: Magnified energy band diagrams of an n-n heterojunction with interface states. (a) a definition of various fluxes; (b) voltage division across the structure [5].

in both directions, or saturation in either direction, like two metal-semiconductor diodes that are joined from metal to metal. In fact, if all the current flows from one semiconductor to the interface states at another semiconductor, the structure can not be indistinguishable from two metalsemiconductor contact (or surface-state semiconductors) that are joined externally in series. However, current might flow from one semiconductor to the other without being in equilibrium with the interface states. Therefore, more general IV characteristics will be derived.

The band diagram of an n-n heterojunction with a magnified interface region is shown in Fig. 2.8. Let's assume that the interface states are located in a thin layer placed between the two depletion regions. In Fig. 2.8(a), F_{1S} and F_{2S} are electron

fluxes from the interface states into the bulk regions. F_1 and F_2 are the bulk electron fluxes toward the barriers given by:

$$\begin{aligned} F_1 &= \frac{\bar{C}_1}{4} n_1 \\ F_2 &= \frac{\bar{C}_2}{4} n_2 \end{aligned} \tag{2.2}$$

in which n_1 and n_2 are the free electron concentrations and $\bar{C}_1$ and $\bar{C}_2$ the mean thermal velocities of the electrons in regions (1) and (2). The fluxes $F_1^{'}$ and $F_2^{'}$ are those of F_1 and F_2 sufficiently energetic to overcome the barriers in region (1) or region (2). Using Boltzmann statistics, $F_1^{'}$ and $F_2^{'}$ can be computed as follow:

$$\begin{aligned} F_1^{'} &= F_1 exp[-q(V_{D1} - V_1)/kT] \\ F_2^{'} &= F_2 exp[-q(V_{D2} - V_2)/kT] \end{aligned} \tag{2.3}$$

The total voltage drop at the junction is $V_j = V_1 - V_2$. When an electron reaches the interface and is able to pass the barrier, it might reflect from the interface or it might be transmitted through the interface. Assume that R_1 and R_2 are the reflection coefficients at the interface for the fluxes $F_1^{'}$ and $F_2^{'}$, and α_1 and α_2 are the transmission coefficients for the flux of $(1 - R_1)F_1^{'}$ and $(1 - R_2)F_2^{'}$. Then the total fluxes F_I and F_{II} to the region (1) and to the region (2), respectively, are:

$$\begin{aligned} F_I &= F_1^{'}(1 - R_1) - F_{1S} - \alpha_2(1 - R_2) \\ F_{II} &= -F_2^{'}(1 - R_2) + F_{2S} + \alpha_1(1 - R_1) \end{aligned} \tag{2.4}$$

R_1, R_2, α_1 and α_2 are all dependent on the density of interface states and their nature. Since under no bias and thermal equilibrium, $F_I = F_{II} = 0$, we can therefore compute the value of F_{1S} and F_{2S}. After the substitution of the $F_1^{'}$, $F_2^{'}$, F_{1S} and F_{2S} values into Equ. 1.4, we end up to the following equation for the saturation current:

$$\begin{aligned} F &\cong F_1 exp(-qV_{D1}/kT)(1 - R_1)[\frac{\alpha_1(1 - \alpha_2)}{\alpha_2(1 - \alpha_1)} + \alpha_1] \\ F &\cong -F_2 exp(-qV_{D2}/kT)(1 - R_2)[\frac{\alpha_2(1 - \alpha_1)}{\alpha_1(1 - \alpha_2)} + \alpha_2] \end{aligned} \tag{2.5}$$

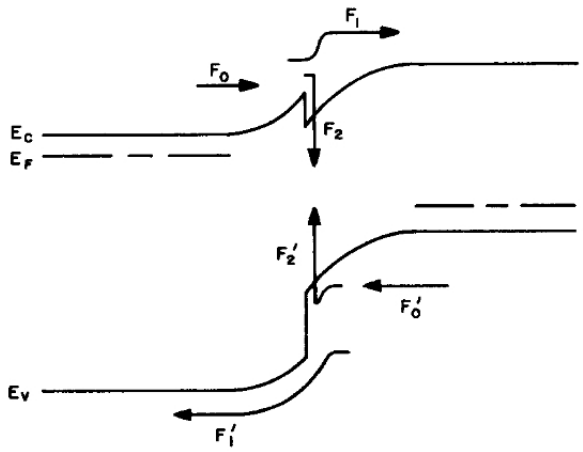

Figure 2.9: A p-n heterojunction in forward bias. The flux $F_2 = F_2^{'}$ is the space charge recombination flux [5].

The equation above gives the saturation current for V_j positive and V_j negative. The actual evaluation of those equations requires the knowledge of R_1, R_2, α_1 and α_2. Note that in the case of an ideal heterojunction, when $R_1 = R_2 = 0$ and $\alpha_1 = \alpha_2 = 1$, Eq. 1.5 represents the saturation current of a metal-semiconductor diode with the same barrier heights as region (1) and (2).

2.2.2.2 Electronic Interface State Effects on Recombination at the Junction

Consider the band diagram of a heterojunction illustrated in Fig. 2.9 (forward bias). If recombination at the junction region were negligible, then only the carrier fluxes F_1 and $F_1^{'}$ would contribute in the total current. If, however, there were a high dense layer of electronic states within the energy gap located at the interface, the current would consist of the flux of electrons F_2 into the states from the left and the flux of holes $F_2^{'}$ into the states from the right. This leakage current which flows via recombination due to the presence of the interface states depends on the recombination rate. The rate of this recombination which is assisted by interface states can be estimated using Shockley-Read-Hall recombination model.

Shockley-Read-Hall Recombination: Those recombination processes which in-

volve defect or trap states in the band gap are, by far, the most important recombination processes in real semiconductors. Trap states are spatially localized and therefore are able to capture free carriers. These carriers can subsequently be released by thermal activation or recombined with the coming opposite polarity carriers. Localized states which capture and release only electrons or holes are usually called traps. Those states which capture both electrons and holes are called recombination centers. Recombination centers usually lie deeper into the band gap than traps.

Let us assume a semiconductor which contains a density N_t trap states lying in the band gap at an energy E. Unoccupied trap states are able to capture electrons from the conduction band, and occupied trap states are able to capture holes from the valence band. In this bimolecular process, electrons are captured at the rate of:

$$U_{nc} = B_n n N_t (1 - f_t) \tag{2.6}$$

where f_t is the probability that the trap states is filled. The coefficient B_n is given by:

$$B_n = v_n \sigma_n \tag{2.7}$$

where v_n is the mean thermal electron velocity and σ_n is the capture cross section of the trap state for electrons. The electron capture lifetime resulting from a trap state is defined as follow:

$$\tau_{n,SRH} = \frac{1}{B_n N_t} \tag{2.8}$$

The electron escape rate from a trap state depends on the occupation of the trap state and can be expressed as:

$$G_{nc} = \frac{N_t f_t}{\tau_{esc}} \tag{2.9}$$

where the escape time τ_{esc} can be estimated using the condition $G_{nc} = U_{nc}$ in the equilibrium. Then it follows that:

$$G_{nc} = B_n n_t N_t f_t \tag{2.10}$$

where n_t is the electron density at the Fermi level when the Fermi level lies within trap states:

$$n_t = n_i e^{(E_t - E_i)/k_B T} \tag{2.11}$$

The same procedure can be followed for deriving a formula for hole capture and release. Basically, the capture and release rates for electrons and holes is different and depends on the affinity of the trap for electrons or holes and its location in the band gap. However, in the thermodynamic equilibrium, the net rate of electron capture by the traps $U_{nc} - G_{nc}$ must be equal to the net rate of hole capture $U_{pc} - G_{pc}$, because net charges cannot be accumulated on the traps. This forcing function fixes the value of f_t:

$$f_t = \frac{B_n n_t - B_p p_t}{B_n(n + n_t) + B_p(p + p_t)} \tag{2.12}$$

therefore f_t can be removed from the expression of $U - G$. At the end, we could obtain the net recombination rate as:

$$U_{SRH} = \frac{np - n_i^2}{\tau_{p,SRH}(n + n_t) + \tau_{n,SRH}(p + p_t)} \tag{2.13}$$

in which we have used the definitions of $\tau_{n,SRH}$ and $\tau_{n,SRH}$. This is the Shockley-Read-Hall expression for recombination via a single trap state. For doped semiconductors, the expression for U_{SRH} simplifies. In p-type material, when $\tau_n N_a >> \tau_p n_t$, and $N_a >> p_t$, U_{SRH} becomes proportional to the excess carrier density:

$$U_{SRH} \approx \frac{(n - n_0)}{\tau_{n,SRH}} \tag{2.14}$$

In n type material:

$$U_{SRH} \approx \frac{(p - p_0)}{\tau_{p,SRH}} \tag{2.15}$$

SRH recombination is more important when n and p are of similar magnitude. This can be realized from Eq. 2.13 for a mid gap trap with equal capture times, U_{SRH} has

its maximum when $n = p$. Therefore in undoped regions, where n and p are similar, SRH recombination is stronger relative to radiative recombination.

In real semiconductors, there may be several trap levels in the band gap and carriers may recombine in more than one step. However, the largest contribution is from traps which are located close to the center of the band gap. So, for bulk material with a uniform density of traps, the approximation is usually made that recombination through one particular trap level is dominant.

Surface, Interface and Grain Boundary Recombination: Based on Eq. 2.13, spatial variations in U_{SRH} can be due to variations in n and p, or due to spatial variations in the nature or the density of the dominant trap. A larger density of trap states decreases the electron and hole capture times. In reality, defects are much more likely to happen at surfaces and at the interfaces between different crystal regions in a multicrystalline or heterojunction material. Trap states at surfaces and interfaces result from both crystal defects due to broken or strained bonds, and extrinsic impurities which come from the external environment, or which are concentrated at the interface during growth. In such cases, the traps responsible for recombination are located in a two-dimensional instead of three-dimensional space and it is more meaningful to express the recombination in terms of the trap state density per unit area of the surface or interface, than per unit volume. The related quantity would be a recombination flux which is the number of carriers recombining at the interface per unit area per unit time, rather than a volume recombination rate.

If the surface has a density N_s trap states per unit area, then within a very thin layer, δx, close to the surface, the surface recombination flux will be:

$$U_S \delta x = \frac{n_s p_s - n_i^2}{\frac{1}{S_p}(n_s + n_t) + \frac{1}{S_n}(p_s + p_t)} \tag{2.16}$$

per unit area, in which n_s and p_s are the density of electrons and holes at the interface.

S_n is the surface recombination velocity for electrons, expressed by:

$$S_n = B_n N_s \tag{2.17}$$

and S_p is the surface recombination velocity for holes, expressed by,

$$S_p = B_p N_s \tag{2.18}$$

This leakage of minority carriers to the surface results in a surface recombination current. The value of this current can be computed from the electron continuity equation. In the dark, at equilibrium, the continuity equation requires that $\bigtriangledown . J_n = qU_n$. By taking the integral from this equation across the interfacial layer, change in the electron current density is given by:

$$\Delta J = J(x_s + \frac{1}{2}\delta x) - J(x_s - \frac{1}{2}\delta x) = q \int_{x_s - \delta x}^{x_s + \delta x} U dx = qS_n(n_s - n_0) \tag{2.19}$$

When a carrier is captured by a trap, it may then be released or it may be annihilated by the capture of the opposite type of carrier. When the time for electron release by thermal activation:

$$\frac{1}{\tau_{esc}} = B_n n_i e^{(E_t - E_i)/k_B T} \tag{2.20}$$

is much shorter than a hole capture:

$$\frac{1}{\tau_{cp}} = B_p p \tag{2.21}$$

the state can be considered an electron trap rather than a recombination center. This may happen if the state is close in energy to the conduction band edge, or if the cross section for electron capture is much larger than for hole capture, as, for instance, for a positively charged defect. Similarly, localized states which are close to the valence band or which have a higher cross section for hole capture act as hole traps. Traps serve to slow down the transport of carriers but they do not remove them.

The topic covered so far in this chapter involve the general properties and characteristic of heterojunctions. The rest of this chapter is dedicated to a brief review of the properties of crystalline silicon, amorphous silicon, crystalline gallium phosphide, which provides the basics for the heterojunctions studied in this dissertation.

2.3 Crystalline Silicon

General Properties: Silicon is found in stars and the sun and is a main component of a class of meteorites. The earth's crust contains 25.7% silicon, by weight, which makes Si the second most abundant element after oxygen in the earth's crust. Silicon is not naturally present in its elemental form, but mainly found as an oxide and as silicates. Silicon is produced commercially by heating silica in the presence of carbon in an electric furnace, using carbon electrodes. The Czochralski process is usually used to prepare single crystals silicon in order to use in solid-state or semiconductor devices. Crystalline silicon has a metallic luster and grayish color. However, silicon can be also prepared in the amorphous allotrope as a brown powder, which can be easily melted or vaporized. It is also possible to prepare silicon in nanosheet, nanowire, nanotube, nanoparticle, nanocluster, and quantum dot forms with different properties from bulk form.

Silicon is one of the most frequent elements used in human life. In the compound form, it is used to make concrete, brick, refractory material for high-temperature work, enamels, pottery, and glass. Glass is one of the most inexpensive materials with excellent mechanical, optical, thermal, and electrical properties and can be made in a variety of shapes, and is used as containers, window glass, insulators, and thousands of other uses. In elemental form, very pure silicon can be doped with boron, gallium, phosphorus, or arsenic to produce silicon for use in solar cells, transistors, rectifiers, lasers and other solid-state devices which are used widely in the

electronics and space-age industries.

Electronic Properties: Silicon is an indirect band gap semiconductor which means the maximum of its valence band is not at the same position in momentum space as the minimum of its conduction band. This feature results in two major consequences. First, it causes radiative recombination to be fairly low, which means that, for defect-free silicon, the photogenerated electrons and holes have very long lifetimes. Instead, the dominant intrinsic recombination mechanism in Si is Auger recombination. In Auger recombination, an electron recombines with a hole by giving their energy difference to a third charge carrier, either a second free electron or second free hole. This energy is finally lost as heat. Consequently, based on the experimentally measured radiative and Auger recombination rates [70], the maximum intrinsic efficiency for silicon solar cells has been calculated to be 29.4% [25]. Second, due to its indirect band gap, Si has a relatively low absorption coefficient, especially near the band edges. However, with wafer surface texturing, associated with the use of well designed anti-reflection coatings and rear surface mirrors, high light absorption, including the infrared section of the solar spectrum, is possible even with thin wafers ($\sim 100 - 150\mu m$) [25]. Practically, carrier recombination in Si can be affected, or even dominated, by the existence of crystallographic defects or external impurities. Thanks to improved Si ingot growth processes, defect engineering, and contamination control during heterojunction device fabrication, the bulk electronic properties of c-Si wafers has improved to such a level that further device improvement now depends on innovative interface passivation and carrier-selective contact structures.

The main goal of interface passivation is to decrease recombination of photogenerated carriers at the silicon surface [71–73] which reduces dark current and consequently control V_{oc}. This goal can be achieved by chemical passivation, usually by

hydrogen, of undesirable surface defects [74–77], corresponding to broken and strained silicon-silicon bonds, or by modifying the relative concentration of photo-generated carriers near the surface [78, 79]. Effective surface passivation is usually achieved by dielectric materials such as silicon dioxide [78, 80–84], silicon nitride [85–88], silicon carbide [89, 90] and aluminum oxide [71, 91–93]. Alternatively, a (disordered) semiconductor such as intrinsic hydrogenated amorphous silicon [16, 94] can be employed. None of these layers allows perfect carrier extraction, as they are either insulating or insufficiently conductive.

For having efficient carrier extraction to the two external metal electrodes, two efficient carrier-selective contacts are required, that ideally present efficient transport of only one type of carrier while preventing the transport of the other type of carrier. Since recombination needs the participation of both electron and hole, preventing the transport of one of them results in reducing recombination in the contact structure. However, to prevent recombination more effectively, we usually need the presence of an interfacial passivating layer. Hence an ideal selective carrier contact is one that simultaneously presents a complete conductivity for just one type of the two carriers, while minimizing recombination. In fabricating solar cells with high efficiency, we can choose either to deposit a passivating dielectric material on most of the wafer surface and then selectively extract photo-generated carriers through local openings in this insulator [95], or to cover the full wafer surface with carrier-selective materials using a suitable interface-passivation strategy. In the second approach, both the requirements of single-carrier conduction and surface passivation are frequently achieved by employing a stack of two or more layers, for instance intrinsic and doped hydrogenated amorphous silicon, as in silicon heterojunction solar cell technology [15, 17, 26].

An important criterion for this decision relies on the optical properties of

the required materials for contact formation. Indeed, layers blanket-deposited on the wafer surfaces (either for interface passivation or selective transport) should also maximize light coupling into the silicon absorber by minimizing reflection and parasitic absorption losses. Developing contact layers that satisfy these electronic and optical requirements simultaneously represents a considerable challenge [2].

2.4 Amorphous Si (a-Si) and Hydrogenated Amorphous Si (a-Si:H)

General Properties: Amorphous silicon (a-Si) is the non-crystalline form of silicon. It is the most well developed of the thin film technologies having been on the market for more than 15 years. It is widely used in pocket calculators, but it also powers some private homes, buildings, and remote facilities. United Solar Systems Corp. (UniSolar) pioneered amorphous-silicon solar cells and remains a major manufacturer today, as does Sharp and Sanyo. Amorphous silicon panels are formed by vapor-depositing a thin layer of silicon material about 1 micrometer thick on a substrate material such as glass or metal. Amorphous silicon can also be deposited at very low temperatures, as low as 75 degrees Celsius, which allows for deposition on plastic as well. Interest in amorphous semiconductors developed around the chalcogenides, which are materials containing the elements sulfur, selenium and tellurium; examples are As_2Se_3 , GeS_2 etc. The chalcogenides are glasses which may be formed by cooling from the melt, with structure similar to the oxides but with smaller energy band gaps. Research in these amorphous semiconductors addressed the question of how the disorder of the non-crystalline structure influences the electronic properties. The study of chalcogenides was further promoted by the introduction of xerographic copying machines.

Hydrogenated amorphous silicon was first made in the late 1960s. Before that time, there was research on amorphous silicon without hydrogen, which was prepared by sputtering or by thermal evaporation. The unhydrogenated material has

a very high defect density which prevents doping, photo-conductivity and the other desirable characteristics of a useful semiconductor. Electronic measurements were mostly limited to the investigation of conduction through the defect states. Chittick and coworkers in the UK were the first to make a-Si:H, using glow discharge as the deposition technique [96]. Silane gas (SiH_4) is excited by an electrical plasma which causes the gas molecules to dissociate the deposit on heated substrates. The technique is essentially the same as is used currently, although the design of the deposition systems has evolved. The first reactor was inductive: the plasma is excited by a coil outside the quartz chamber. Most reactors now are capacitative, consisting of two parallel electrodes within a stainless steel chamber, but the deposition mechanism is not substantially different.

Atomic structure of amorphous silicon: In a system of particles distributed in three dimensional space, the radial distribution function or pair correlation function g(r) gives the number of particles (atoms, molecules, etc.) per unit volume as a function of distance, r, from a reference particle. In other words, g(r) gives the probability of two particles being separated by a distance r in a system of particles. To calculate g(r) from simulation, all the neighbors separated by r are sorted into distance bins, and then the number of neighbors is normalized with respect to the g(r) of an ideal gas where particle distances are completely uncorrelated. For three dimensions, this normalization is the number density of the system multiplied by the volume of the spherical shell, which mathematically can be expressed as is the number density. g(r) is a useful tool for describing the atomic structure of amorphous materials and can be measured experimentally using x-ray diffraction. The experimentally measured g(r) provide a very strong criteria for checking the accuracy of the atomic structure of amorphous material obtained from simulation. The radial distribution function is of fundamental importance since it can be used to link the microscopic details to

macroscopic properties and moreover it is possible to obtain the microscopic details of the radial distribution function from the macroscopic properties.

The main feature which makes amorphous material different from crystalline ones is disorder in the atomic structure. This structural disorder originates from relatively small deviations in bond lengths, bond angles, and dihedral angles from the equivalent ideal values in crystalline form. In spite of the inherent disorder, the atoms in amorphous materials are not distributed in space in a completely random way. For instance, in a-Si as in crystalline Silicon c-Si, each Si atom is averagely bounded to four other Si atoms by covalent bonds in much the same length and angle leading to short range order. This short range order is a global feature of all type of amorphous materials and can be represented by radial distribution function (RDF). A schematic example of the RDF of a network of atoms in crystalline, amorphous, and gaseous forms has been separately illustrated in Fig. 2.10. Although, the relative positions of atoms in the gaseous phase are completely random, it is highly ordered in the crystalline phase. The amorphous phase has almost the same short range order as the crystalline phase, but has the long range disorder of the gaseous phase.

The radial distribution function in a layer-by-layer format has been used for characterizing the atomic structure of crystalline/amorphous heterojunctions. Figure 2.11 shows the layer resolved RDF of the a-Si/c-Si heterojunction generated using molecular dynamics simulation [97, 98], where a layer is defined as a region that is half the Si lattice constant. The amorphous regions show a well-defined peak at the neighbouring Si-Si distance, with a reduced maximum and increased broadening in this peak compared with the crystalline RDF, which is a series of delta functions corresponding to the lattice position of nearest neighbors, next nearest neighbors etc. The second and subsequent peaks are typical of amorphous Si. An interface

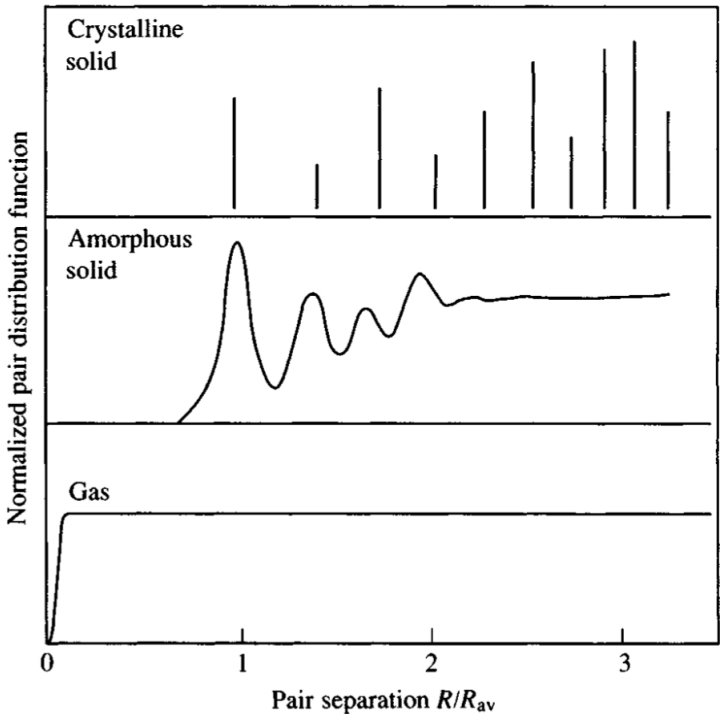

Figure 2.10: A typical RDF of a network of atoms in three different phases.

region can be also determined by examining the RDF. In an interface layer, while the RDF is obviously not characteristic of an amorphous region, it is neither typical of crystalline Si and it is clear that the peak heights are reduced and the peak widths are larger, indicating that the interface region is intermediate between c-Si and a-Si. The details of the RDF function can be used for interpreting the electronic structure of an amorphous/crystalline heterojunction.

Electronic structure of amorphous materials: From electronic structure point of view, one of the basic feature of a semiconductor (like Si) compared to a conductor is the presence of a band gap (no electronic states) between the filled valence band and the unfilled conduction band states. According to free electron theory, the periodicity of the lattice is the main reason for the appearance of a band gap in the electronic structure for free electrons. Since there is no periodicity in the amorphous structure, the main question which arises is whether an amorphous material has a bandgap or

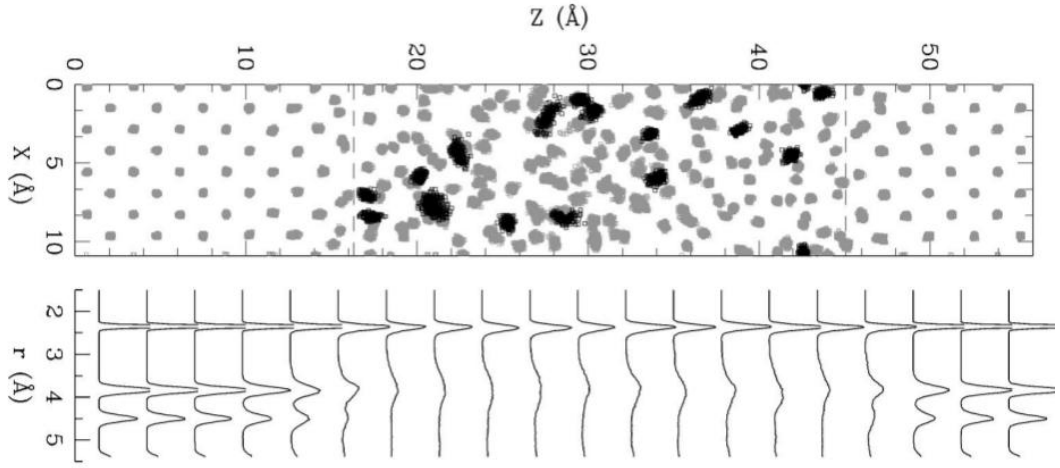

Figure 2.11: Atomic structure (upper panel) and layer resolved radial distribution function (lower panel) of a-Si/c-Si.

not. For decades, there was a controversial debate over this question. Eventually, Weaire and Thorpe presented a Hamiltonian based on a tight bonding model which could explained the band gap in amorphous materials. In their model, the band gap is a consequence of the splitting of the bonding and anti-bonding states due to the covalent bond. These bonding and anti-bonding states are mostly affected by the short range order, which is much the same in both amorphous and crystalline Si and the lack of periodicity is only a small perturbation. The form of the Weaire-Thorpe Hamiltonian is as following:

$$H = V_1 \sum_{j \neq j'} |\Phi_{ij}\rangle \langle \Phi_{ij'}| + V_2 \sum_{i \neq i'} |\Phi_{ij}\rangle \langle \Phi_{i'j}| \tag{2.22}$$

where Φ_{ij} are the wavefunctions created by SP^3 hybridization in tetrahedral bonding form. The first term in Eq. 2.22 is for the interactions between the two wavefunctions belonging to the same atom and the second term is for the interactions between two orbitals belonging to the same bond. This Hamiltonian only includes the short range bonding information, but no long range bonding information, and so can be applied to both amorphous and crystalline structure. Weaire and Thorpe proved that in a

specific range of V_1/V_2 interaction strengths, the valence and conduction band tend to be separated by a band gap, regardless of the lack or presence of long range order in the structure.

As discussed so far, the three fundamental features of amorphous structures are the short range order, long range disorder and the coordination defects. The presence of short range order is the main reason that we observe overall the same electronic structure for an amorphous network compared to a crystalline one. This is why, for instance, a-Si is a semiconductor, just like c-Si. However, as expected, there are some differences in the band structure of an amorphous structure compared to a crystalline one. The most important difference is that the sharp band edges close to the band gap in the crystalline form are replaced by a broadened band of tail of localized states extending into the gap. These localized states originate from deviations in bond length and angle. Although the density of localized states (band tail) are relatively small, they may play a critical role in charge transport occurring at the band edges. In addition to having a band tail, amorphous material also have some electronic states deep inside the band gap (midgap states) arising from coordination defects or dangling bonds. These midgap states can influentially control many electronic properties of the material by affecting trapping and recombination processes. Therefore, in general, the electronic structure of an amorphous structure comprises the valence and conduction bands, the band tails and the midgap states (Fig. 2.12).

The main step in calculating the electronic states of a many body system is solving the Schrödinger equation:

$$-\frac{\nabla^2}{2}\Phi + V(r)\Phi = E\Phi \tag{2.23}$$

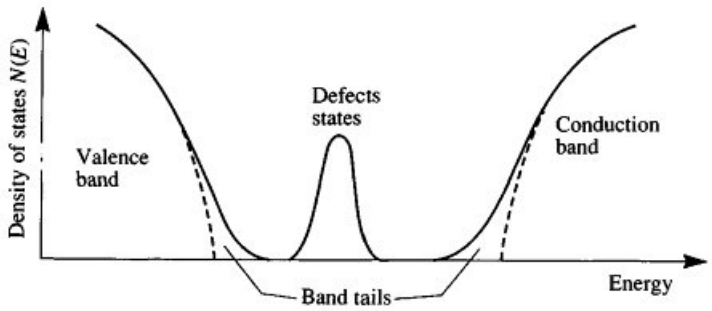

Figure 2.12: Typical electronic structure of amorphous materials.

where E is the energy of the system and V(r) is the potential energy arising from electron-electron interaction (which is neglected in free electron theory) and mostly electron-lattice interactions. The periodicity in the atomic structure leads to the same periodicity in the potential energy and consequently in the wavefunctions obtained from Eq. 2.23 which are called Bloch states. The Bloch wavefuction is expressed in following general form:

$$\Phi(\vec{r}) = exp(i\vec{k}.\vec{r})U_k(\vec{r}) \tag{2.24}$$

Where $U_k(\vec{r})$ is a periodic function having the same periodicity as the lattice. $\vec{k}$ is crystal wave vector containing the periodicity information of the lattice. Each Bloch wavefunction has a specific momentum, k, and extends through out the lattice. Therefore, the energy bands can be described by an energy-momentum (E-k) dispersion. The E-k dispersion contains important information such as the effective mass, electronic excitations, etc. However, this solution to the Schrödinger equation is not applicable for amorphous systems because $V(\vec{r})$ is no longer periodic. Emphasize on the momentum of the carrier in a crystal is replaced by emphasizing on their spatial location of the carrier in an amorphous. Some results of the lack of k-conservation are:

1) The electronic structure can not be longer expressed by the E-k disper-

sion relations, in an amorphous material. Instead, the Electronic Density-of-States Distribution is used for describing the electronic structure of an amorphous system as illustrated in Fig. 2.12. In addition, the electron and hole effective masses are meaning less any more.

2) For optical transitions, the selection rules caused by k-conservation does not apply any more for an amorphous structure. Therefore, there is no meaningful direct or indirect band gap concept. Instead, transitions happen between in the states which overlap in real space.

3) Due to the scattering and the localization of the wavefunction as a result of disorder, the carrier mobility reduces in an amorphous structure compared to a crystalline structure.

The long range disorder potential results in large electron scattering and consequently electron localization, in which the wavefunction is constrained to a relatively small volume of material instead of being extended. For explaining the localization of orbitals in an amorphous structure, Anderson (1958) presented the model illustrated in Fig. 2.13. In this model, the potential of a perfect lattice is described by an array of identical atomic potential wells and the resulting electronic band is broadened to a band width B due to the interaction between atomic orbitals. In an amorphous system, the general form of the potential model stays the same with the difference that a random potential with an average amplitude, V_0, is added. Anderson proved that if V_0/B exceeds a specific value, an electron is not able to diffuse away from one atomic site to another at zero temperature. For complete localization, the value of V_0/B is about three. Since the band width of a typical electronic band is the order of 5 eV, a huge disorder potential is necessary to make all the electronic states localized. Due to the presence of short range order, the Anderson criteria is never met for

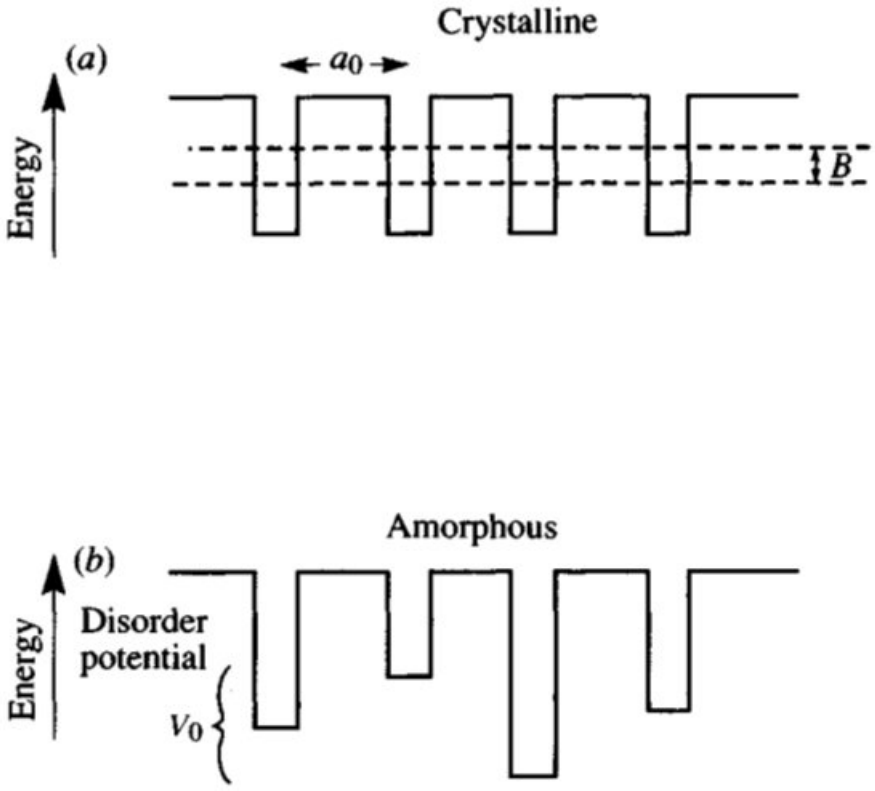

Figure 2.13: The potential model used in Anderson's theory for explaining localization.

any amorphous semiconductor. However, even a small value V_0/B leads to localized states close to the band edges. The electronic states deep within an electronic band are extended states and the states at the edges of the band are localized states. The extended and localized states are separated by a mobility edge. In the conduction band of a semiconductor, only the electrons higher than the energy of the mobility edge, E_c, are able to move at zero temperature.

The electronic structure arising from Anderson's model is illustrated in Fig. 2.14. The location of the mobility edge inside the band depends on the amount of disorder and vary typically between 0.1-05 eV from the band edge. It is worth noting that the nature of the electronic states close to the mobility edge are more complicated than in the simple model with an abrupt mobility edge, and details regarding this

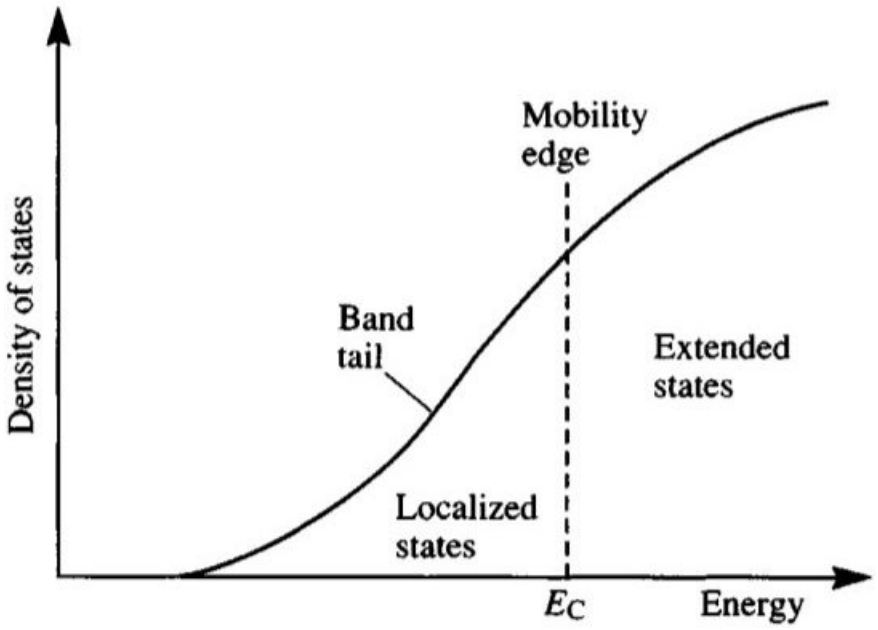

Figure 2.14: The EDOS distribution of a semiconductor close to band edge.

topic are beyond the scope of this dissertation. Creating a mobility gap between extended and localized states is not the only consequence of disorder in the structure, the disorder can also effectively control the electron and hole mobilities above the mobility edges.

2.5 Gallium Phosphide (GaP)

General Properties: Pure crystalline gallium phosphide appears clear orange. GaP does not occur in naturally, but its constitutive elements exit in the earth's crust in relatively high amounts. Ga is the 35th most abundant element (close to Co, Li, and Pb and much higher than Be, Sn, Ge, Br, Tl, Sb, I, Cd, Ag, Hg, Se, and In) in the earth's crust and P is the 11th most abundant element (close to H) in the earth's crust. GaP is not soluble in water and is odorless. Interest in GaP was initially due to its application in low-cost green, yellow, and red light-emitting diodes (LEDs) with low to medium brightness. Pure gallium phosphide emits green light at a wavelength of 555 nm. The conversion efficiency of green GaP-based LEDs is only 0.1 % due to

the indirect bandgap of a pure GaP. Therefore dopants like nitrogen, zinc or oxygen are used in order to increase the LED efficiency. Yellow-green is emitted by GaP doped with nitrogen at a wavelength of 565 nm. GaP doped with zinc oxide emits red light at a wavelength of 700 nm. GaP in combinations with some elements such as Al, In, As, and N present a wide range of bandwidth starting from 1.42 eV of GaAs to 2.26 eV of pure GaP. Some of these alloys are also direct bandgap. Like GaAs, gallium phosphide can potentially be used as a semiconductor substrate for high speed electronic and optoelectronic circuits, and can compete with other commonly used semiconductors in the present opto-electronic industry due to its high mechanical strength, chemical resistance, thermal conductivity and hardness. In addition, GaP can be used in visible and near infrared applications where most of the interesting infrared materials is unusable due to absorption (GaP as a material for visible and infrared optics). GaP is also an excellent candidate to be part of a high band gap solar cell in a multijunction or tandem system, due to its wide band gap (2.26 eV).

GaP has usually been grown in crystalline thin film form by using epitaxial techniques. In addition to crystalline form, amorphous GaP (a-GaP) has also been synthesized for application in LEDs and high-temperature transistors by N. Elgun et al. (1994). The flexibility of its energy gap should be useful for tuning wide area tandem solar cells in the near future. In the photovoltaic field, a-GaP has the advantages of being relatively cheap, with low temperature deposition and the possibility of growth on a variety of substrates, including glass, metal and plastic, with diverse commercial applications. As mentioned above, epitaxial techniques have mainly been used to grow crystalline GaP thin films; however, several deposition methods have also been used for the preparation of amorphous and crystalline GaP thin films, like plasma enhanced chemical transport deposition (PECTD), evaporation, plasma deposition, liquid phase epitaxy, ion beam assisted deposition and sputtering. Among

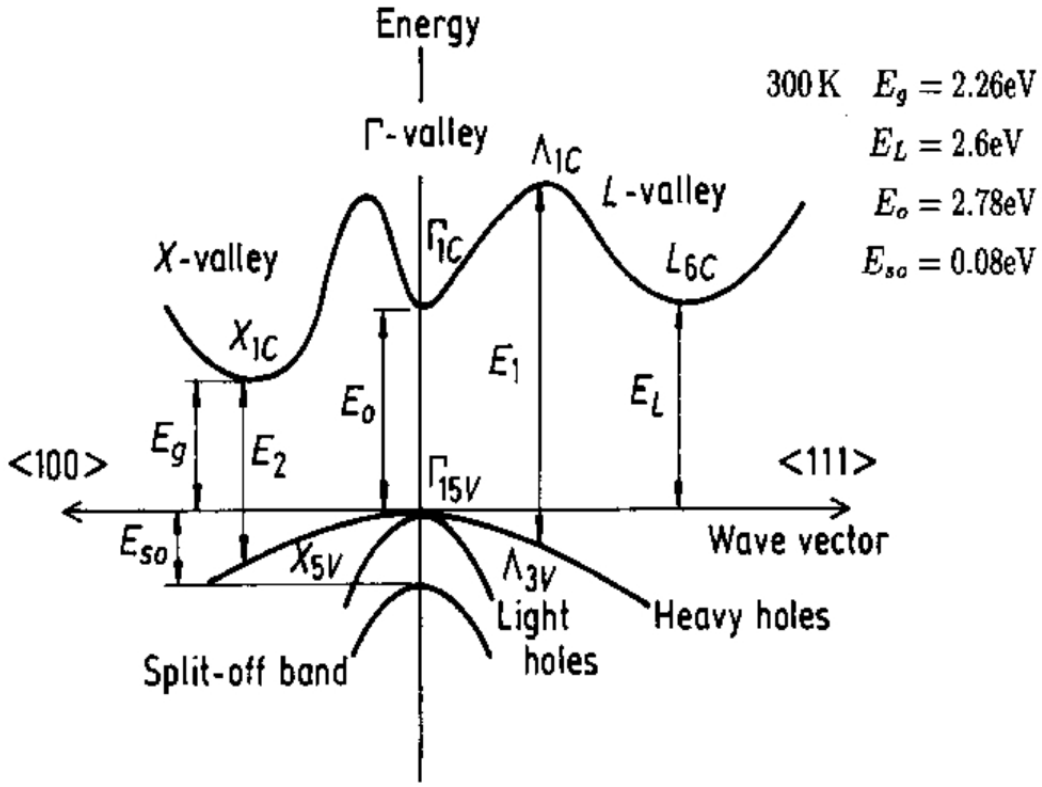

Figure 2.15: The band structure of GaP in crystalline form.

these deposition techniques, radio frequency (RF) sputtering is known to be suitable for large-scale applications in device fabrication at a relatively low cost [99]. This technique has been also used for preparing hydrogenated a-GaP. It is possible to synthesis GaP with different size and shape such as nanowires, nanotubes and quantum dots. Meanwhile, it is feasible to economically grow of GaP epi-layers on silicon substrates because of its high lattice match with silicon [100].

Electronic Structure: Gallium phosphide (GaP) is an important III-V semiconductor with an indirect band gap of 2.26 eV at room temperature. Figure 2.15 is showing the band structure of pure GaP in its crystalline form. The energy is plotted as a function of the wavevector along the main crystallographic directions in the crystal, since the band diagram depends on the direction in the crystal. The

band structure has been simplified to the band structure close to conduction and valence band since only electrons in the highest almost-filled band and the lowest almost-empty band dominate the behavior of the semiconductor. An important feature which can be extracted from the band structure is whether the conduction band minimum and the valence band maximum occur at the same wavevector. In the GaP case, valence band maximum occurs at the Γ point, but the minimum conduction band occurs at the X point. Therefore, GaP is an indirect bandgap material. The mobility of an electron or a hole in the presence of an applied electric field can be determined directly by the gradient of the energy function $dE(k)/dk$. In GaP, the electron and hole mobilities are 250 and 450 $cm^2V^{-1}s^{-1}$, respectively. In comparison with Si, the electron and hole mobilities are 1400 and 450 $cm^2V^{-1}s^{-1}$ in Si, respectively.

Chapter 3

THEORETICAL METHODS

In this chapter, a brief overview of the computational method used in our study is given. The electronic structures of all studied materials are calculated from first principles (DFT). Therefore, in the first part of this chapter, an overview of the detail of DFT and MD calculations will be given and in the second part including a brief overview of important aspects of DFT is given. Also, the concepts of basis set and Pseudopotential functions will be briefly described.

3.0.1 Computational Details

We use a melting and quenching approach based on MD simulation for generating a structural model of a-Si, as the starting atomic structure for feeding DFT calculations. The LAMMPS molecular dynamic code was used for simulating the melting and quenching process. In the simulation, the Tersoff interatomic potential [101] was employed for describing the Si atom interactions, with the cut-offs set as 2.7 Å(taper) and 3.0 Å(maximum); this potential has been widely used for generating Si based structures. Full ion relaxation of all the structures resulting from MD were carried out at the DFT-level as implemented in the Quantum Espresso 5.2.1 software package. The BFGS quasi-newton algorithm, based on the trust radius procedure, was used as the optimization algorithm to find the relaxed structure.

Both the ionic relaxation and the electronic structure calculations was performed using the Becke-Lee-Yang-Parr (BLYP) or Perdew-Burke-Ernzerhof (PBE) exchangecorrelation functional [102–104]. The core and valance electrons interaction were described by the Norm-Conserving Pseudopotential function. A energy cutoff (E_{cut}) of 12Ry was employed for the plane-wave basis set and an $8 \times 8 \times 8$ k-point mesh was used with the Monkhorst-Pack grid method for Brillouin-zone sampling in

all calculations, unless otherwise stated.

3.0.2 Density Functional Theory

DFT is a single partical theoretical method in quantum mechanics used in physics, chemistry, and material science as an alternative to solving the many-body Schrödinger equation. The demonstration of its validity is well-established for the ground state, while theoretical issues remain open regarding its applicability to excited states. The use of DFT in solving complicated many-body problems has led to a dramatic reduction in the computational expense and time, which explains why DFT has become one of the most popular computational methods in computational chemistry.

DFT relies on the Hohenberg-Kohn theorems which state that [67, 68]:

Theorem 1. If two systems of electrons have the same ground state density $\rho(r)$, with one trapped in the potential $V(r)$ and the other in the potential $V'(r)$, then:

$$V(r) - V'(r) = Constant \tag{3.1}$$

From this theorem, one can conclude that $V(r)$ is a unique functional of ρ and consequently the wave-function obtained from the solution of the Schrödinger equation based on the given $v(r)$ will be also a unique function of ρ. Therefore, it is possible to define an energy functional as below:

$$E[\rho(r)] = \int_{-\infty}^{\infty} drV(r)\rho(r) + F[\rho(r)] \tag{3.2}$$

Based on this equation, one can prove that:

Theorem 2. The global minimum of the energy functional, Eq. 3.2, is the true ground-state energy, E_0, for the system and the density that minimizes the functional is the ground-state density, $\rho_0(r)$.

In Eq. 3.2, $F[\rho(r)]$ is an universal functional containing the kinetic energy and the potential energy of the electrons resulting from the Coulomb repulsion between them. In the majority of systems, $F[\rho(r)]$ is an extremely complicated functional whose exact form is not known, and should be approximated in some way. Despite the need for an approximate form of this functional, the Hohenberg-Kohn theorems still make the quantum mechanical calculations much simpler by mapping the many-body problem to an electron density problem dependent on just three spatial variables.

One of the earliest approximations for the universal functional, $E[\rho]$ was proposed by Kohn and Sham based on an effective potential model [68]. They introduced the idea of an auxiliary system of non-interacting electrons for which the kinetic energy functional and the exact density could be written in terms of one-electron Kohn-Sham orbitals. Employing this approximation, the many-body problem can be mapped into a set of coupled one-electron equations similar in spirit to the Hartree-Fock scheme but actually preserving the many-body character of the problem :

$$H\Phi_j(r) = \varepsilon_j \Phi_j(r) \tag{3.3}$$

$\Phi_j(r)$ is Kohn-Sham (KS)-wavefunction and ε_j is the eigenvalue of the KS-wavefunction. The Hamiltonian of the system in the Kohn-Sham formalism is:

$$H = \frac{\bigtriangledown^2}{2} + V_{eff}(r) \tag{3.4}$$

and

$$V_{eff}(r) = V_{ext} + \int \frac{\rho(r')}{|r - r'|} dr + \frac{\partial E_{xc}[\rho(r)]}{\partial \rho(r)} \tag{3.5}$$

As seen, the effective potential includes three terms. The first term is the external potential describing the interaction between the nucleus (ion cores) and the valence electrons, the second term is the repulsive Coulomb interaction between electrons, and the third term is the exchange correlation energy, which is the most complicated

term and needs to be approximated. The KS-equation should be solved iteratively as follow:

1) The initial form of $\rho(r)$ is approximated.

2) The KS Hamiltonian is constructed based on Eq. 3.4.

3) The KS-wavefunctions are obtained via Eq. 3.3.

4) The new electron density is calculated through $\rho(r) = \sum_j |\phi_j(r)|^2$.

5) If the difference between the new and old electron density is equal or lower to the convergence criteria, the KS equations are considered solved, otherwise the process is repeated from Step 2.

In order to solve KS equations, it is necessary to find a description for the exchange-correlation (XC) energy functional. This function appears in the KS equation for correcting the error resulting from using the non-interacting kinetic energy of the electrons and using classical electron-electron interactions. Quantum treatment of electron-electron interactions includes the Fermi correlation which prevents two electrons with parallel spins to be in the same point of space; Coulomb effects which describes the correlation between the position of two electrons due to the Coulomb repulsion, and the correlation related to the overall symmetry of the system wavefunction. The exact form of the XC functional is unknown, but there are various approaches to approximate this functional. The earliest approximation of the XC functional was proposed by Kohn-Sham [68] known as the Local Density Approximation (LDA). There, E_{xc} obtained in the LDA is described as follows:

$$E_{xc}^{LDA}(\rho) = \int \rho(r)\varepsilon_{xc}[\rho(r)]dr \tag{3.6}$$

Here, ε_{xc} is the E_{xc} per electron in a homogeneous electron gas with the spatial electron density of $\rho(r)$ obtained from theories of a homogeneous electron gas. Since the LDA gives a bad approximation of E_{xc} in some systems, there have been so many

efforts to introducing a better functional for estimating E_{xc}. Maybe the most well-known and well-used functional for the exchange-correlation energy after LDA is the Generalized Gradient Approximation (GGA) which states that the XC energy not only depends on the value of the electron density, but also it depends on its spatial gradient [105]. The typical form for a GGA functional is:

$$E_{xc}^{GGA}(\rho) = \int \rho(r)\varepsilon_{xc}[\rho(r), \bigtriangledown\rho(r)]dr \tag{3.7}$$

The GGA significantly improves on the LDA description of the binding energy of molecules. This improvement caused the wide spread acceptance of DFT in the chemistry community in the early 1990s. it is worth mentioning that both E_{xc}^{LDA} and E_{xc}^{GGA} can be separated into two exchange and correlation parts [106]:

$$E_{xc}^{LDA}(\rho) = E_{x}^{LDA}(\rho) + E_{c}^{LDA}(\rho) \tag{3.8}$$

$$E_{xc}^{GGA}(\rho) = E_{x}^{GGA}(\rho) + E_{c}^{GGA}(\rho) \tag{3.9}$$

Based on this separation, different hybrid exchange correlation functionals have been proposed for further accuracy such as the linear combination of E_{xc}^{LDA} and E_{xc}^{GGA}. One of the well-known and successful hybrid functionals is B3LYP (Becke, three-parameter, Lee-Yang-Parr). This functional is defined as follows:

$$E_{xc}^{B3LYP} = E_{x}^{LDA} + a_0(E_{x}^{HF} - E_{x}^{LDA}) + a_x(E_{x}^{GGA} - E_{x}^{LDA}) + E_{c}^{LDA} + a_c(E_{c}^{GGA} - E_{c}^{LDA}) \tag{3.10}$$

where E_{x}^{HF} is the HartreeFock exact exchange functional:

$$E_{x}^{HF} = -\frac{1}{2}\sum_{i,j}\int\int \psi_i^*(r_1)\psi_j^*(r_1)\frac{1}{r_{12}}\psi_i(r_2)\psi_j(r_2)dr_1dr_2 \tag{3.11}$$

Since this functional is not available in the Quantum Espresso software, we instead use another well verified exchange-correlation functional named BLYP. The mathematical expression of BLYP is similar to B3LYP and is explained in details in previous works [103, 107].

3.0.3 basis set and Pseudopotential

As mentioned before, in order to solve the Kohn-Sham equation, an initial guess for $\rho(r)$ as the starting point of the calculations is required. The initial ρ can be obtained from the initial guess of a wavefunction constructed from a linear combination of atomic wavefunctions of the atoms in the given system. Several different approaches have been proposed to generate atomic wavefunctions in order to correctly describe the behavior of the electrons in the core and valance levels. These atomic wavefunctions are called the basis set. The 4 main popular basis set are: Plane Wave, Guassian, Augmented, and Numerical. Since the Quantum Espresso code only uses a plane wave basis set for performing DFT calculations, here we briefly explain this particular basis set. It is worth to notify that plane wave basis set are widely used in many solid state calculations.

According to Bloch's theorem, the electronic wavefunctions for a lattice of atoms at each k point can be expressed in terms of plane wave basis set as following:

$$\Psi_{\vec{k}}(\vec{r}) = \sum_{\vec{K}} C(\vec{K}) exp(i\vec{K}.\vec{r}) \qquad\qquad \vec{K} = \vec{k} + \vec{G}. \tag{3.12}$$

where $exp(i\vec{K}.\vec{r})$ are the plane wave basis set and the sum runs over all $\vec{G}$. Here, $\vec{G}$ is reciprocal lattice vector and $\vec{k}$ is wavevector of the electronic wavefunction. $C(\vec{K})$ presents the expansion coefficients of the basis set and follows the relation:

$$(\lambda_{\vec{K}} - \epsilon)C(\vec{K}) + \sum_{\vec{G}} U_{\vec{G}} C(\vec{K} - \vec{G}) = 0 \qquad\qquad \lambda_{\vec{K}} = \hbar^2 K^2/2m \tag{3.13}$$

where $U_{\vec{G}}$ denotes the Fourier transform of the periodic potential lattice. In order to describe $U_{\vec{G}}$, pseudopotential functions are required which account for both the ion core and electronic shell potential. Theoretically, we need to expand the wavefunctions in terms of an infinite number of plane waves basis set which is computationally

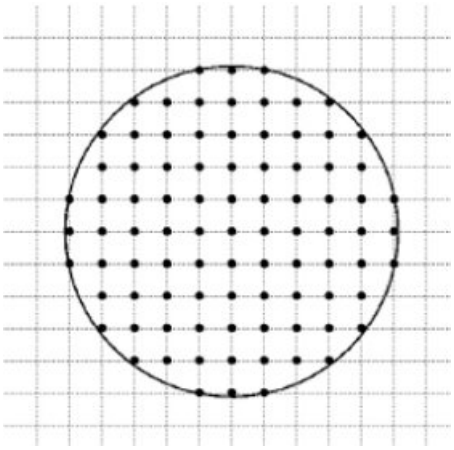

Figure 3.1: Truncation of the basis set plane wave using E_{cut}.

impossible. Since the $C(\vec{K})$ coefficients decrease exponentially with increasing K, practically only finite number of plane waves corresponding to some maximum value of K are needed within a certain numerical accuracy. In calculations, E_{cut} is the factor which specifies the number of plane waves in the wave function expansion. In fact, a plane wave with specific K will contribute in the expansion, if its K satisfy the following relation:

$$\frac{\hbar^2(k+G)^2}{2m_e} < E_{cut} \tag{3.14}$$

The truncation of the basis set using E_{cut} is illustrated in Fig. 3.1. With a limited number of plane waves, all the wavefunctions and their energies can be calculated. Other physical quantities of the system (e.g. charge density) are also computationally possible with integrating that quantity over the entire Brillouin Zone (BZ). For example, the electron density can be calculated using the following equation:

$$\rho(r) = \sum_{i}^{occ} \int_{\Omega_{BZ}} |\Psi_{i,\vec{K}}(\vec{r})|^2 \frac{d^3K}{\Omega_{BZ}} \tag{3.15}$$

where the sum runs over all occupied bands, j. Since there is so many K-points in the BZ, integration of Eq. 3.15 is computationally difficult. Therefore, the integral

is replaced by a sum containing fewer K-points but with the weights, w_n:

$$\rho(r) \approx \sum_{i}^{occ} \sum_{n=1}^{N_{kpt}} w_n |\Psi_{i,\vec{K}}(\vec{r})|^2 \tag{3.16}$$

From a computational point of view, uniformly sampling K-points from the BZ is critical to accurately calculate $\rho(r)$. One of most successful and widely used methods for K-point sampling is the Monkhorst-Pack method. The interested reader referred to the original paper for more details [108].

Although, the electrons in the valence states are represented explicitly with plane wave basis set, the core electrons and nucleus of an atom together were represented by pseudopotential functions. Using this approach makes DFT calculations inexpensive and shorter for the systems containing many atoms as well as heavy atoms. There has been much effort in finding ways to create proper pseudopotentials which are both successful to describe the many-electron behavior correctly, and are computationally efficient at the same time. For the Quantum Espresso calculations performed in this dissertation, the pseudopotentials are created from all-electron atomic calculation performed in DFT through solving the radial Kohn- Sham equations:

$$(-\frac{1}{2}\frac{d^2}{d^2r} + \frac{l(l+1)}{2r^2} + v[\rho; r)])rR_{n,l}(r) = \varepsilon_{nl} rR_{n,l}(r) \tag{3.17}$$

Here $v[(\rho; r)]$ is the self-consistent one-electron potential:

$$v[\rho; r] = -\frac{Z}{r} + v_H[\rho; r] + v_{xc}[\rho(r)] \tag{3.18}$$

v_H is the Hartree potential, v_{xc} is the exchange-correlation potential functional of the core electrons, and $\rho(r)$ is the total electron density of the wavefunctions occupied by the core electrons. The pseudopotential should satisfy following conditions:

1) The psuedo-wavefunctions obtained from pseudopotential shouldn't have a node.

2) The normalized atomic radial pseudo-wave-function (PP), with angular momentum

l, should be equal to the normalized radial all-electron wavefunction (AE) after a given cutoff radius, r_c:

$$R_l^{PP}(r) = R_l^{AE}(r) \qquad for \qquad r > r_c \tag{3.19}$$

3) Both wavefunctions (PP and AE) should have the same charge inside of the cutoff radius as follows:

$$\int_0^{r_c} |R_l^{PP}(r)|^2 r^2 dr = \int_0^{r_c} |R_l^{AE}(r)|^2 r^2 dr \tag{3.20}$$

4) The eigenvalues of AE and PP wavefunctions must be the same.

A pseudopotential with these conditions are usually called, "norm-conserving pseudopotential" and this type of pseudopotential is used in the DFT calculations.

Chapter 4

ELECTRONIC STRUCTURE AND LOCALIZED STATES IN AMORPHOUS SI AND HYDROGENATED AMORPHOUS SI

As discussed in Chapter 2, amorphous silicon (a-Si) is utilized in many material technologies such as solar cells, thin film transistors, LCD, photo-sensors, and photoreceptors [109–114]. It is generally accepted from experimental and theoretical studies that most of the optical and electrical properties of a-Si including absorption, photodegradation (SWE), and charge transport are strongly affected by the presence of mid-gap states in the electronic structure of a-Si, which results from the existence of microscopic structural disorder and defects [115–117]. Dangling bonds (DBs) are mostly believed to responsible for these mid-gap states, and contribute strongly to the optical and electrical properties of a-Si. However, there are indications that other metastable and likely less localized structural defects may also contribute [115, 118]. On the other hand, since large amounts of H are usually used to saturate dangling bonds in an a-Si structure, the nature and the interaction of H with these metastable defects is also a matter of interest. Different possible interactions of H atoms with these metastable structural defects may result in different atomic configurations, and consequently different electronic structure [119, 120]. Therefore, improved understanding of the defect configurations contributing to the electronic structure beyond DBs, and of the influence of hydrogenation, is important to improve the material properties of a-Si [121]. In this dissertation, we investigate the nature of possible H interactions with different metastable structural defects and further investigate the effect of hydrogen on mid-gap states and orbital localization based on its interaction with the aforementioned defects.

Part of this work was presented as a talk in 2016 MRS Spring Meeting & Exhibit-Phoenix in March 31 and a full version is going to be submitted to a peer-reviewed journal.

Several theoretical and computational studies have been reported on the properties of a-Si, with and without H [97, 122–129]. The accuracy of these studies are dependent on generating a reliable computer model for the a-Si and a-Si:H atomic structure. In the case of a-Si, molecular dynamics simulations in conjunction with DFT calculations have yielded structures whose properties are commensurate with experimental results [98]. In the case of a-Si:H, the type of simulations performed vary over a broad range, from simple classical models to accurate first principle models. One of the earliest approaches to generate the structure of a-Si:H was the Bethe-lattice approach [123]. Later, there were a class of approaches to saturate dangling bonds in the pure a-Si structure by adding hydrogen by hand or numerically, and then relaxing the resulting structure using Keating-type potentials for both the H and Si atoms [130–133]. Different types of interatomic potentials (such as the Stillinger-Weber-type) were later developed to generate a-Si:H networks [131]. In addition to these reports, which were mostly based on classical models, there have also been several attempts using ab initio MD to create realistic structures of a-Si:H based on the Car-Parrinello approach [122, 124]. In this approach, the interatomic potential obtained from DFT is used to simulate the melting and quenching processes on structures containing both H and Si atoms. In addition to DFT, the tight binding model has been also used to describe the interaction between atoms, in order to generate a-Si:H networks based on the melting and quenching approach [128].

In the present work, we report a new method to create low defect and stable configurations of a-Si:H. The procedure consists of adding hydrogen atoms to a fully optimized a-Si supercell obtained from MD-DFT methods using melting and quenching, in which fully optimized DFT calculations were performed on many possible configurations after each H atom addition. The optimized configurations obtained from DFT with the lowest energy were then taken as the most stable configurations.

Using this method, we generated a total of 8 stable configurations which differ in H concentration from 2 to 12% to investigate the effect of hydrogen addition on the atomic and electronic structure of a-Si. This method enables us to investigate which structural defects are more sensitive to the addition of H, by analyzing various stable configurations of a-Si:H. Furthermore, we investigate the effect of hydrogen addition on the electronic properties of a-Si:H with different hydrogen concentrations and bonding configurations.

4.1 Method

4.1.1 Generation of the a-Si and a-Si:H Structures

Molecular Dynamics simulations in conjunction with DFT calculations have been demonstrated to yield amorphous material structures whose properties are commensurate with experimental results [98, 134, 135]. Therefore, we initially carried out MD simulations to generate a general form of the a-Si structure, and then relaxed the structure using a DFT calculation to obtain an experimentally compatible structure.

MD simulation of the melting and quenching process was carried out on a crystalline Si structure in order to create an a-Si supercell containing 64 Si atoms (a-Si64) with three dimensional (3D) periodic boundary conditions. A diamond starting atomic structure of crystalline Si with an experimental lattice constant of $a_0 = 5.43\mathring{A}$ was constructed using a cubic supercell with the dimension of $a = b = c = 2a_0$, which was periodically repeated in 3D space to generate an infinite network of atoms. Then, we carried out a simulated melting process at 3000 K for 10 ps with a fixed volume and temperature ensemble (NVT). A simulation time step of 0.1 fs was used. The structure obtained from the 10 ps melting was consequently quenched to 300 K, with a cooling rate of 6×10^{12} K/s which we refer to as a medium cooling rate. After quenching, the a-Si structure was annealed for 25 ps at 300 K. Finally, the structure

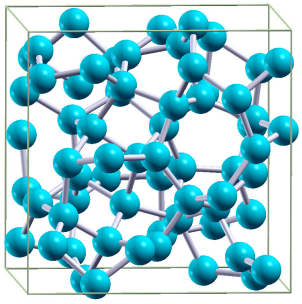

Figure 4.1: The atomic structure of the a-Si64 supercell.

was fully optimized using DFT relaxation calculation.

Six complete MD simulation cycles, as described above, were performed on the same c-Si supercells with six different cooling rates ranging from 2×10^{12} to 2×10^{13} in order to generate six different a-Si supercell as the starting structure for DFT calculations. We found similar results for the simulated structural and electronic properties for all the a-Si supercells. Therefore, in the present work, we focus on the detailed resulted obtained for one a-Si structure, that of from medium cooling rate (6×10^{12}).

Figure 4.1 illustrates the atomic structures of an a-Si supercell containing 64 atoms obtained from MD simulation (with medium cooling rate) and DFT relaxtion calculation. Based on the periodic structure formed from the supercell in Fig. 4.1, all the Si atoms in the supercell except two of them (each of them has one dangling bond) are bonded to four other Si atoms through covalent bonds with an assumed cutoff Si-Si bond length of 2.58 Å, which is 10% longer than the experimental Si-Si bond length (2.35 Å). The structure mostly displays stable 5, 6 or 7 fold rings, and there are no large voids or holes inside it. The average Si-Si bond length is 2.34 Å with an rms value of 0.04 Å and the average Si-Si-Si bond angle is 108.100° with an rms value of 1.256°. In the crystalline form of Si, the Si-Si bond length is 2.35 Å and the Si-Si-Si bond angle is 109.471°. Interestingly enough, the amorphous structure

obtained after the MD quenching phase did not have any dangling bonds, rather floating bonds, and only after the DFT optimization did the dangling bonds appear, leading to a lower energy structure.

For obtaining an atomic structural model of a-Si:H with H at%=2 (a-Si64H), the supercell of a-Si with 64 atoms obtained from MD is first relaxed using DFT methods and then a single hydrogen atom is added to this fully relaxed supercell. Since there are 64 possible ways to bond a hydrogen atom to the supercell (the hydrogen atom can be bonded to each of the 64 Si atoms), DFT ion relaxation calculations were carried out on all 64 possible configurations. The configuration with the lowest energy computed by the ion relaxation calculations is chosen as the most stable configuration in order to perform further calculations. The same procedure was repeated for finding the most stable configuration of a-Si:H with H at%=3 (a-Si64H2), with the difference being that a single hydrogen atom was added to the most stable configuration of a-Si:H with H at%=2. The same strategy was used for generating a-Si:H with higher hydrogen concentrations. Here, the short hand label of a-Si64Hn was used to determine the number of H atoms in the supercell where "n" indicates the number of H atoms in the a-Si supercell containing 64 Si atoms. We also use the label of Si#n to indicate the n^{th} Si atom in the supercell.

The reliability of the structures obtained from the MD-DFT protocol were checked by calculating the Radial Distribution Function (RDF) using the LAMMPS program. The RDF gives the probability of finding two atoms in a structure separated by a distance, r. Figure 4.2 shows the calculated RDF of the a-Si and a-Si:H structures compared the experimental results [6, 7]. As can be seen, both the calculated and experimental RDF exhibit a strong peak at 2.3 Å and two weak peaks around 4 and 6 Å. The small peak which appears adjacent to the highest peak, around 1.5 Å, is due to the presence of H.

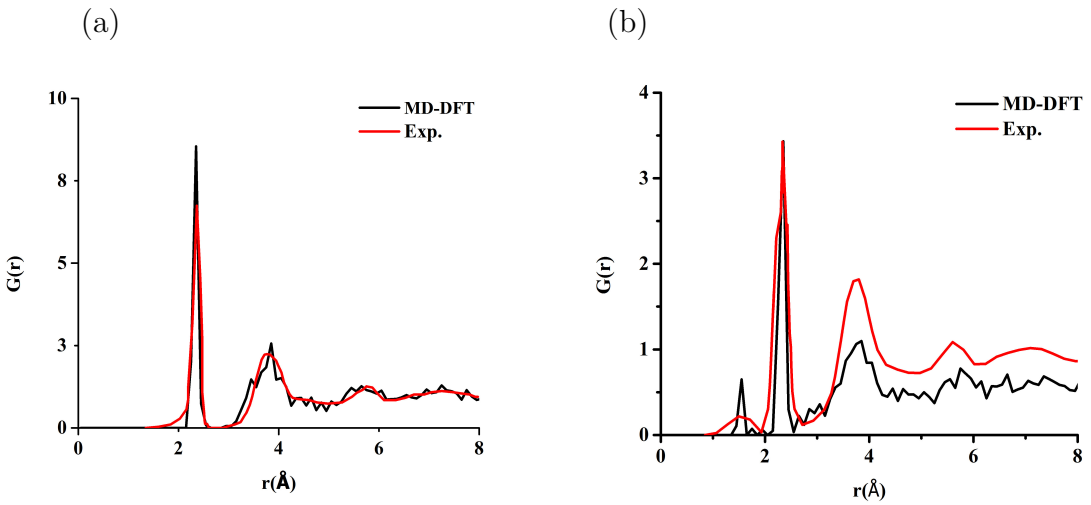

Figure 4.2: The calculated RDF (black lines) of a) a-Si and b) a-Si:H in comparison with experimental RDF (red lines) [6, 7].

4.2 Result

4.2.1 Hydrogen Addition Effect on the Atomic and Electronic Structure of a-Si

As grown, a-Si is typically highly defective and contains many undercoordinated Si atoms (dangling bonds) as well as significantly deviated Si-Si bond lengths and Si-Si-Si bond angles compared to bulk crystalline Si (c-Si) [136]. In this section, first we attempt to identify which of the structural defects in a-Si are primarily involved in the H addition from an energetic standpoint, and second we investigate how the electronic structure changes with this H addition. Toward this goal, we investigate the energy change of a-Si with inserting one or more hydrogen atoms to the modeled a-Si64 supercell obtained from MD and then optimized by the DFT method. For generating different initial configurations, the hydrogen atom was attached to a specific Si atom at a distance of 1Å in 6 different directions ($\pm$x, $\pm$y, and $\pm$z). From the chemical point of view, the distance of 1Å between the given Si atom and the H atom guaranties the presence of a bond between them. Since there are 64 Si atoms total in the supercell, and H atom attaches to a given Si atom in 6 different configurations, we therefore

generated 64×6=384 different initial configurations in order to perform further energy relaxation as discussed in the previous section. The energy of all the relaxed structures were compared and the structure corresponding to the lowest total energy was defined as the most stable one.

As mentioned before, there are no dangling bonds and two floating bonds (FB) in the supercell prepared by MD simulation. After optimizing this supercell using the DFT method, the energy of the final supercell is 8.23 eV less than that of the initial structure. We found that this huge stability is associated with appearing two dangling bonds (labeled here as Si#59 and Si#20) and removing two floating bonds in the supercell. This result shows that stable configurations of the amorphous structure do not necessarily mean no dangling bonds in the structure. Since we have two dangling bonds in the supercell, the H atom is conventionally expected to passivate the mentioned dangling bonds in the most stable configuration of a-Si64H. However, our structural analysis shows that, the most stable configuration of a-Si64H corresponds to a H atom bonded to Si#46, not to the dangling bond Si#59 or Si#20. The position of Si#46 in the a-Si structure is illustrated in Fig. 4.3. Although the Si#46 atom does not have a dangling bond, it is under a significant ring strain (RS) since it is shared between two unstable 4-fold rings. Ring strain exists when the chemical bonds form under abnormal angles which is the case for small rings such as 3 and 4-fold rings resulting in their abnormal chemical reactivity [137]. Due to this high ring strain, the bond shared between two rings is relatively longer (2.46Å) than the other bonds in the rings. A 3D electron density analysis showed that two bonds out of the four bonds involved with Si#46 have low electron density relative to the other bonds. Since the concentration of electronic charge in the bond region is characteristic of the strength of the covalent bonds, especially the bonds between identical atoms [138], the covalent bonds involved with Si#46 are therefore weak.

These weak covalent bonds might explain why H preferentially binds to the Si#46 site rather than the Si atom with the dangling bond [139, 140]. It is known that the bonds of large different strength to those which make up the perfect crystal could significantly change the local distribution of electronic energy levels [141]. Some of these altered energy levels are localized and located in within the band gap of the semiconductor [141]. In consistent with the argument, using the atom-projected densities of states (PDOS) analysis, we found that this Si atom creates highly dense mid-gap states close to the conduction band edge compared to the other Si atoms in the supercell. We also found that the H atom bonded to Si#46 results in removing one dangling bond (Si#20), which is very far from the H position in the supercell. Since the exsistance of dangling bonds in the a-Si is associated with disorder in the atomic structure, H atoms attached to Si atoms with highly SBs could reduce the disorder and consequently the dangling or floating bonds. This change in disorder may be another reason why H preferentially, in some cases, attaches to Si atoms with SBs rather than DBs. In fact, H atoms attached to Si atoms with SBs could tune both the short range and long range disorder. Tuning this disorder using H atoms provides a big degree of freedom to engineer the electronic structure of a-Si.

We also examined the atomic structure of a-Si:H, when a second H atom is inserted into the a-Si64H supercell. Our structural analysis shows that, in the most stable configuration, the inserted H atom is bonded to Si#59, which has a dangling bond. By inserting this second H atom to the supercell, all the dangling bonds disappear in the supercell. With continued insertion of H atoms to the supercell, we found again a sensitivity of Si atoms under bond or ring strain to hydrogen addition. For instance, in the case of inserting the third and fourth H atoms to the supercell, the H atom is bonded to the Si atoms in 4-fold rings. The bonds involved with these Si atoms are under either bond length strain or ring strain. Our calculations show the

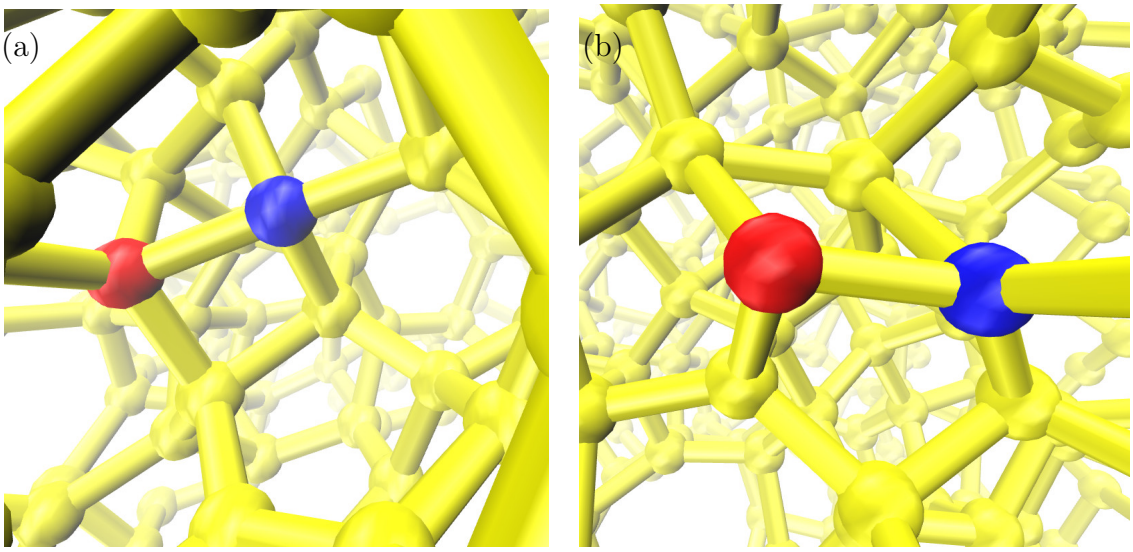

Figure 4.3: The position of a) Si#46 (blue colored) and Si#47 (red colored) and b) Si#20 (blue colored) and Si#53 (red colored) in a-Si structure.

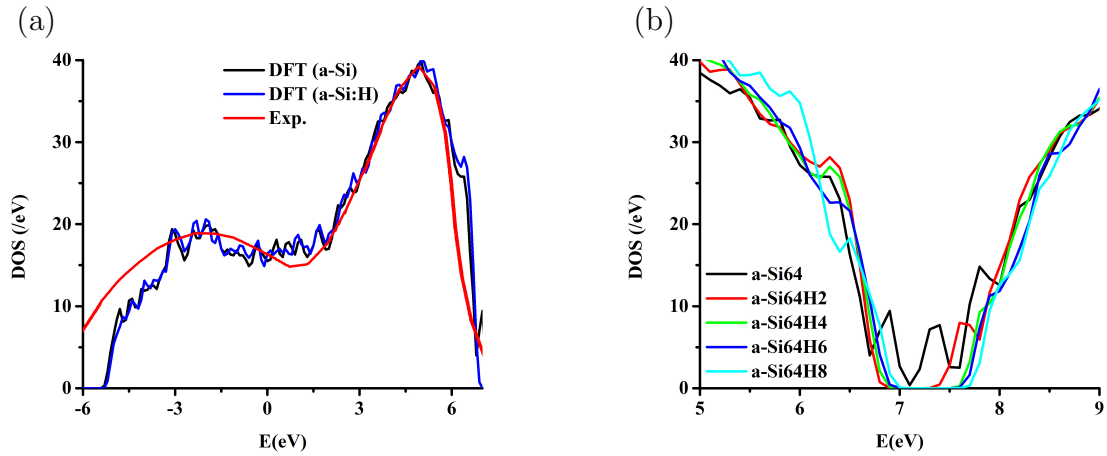

Figure 4.4: Calculated EDOS of a) the valence band of a-Si and a-Si:H in comparison with photoemision experiment [8] and b) a-Si:H close to the band gap in different H concentrations.

same trend for the case of having five (a-Si64H5) and six (a-Si64H6) H atoms in the supercells. In the most stable configuration, in both cases, the inserted H atom was added to the Si atoms under ring strain, one in a 4-fold ring and one shared between two 5-fold rings.

In all the a-Si:H cases studied, the energy difference between the first and

second most stable configurations was at least 0.1 eV, and therefore are quite stable even up to elevated temperatures. However, since a-Si:H is usually deposited by plasma deposition under highly non-equilibrium conditions, other less stable configurations would also appear within a particular volume of material [109]. However, these less stable configurations could be converted to more energetically stable ones with appropriate annealing process [133].

The details of the electronic properties of a-Si and a-Si:H materials are very important for their use in electronic and optoelectronic applications. We performed electronic structure calculations on a-Si and on the most stable configurations of a-Si:H. Figure. 4.12a illustrates the calculated electronic density of states (EDOS) plot of the a-Si and a-Si:H valence band compared to photoemission experimental results [8], where a good agreement is observed between experimental and computational results in terms of the hight and the location of the two characteristic peaks of a-Si and a-Si:H. This agreement provides further evidence (beside the RDF) in the accuracy of the amorphous structure produced by the MD-DFT method. From Fig. 4.12b, it is obvious that adding H atoms to the a-Si structure noticeably change the electronic structure close to the band gap, including a decrease the mid gap state density and an increase in the band gap, which is in agreement with experimental results. The decrease in the mid gap state density with H has been attributed to the passivation of the dangling bonds, the argument being that insertion of H into a-Si effectively decreases the number of dangling bonds and consequently removes the mid gap states in the a-Si EDOS. However, this argument is not always true. For example, we find that although all dangling bonds disappears after adding the second H atom to the supercell, additional H contains reduce the mid gap state and increase the band gap (See Fig. 4.12b). This mid gap states removal can be due to the replacement of relatively weak Si-Si bonds by a strong Si-H bonds. The formation of strong Si-H

bonds results from the interaction of the the shallow orbital of a-Si in the valance and conduction band edges with the H orbitals, which instead create electronic states deeper in valance and conduction bands.

We note that the band gap change is fast at relatively low H concentration, but this change becomes slower at higher H concentration. The band gap value becomes constant and even drops at a certain level of H concentration. Therefore, there should be an optimum value of H concentration in growing a-Si:H material, which is in good agreement with previous experiments [142].

4.2.2 Localized States due to Defects and Hydrogen Effect on Orbital Localization

The atomic structure and the degree of disorder plays an important role in determining the localization of electronic states in a material. In this section, we investigate which structural defects are responsible for orbital localization in a-Si and how H addition affects this localization. In order to do that, localization of the Kohn-Sham orbitals was first studied in detail for the basic a-Si model without H, followed by study of the same localization with H.

The localized properties of an eigenstate can be numerically quantified using the inverse participation ratio (IPR). The IPR for an eigenstate Ψ_n is given as

$$IPR(\Psi_n) = \frac{\Sigma_{i=1}^{N} a_{ni}^4}{(\Sigma_{i=1}^{N} a_{ni}^2)^2} \tag{4.1}$$

where a_{ni} is the coefficient of i^{th} basis set orbital in n^{th} Kohn-Sham orbital Ψ_n ($\Psi_n = \Sigma_{i=1}^{N} a_{ni}\phi_i$). The IPR for an ideally extended state is zero and for an ideally localized state (on one basis orbital) is one. Therefore, higher IPR signifies a higher degree of localization. Here, the Kohn-Sham wavefunctions for a-Si structures were obtained using DFT calculation, and in order to quantify the localization properties, the IPR values were computed from Eq. 4.1. In the rest of this section, the Kohn-Sham wave function of the localized states is discussed in detail.

The following functionals show the Kohn-Sham wavefunctions of the ten most localized electronic states (in order of increasing IPR value) lying in the gap and valence band tail of a-Si.

$$
\begin{aligned}
\Psi_1 &= 0.145\phi_{46P_z} + 0.040\phi_{48P_z} + 0.036\phi_{62P_x} + ... \\
\Psi_2 &= 0.126\phi_{46P_z} + 0.030\phi_{26P_y} + 0.029\phi_{47P_x} + ... \\
\Psi_3 &= 0.125\phi_{46P_z} + 0.055\phi_{47P_x} + 0.030\phi_{26P_y} + ... \\
\Psi_4 &= 0.111\phi_{46P_z} + 0.027\phi_{48P_z} + 0.026\phi_{4P_z} + ... \\
\Psi_5 &= 0.123\phi_{46P_z} + 0.033\phi_{26P_y} + 0.033\phi_{47P_x} + ... \\
\Psi_6 &= 0.121\phi_{46P_z} + 0.042\phi_{26P_x} + 0.032\phi_{48P_z} + ... \\
\Psi_7 &= 0.117\phi_{46P_z} + 0.043\phi_{48P_z} + 0.034\phi_{62P_x} + ... \\
\Psi_8 &= 0.103\phi_{46P_z} + 0.030\phi_{11P_y} + 0.028\phi_{48P_z} + ... \\
\Psi_9 &= 0.127\phi_{46P_z} + 0.058\phi_{26P_y} + 0.040\phi_{7P_x} + ... \\
\Psi_{10} &= 0.106\phi_{46P_z} + 0.050\phi_{47P_x} + 0.033\phi_{43P_x} + ...
\end{aligned}
\tag{4.2}
$$

Here, the notation of ϕ_{nx} is used to describe the basis set orbital where "n" indicates the n^{th} Si atom in the supercell and "x" indicate the type of atomic orbital from the valance layer of Si. For instance, ϕ_{46P_z} stands for the P_z atomic orbital from 46^{th} Si atom in the supercell. We also use the short hand label of Si#n to indicate the n^{th} Si atom.

Eq. 4.2 clarifies that Si#46 has the largest contribution in constructing the ten first most localized electronic states. The position of Si#46 in the a-Si structure was previously shown in Fig. 4.3. As previously mentioned, this Si atom is under high ring strain due to being shared between two small 4-fold ring. Although there are two dangling bonds in the supercell, atom Si#46 with abnormal bond angles has the most important role in creating localized states in the gap and valence band tail. This result indicates the Si atoms without DB may appear to contribute most to the

localized states (with the highest localization) in the band tail and midgap region, rather than DBs.

In order to further examine the contribution of Si atoms with SB and RS in orbital localization, the localization of states within the conduction band tail were also investigated. The following Kohn-Sham wavefunctions describes the ten most localized electronic state of a-Si locating in the conduction band tail based on the atomic orbitals.

$$
\begin{aligned}
\Psi_1 &= 0.133\phi_{20P_y} + 0.065\phi_{53P_y} + 0.052\phi_{59P_y} + ... \\
\Psi_2 &= 0.127\phi_{46P_z} + 0.084\phi_{47P_x} + 0.069\phi_{44S} + ... \\
\Psi_3 &= 0.114\phi_{47P_x} + 0.069\phi_{46P_z} + 0.048\phi_{44P_x} + ... \\
\Psi_4 &= 0.125\phi_{47P_x} + 0.078\phi_{46P_z} + 0.060\phi_{44P_x} + ... \\
\Psi_5 &= 0.134\phi_{20P_y} + 0.073\phi_{53P_y} + 0.064\phi_{59P_y} + ... \\
\Psi_6 &= 0.130\phi_{20P_y} + 0.054\phi_{53P_y} + 0.053\phi_{4P_z} + ... \\
\Psi_7 &= 0.127\phi_{20P_y} + 0.060\phi_{53P_y} + 0.043\phi_{4P_z} + ... \\
\Psi_8 &= 0.121\phi_{46P_z} + 0.079\phi_{47P_x} + 0.040\phi_{44S} + ... \\
\Psi_9 &= 0.119\phi_{47P_x} + 0.064\phi_{44P_x} + 0.062\phi_{46P_z} + ... \\
\Psi_{10} &= 0.117\phi_{47P_x} + 0.080\phi_{46P_z} + 0.048\phi_{44P_x} + ...
\end{aligned}
\tag{4.3}
$$

By paying close attention to the wavefunctions, one can figure out that Si#46 and Si#47 have the largest contribution in the most of localized states ($\Psi_2, \Psi_3, \Psi_4, \Psi_8, \Psi_9, \Psi_{10}$) located in the conduction band tail. Fig. 4.3 shows the location of Si#47 in the a-Si structure which has been shared between two 4-folded rings and is bonded to Si#46 with a relative weak bond (Fig. 4.3). Another atom which appears important in creating localized states ($\Psi_1, \Psi_5, \Psi_6, \Psi_7$) is Si#20. As indicated in Fig. 4.3, Si#20 atom has a dangling bond and is also under a 4-folded ring strain. it is worth men-

tioning here that since 4-folded rings in a-Si network are not perfect rings, some of the atoms in these rings are under higher angle strain than the others. Therefore, Si#53 (Fig. 4.3) which is in the 4-folded ring has higher contribution than the other atoms in the ring in the localized states($\Psi_1, \Psi_5, \Psi_6, \Psi_7$) due to experiencing higher ring strain.

In order to further verify our findings, the contribution of each atom in the localization of all the electronic states in the mobility gap of a-Si was also calculated as following:

$$IPR_k = \Sigma_{n=1}^{N} IPR_{nk} \tag{4.4}$$

Where N is the number of all the electronic states in the mobility gap of a-Si and IPR_{nk} is the contribution of k^{th} atom of the system in the orbital localizations of n^{th} Kohn-Sham orbital. The IPR_{nk} quantity can be easily calculated using the following equation:

$$IPR_k = a_{ni}^4 / (\Sigma_{i=1}^{I} a_{ni}^2)^2 \tag{4.5}$$

Where, as before, a_{ni} is the coefficient of i^{th} basis set orbital coming from the k^{th} atom in n^{th} Kohn-Sham orbital Ψ_n ($\Psi_n = \Sigma_{i=1}^{N} a_{ni}\phi_i$). Fig. 4.14 shows IPR_k values for each atom. As indicated, Si#20, Si#46 and Si#47 (Si atoms with strained bonds) have very large contributions almost as large as Si#59 (Si atom with dangling bond) in the localization of all the electronic states within the mobility gap of a-Si.

As a result of this section, Si atoms involved with strained-bonds (deviated bond lengths or bond angles) play a crucial role, not necessarily less than dangling bonds, in the localization of the orbitals in the mobility gap of a-Si. These results provide a support to the conclusions of recently studies revealing the importance of strained-bonds participating in localized states [118, 121, 143].

We also examined the effect of H addition on orbital localization. Fig. 4.6

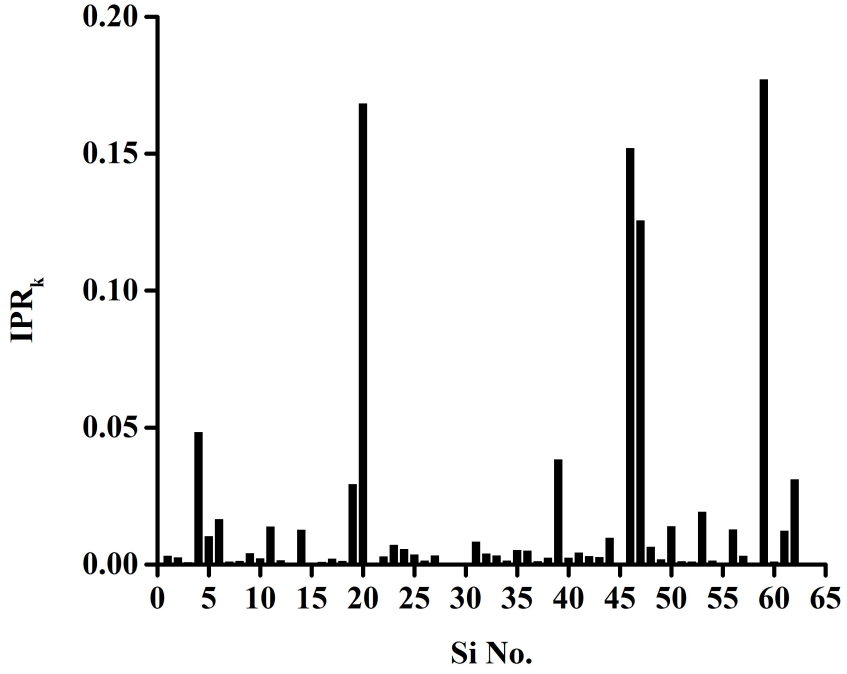

Figure 4.5: The relative contribution of each atom in the orbital localization of the modeled a-Si supercell containing 64 atoms prepared by medium cooling rate.

shows the calculated IPR of a-Si in comparison with a-Si:H in different H concentrations. As clearly seen, there is a relative sharp transition between the high and low IPR values (localized and extended electronic states) identifying the existence of the mobility edges in both valance and conduction bands. The general form of the IPR plot is in agreement with previous theoretical and computational studies [122, 136].

From the comparison between the IPR plots presented in Fig. 4.6, it can be noticed that the localization of the Kohn-Sham orbitals significantly decrease by adding hydrogen atoms to the system. Since our H atoms are mostly added to the atoms under ring strains, therefore decrease in orbital localization is mostly due to removing strained bonds rather than dangling bonds. This lower localization could explain the better transport properties observed for a-Si:H in comparison with a-Si, experimen-

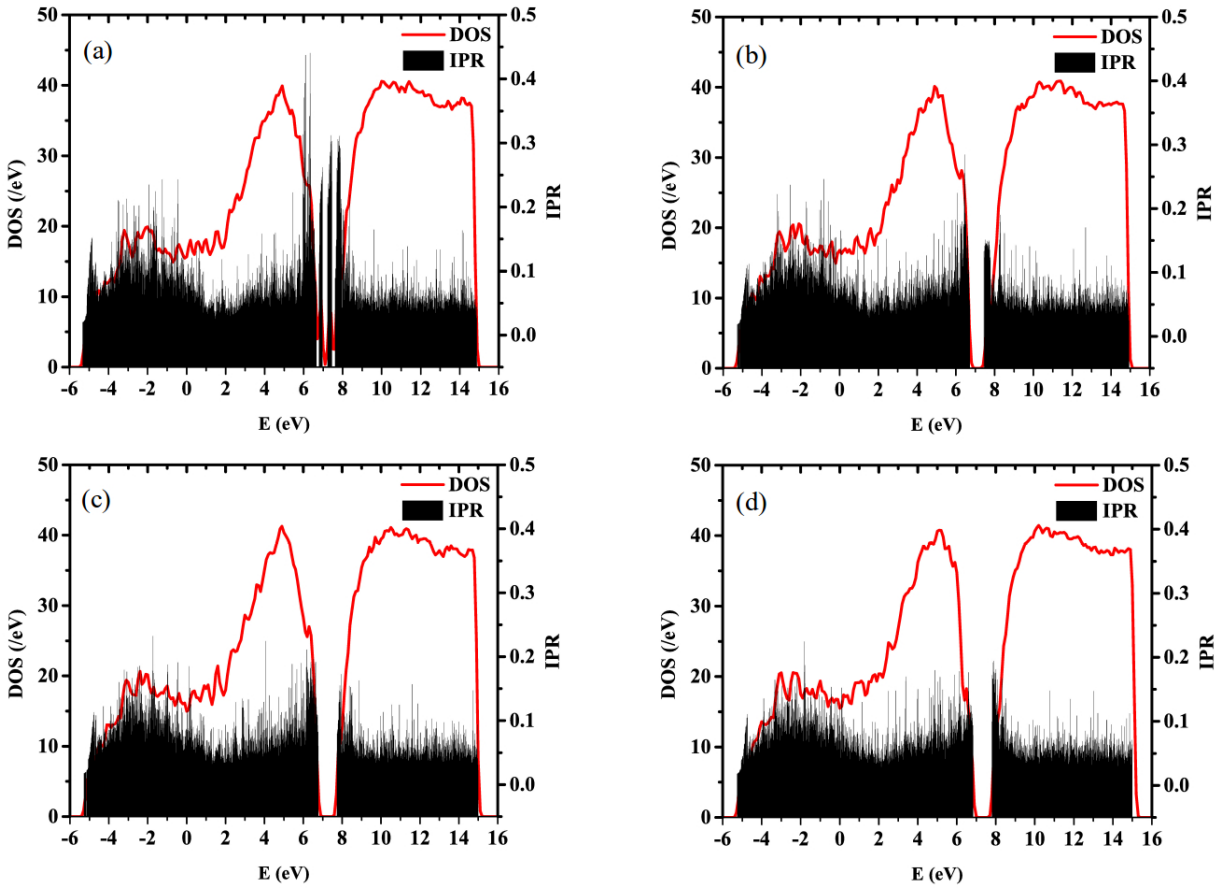

Figure 4.6: The calculated IPR of a-Si:H with a) 0%, b) 3.12%, c) 6.25%, and d) 12.5% H atomic concentration.

tally [109]. It is noticeable that H atoms decrease the localization in the conduction band tail more than that in the valence band tail. Since the valence band tail electronic states are responsible for hole transport and conduction band tail electronic states are responsible for electron transport, more localization in the valance band tail could cause intrinsic a-Si:H to transport electrons more easily than holes [144]. Due to this difference in localization between electrons and holes, it is possible that a-Si:H can act as a selective contact for transporting electron and trapping holes for low hydrogen concentrations [118].

We observed an inverse trend in localization for a-Si:H at high H concentra-

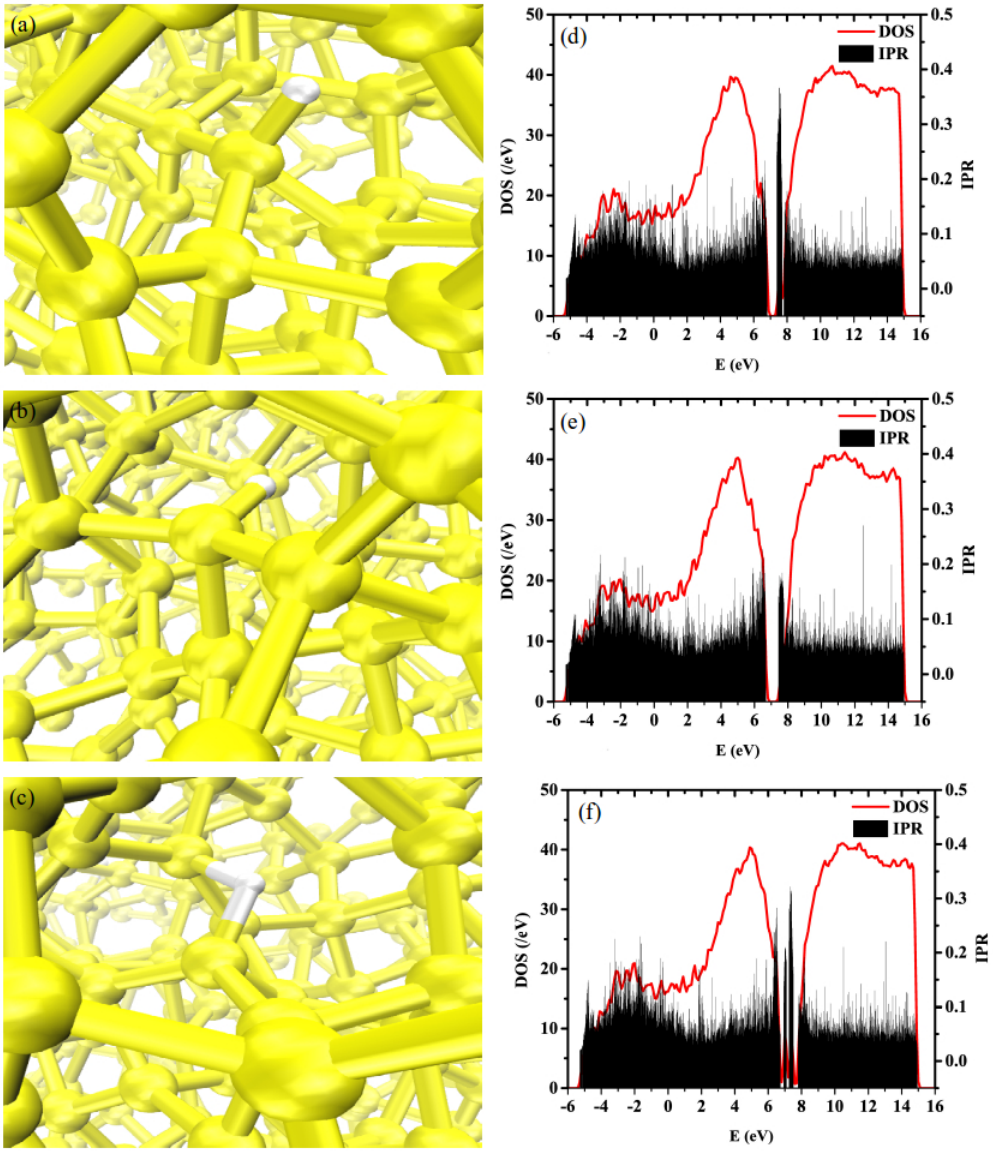

Figure 4.7: The position of H in the a) second, b) third, and c) forth stable configuration of a-Si64H2 (3.16% H atomic concentration) and their corresponding calculated IPR in the d) second, e) third, and f) forth stable configuration.

tions. Fig. 4.6d shows the calculated IPR of a-Si:H with 12.5% H atomic percent. As seen in the figure, the localization of the orbitals in conduction band tail is higher than that in valence band tail, against a-Si:H with low atomic H concentration. This results consequently suggest that a-Si:H can act as a electron selective contact at low

H concentration and act a hole selective contact at high H concentration.

4.2.3 The effect of H position and different configurations on orbital localization

For examining the effect of the H position on the localization of electronic states in a-Si:H, we perform electronic structure calculations on less stable configurations, i.e. for the case of having two H atoms in a-Si64 supercell (3.16% H atomic concentration). In this case, the first H atom is bonded to the Si#46 for all configuration and the second H atom is bonded to different Si atoms in different configurations. As previously mentioned, in the most stable configuration, the second atom is bonded to the Si atom with dangling bond Si#59. However, in less stable configurations, the H atom is bonded to different Si atoms with different bonding configurations. Fig. 4.7 shows the structure of a-Si64H2 in its second, third, and forth most stable configurations and their corresponding IPR plots.

By comparing between the IPR plots of the most stable configuration, Fig. 4.6b, and IPR of the next stable configuration in Fig. 4.7, one can easily note the huge impact of the H position on the localization of orbitals in a-Si:H materials. As clearly seen from the figures, generally speaking, the localization of orbitals in a-Si:H increases in the less stable configurations. This localization increase is especially obvious in the second and forth most stable configurations. Therefore, here we just focus on second and forth most stable configurations.

In the second stable configuration, the second H is bonded to the Si atom involved in 4-folded ring instead of the Si#59. In this case, compared with the most stable configuration, the localization of orbitals in the conduction band tails is more than that in the valance band tails. Therefore, in the less stable structures, a-Si:H can act as a selective contact for holes, in terms of transport.

In the fourth stable configuration, we find that the H atom creates a bridge

between two Si atoms. Fig. 4.7f shows the calculated IPR of forth configuration versus electronic state energies. As clearly seen from the figure, the H atom in the bridge position creates many localized states in the gap of a-Si and increases the localization of valence band tail orbitals. The analysis shows that the Si atoms connected by the H bridge have the largest contribution to localized states.

4.3 Simulation the electronic structure of a-Si and a-Si:H using larger supercells

In order to check the consistency of the obtained results, the same DFT simulations were performed on a supercell containing 216 Si atoms. A diamond starting atomic structure of crystalline Si with a lattice constant of a 0 = 5.46 Åwas constructed using a cubic supercell with the dimension of $a = b = c = 3a_0$, which was periodically repeated in 3D space to generate an infinite network of atoms. This time, in contrast to a-Si64 supercell, a_0 was chosen in such a way that the mass density of our supercell is equal the mass density of a-Si measured by experiments [52, 53]. Then, we carried out a simulated melting and quenching process exactly the same as before. Finally, the structure was fully optimized using DFT relaxation calculation.

Fig. 4.8 illustrates the atomic structures of an a-Si supercell containing 216 Si atoms obtained from MD simulation and DFT relaxtion calculation. Based on the periodic structure formed from the supercell in Figure 1, we found three dangling bonds and three floating bonds per supercell with an assumed Si-Si cutoff bond length of 2.58 Å, which is 10% longer than the experimental Si-Si bond length (2.35 Å). The structure mostly displays stable 5, 6 or 7 fold rings, and there are no large voids or holes inside it. The average Si-Si bond length is 2.367 Åwith an rms value of 0.0592 Åand the average Si-Si-Si bond angle is 107.75° with an rms value of 15.486°. In the crystalline form of Si, the Si-Si bond length is 2.35 Åand the Si-Si-Si bond angle is 109.471°. The structural properties of the generated a-Si are given in Table 1.

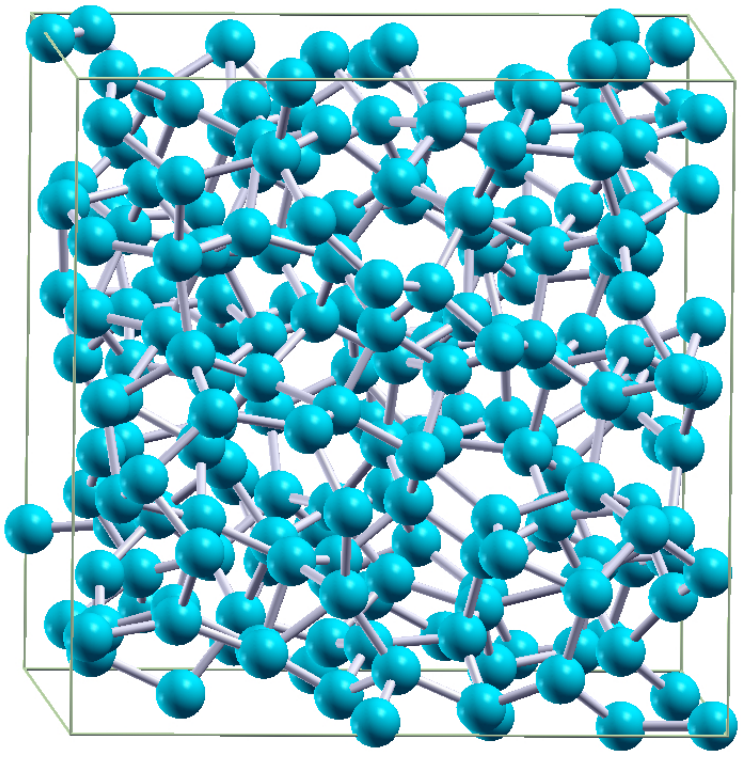

Figure 4.8: The atomic structure of the a-Si216 supercell.

As before, The reliability of the structures obtained from the MD-DFT protocol were checked by calculating the Radial Distribution Function (RDF) using the LAMMPS program. Figure 4.9 shows the calculated RDF of the a-Si structures compared the experimental results [6, 7]. As can be seen, both the calculated and ex-

Table 4.1: Structural and electronic properties of a-Si supercells with different H concentrations: mean first-neighbor distance r, standard deviation of the first-neighbor distance σ, mean bond angle θ, standard deviation of bond angle σ_θ. Lengthes and energies are in Å and kJ/mol units, respectively.

Supercell	r	σ_r	θ	σ_θ	**DB**	ΔE
a-Si216	2.3672	0.0592	107.75	15.48	3	0
a-Si216H2	2.3660	0.0587	108.06	13.95	5	-3300
a-Si216H4	2.3634	0.0564	108.13	13.78	4	-6400
a-Si216H6	2.3629	0.0559	108.20	13.62	6	-9500

perimental RDF exhibit a strong peak at 2.3 Å and two weak peaks around 4 and 6 Å.

For obtaining an atomic structural model of a-Si:H with H at%=0.5 (a-Si216H), the a-Si supercell with 216 atoms obtained from MD is first relaxed using DFT methods and then a single hydrogen atom is added to this fully relaxed supercell. Since there are 216 possible ways to bond a hydrogen atom to the supercell (the hydrogen atom can be bonded to each of the 216 Si atoms), DFT ion relaxation calculations were carried out on all 216 possible configurations. The configuration with the lowest energy computed by the ion relaxation calculations is chosen as the most stable configuration in order to perform further calculations. The same procedure was repeated for finding the most stable configuration of a-Si:H with H at%=1 (a-Si216H2), with the difference being that a single hydrogen atom was added to the most stable configuration of a-Si:H with H at%=0.5. The same strategy was used for generating a-Si:H with higher hydrogen concentrations. We changed the dimension of the supercell after each H addition in such a way that the mass density of the supercell is kept the same

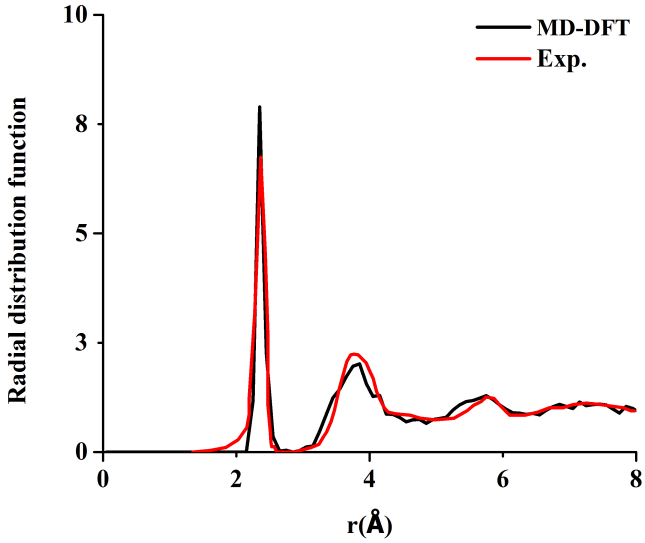

Figure 4.9: The calculated RDF (black lines) of a-Si in comparison with experimental RDF (red lines) [6, 7].

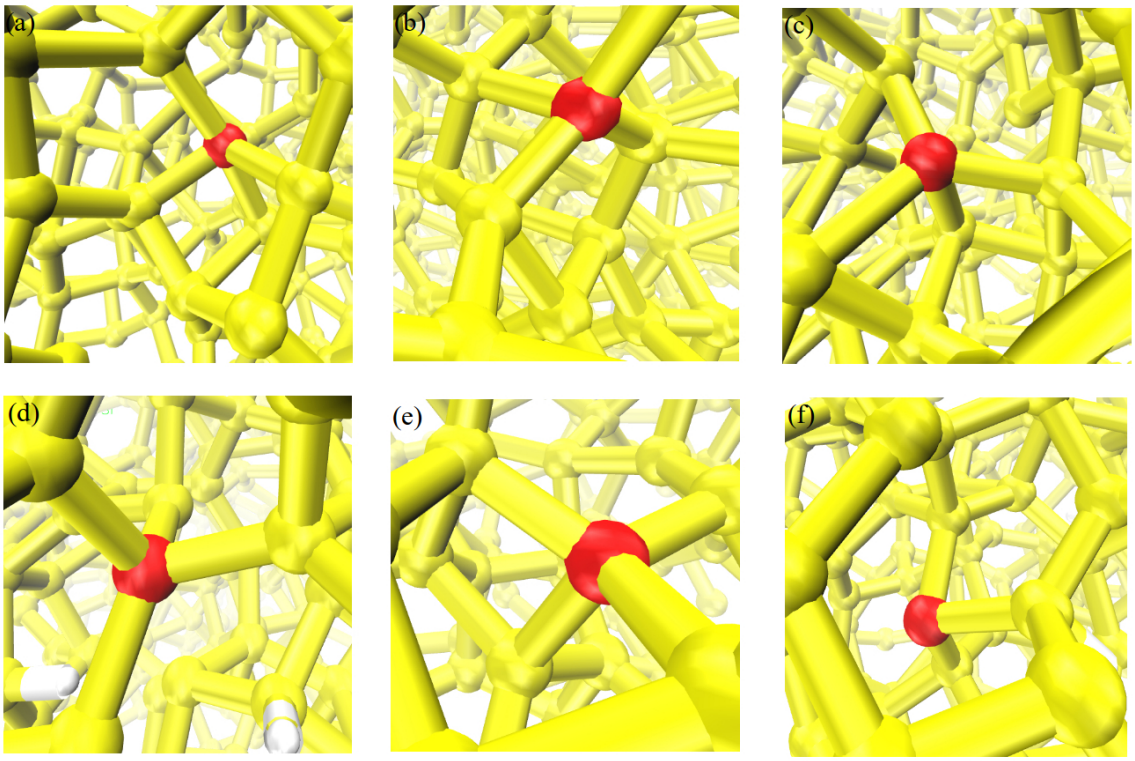

Figure 4.10: The position of Si atoms (red colored) in a-Si structure involved in H addition in a-Si:H with the H atomic percent of a) 0% (a-Si216), b) 0.46% (a-Si216H), c) 0.92% (a-Si216H2), d) 1.37% (a-Si216H3), e) 1.82% (a-Si216H4), and f) 2.26% (a-Si216H5).

as the mass density of a-Si:H in experimental setup [145]. Here, the short hand label of a-Si216Hn was used to determine the number of H atoms in the supercell where "n" indicates the number of H atoms in the a-Si supercell containing 216 Si atoms. We also use the label of Si#n to indicate the n^{th} Si atom in the supercell.

As before, first we attempt to identify which of the structural defects in a-Si are primarily involved in the addition of H from an energetic standpoint, and second we investigate how the electronic structure changes with this H addition. Towards this goal, we investigate the energy change of a-Si with insertion of hydrogen atoms one by one to the modeled a-Si216 supercell obtained from MD simulation and DFT relaxation calculations.

As mentioned before, we found three dangling bonds (labeled here as Si#9, Si#57 and Si#158, illustrated later in Fig. 4.15) and three floating bonds (FBs) in the pure a-Si supercell. Once a H atom is inserted to the supercell, the H atom is traditionally expected to passivate one of these dangling bonds in the most stable configuration of a-Si216H. However, our calculations show that the most stable configuration of a-Si216H corresponds to a H atom bonded to a Si atom (illustrated in Fig. 4.10a) under both bond angle and bond length strain, not to one of the dangling bonds. Bond angle and bond length strain exist when the chemical bonds form under non ideal angles and lengths [137]. The average deviation from the ideal bond angle and bond length involved with the targeted Si atom are 24° and 0.09 Å, respectively. We found that binding a H atom to this Si atom results in removing one of the FBs which is spatially separated from the H position in the supercell. While the number of dangling bonds remain the same, their positions in the a-Si216 supercell change (Fig. 4.14). We also found that attaching a H atom to the aforementioned Si atom causes a decrease in the total energy of a-Si by 1600 kJ/mol which is much higher than a Si-H bond energy. Our calculations show that if H only passivates an isolated dangling bond while the rest of a-Si network is essentially rigid, then the total energy of a-Si would decrease by only 440 kJ/mol. Therefore, attaching a H atom to a strained bond makes the whole a-Si network more stable than attaching it to an isolated dangling bond.

We also examined the atomic structure of a-Si:H, when a second H atom is inserted into the a-Si216H supercell. Our calculations show that in the most stable configuration, the inserted H atom is again bonded to an atom under bond strain which has no dangling bond or floating bond. The position of this Si atom is depicted in Fig. 4.10b. The average deviation from ideal bond angle and bond length involved with this Si atom are 12° and 0.04 Å, respectively. By inserting the second H atom

to the supercell, the number of dangling bonds increases to 5 per supercell and the number of floating bonds remains the same as a-Si216. However, we find that the a-Si network becomes stabilized by 3700 kJ/mol which much higher than the bond energy (880 kJ/mol) of two Si-H bonds. This high stabilization could be due to an increase in the degree of structural order in the a-Si network. Table. 4.1 illustrates the structural properties of the a-Si supercell containing 216 with different H concentration. As seen, the average bond length and average bond angle get closer to their ideal values with inserting H atoms to the supercell. With continued insertion of H atoms to the supercell, we found again a sensitivity of Si atoms under bond angle or bond length strain to hydrogen addition. Fig. 4.10c, 4.10d, 4.10e, and 4.10f show the Si atoms which were the target of H attack with inserting a third, forth, fifth and sixth H atom, respectively, to the supercell. Only for the case of inserting the sixth H atom, is the H atom bonded to a Si atom with a dangling bond. In all those cases, we observe a change in the number of dangling bonds and floating bonds in the supercell although H atom bonds to Si atoms with strained bonds (Table. 4.1). We also observe an improvement in the degree of structural order and a decrease in the excess energy of the a-Si network after each H addition to the strained bonds (Table. 4.1). These results together show, in the most stable configuration, that H atoms do not necessarily attach to an isolated dangling bond, but it might attach to Si atoms under bond strain. The H interaction with strained bonds globally change the structure of a-Si which also changes the number and the position of the dangling and floating bonds. This global structural change is associated with releasing strain from the whole a-Si network, which consequently causes stabilization much higher than the bond energy of individual Si-H bonds.

Figure 4.11 shows a typical histogram of the relative energy distribution of different configurations resulted from H addition (in this case the configurations re-

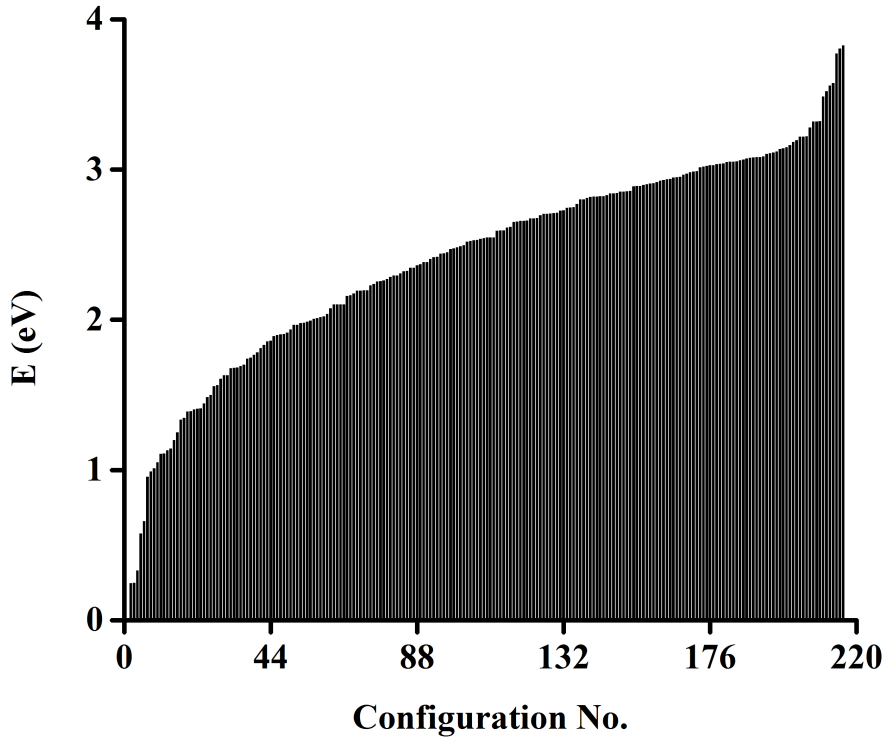

Figure 4.11: The histogram of the relative energy distribution of different configurations resulted from one H atom addition to the a-Si216 supercell.

sulted from one H atom addition to the a-Si216 supercell). The energy of the most stable configuration is set 0 eV. In almost all the a-Si:H cases studied, the energy difference between the first and second most stable configurations was at least 0.25 eV (10kT), and therefore are quite stable at room temperature. In order to ensure that this energy ordering is not dependent on the DFT method, we also use the Perdew-Burke-Ernzerhof (PBE) exchange-correlation functional [105, 146] for calculating the energy of the first and second most stable configurations. We obtain almost the same energy difference and energy ordering for the first and second stable configurations when we use the PBE functional in the DFT calculations.

The details of the electronic properties of a-Si and a-Si:H materials are very

important for their application in electronics and optoelectronics. In order to investigate the electronic properties of a-Si and H atom effect, we performed electronic structure calculations on a-Si and on the most stable configurations of a-Si:H. Figure. 4.12a illustrates the calculated electronic density of states (EDOS) plot of the a-Si and a-Si:H valence band compared to photoemission experimental results [8], where a good agreement is observed between experimental and computational results in terms of the height and location of the two characteristic peaks of a-Si and a-Si:H. This agreement provides further evidence (beside the RDF) of the accuracy of the amorphous structure produced by the MD-DFT method. From the Fig. 4.12a, one can see that the effect of hydrogenation is small on the EDOS of the valence band of a-Si. However, looking in detail at the EDOS close to the valence band edge (Fig. 4.12b), it reveals that adding H atoms to the a-Si structure noticeably changes the electronic structure around the band gap. This change mostly includes a decrease in the mid-gap state density, and consequently an increase in the band gap which is in agreement with experimental trends (although the actual Si bandgap is smaller than the experimental value due to well-known issues of normal DFT). The decrease in the mid-gap state density with H has been attributed to the passivation of the dangling bonds, the argument being that the insertion of H into a-Si effectively decreases the number of dangling bonds and consequently removes the mid-gap states in the a-Si EDOS. However, we find the actual picture is more complicated. From Table 1, it is obvious that the number of dangling bonds in all the a-Si:H supercells are more than the number of dangling bonds in the a-Si supercell without H, however the density of midgap states in the electronic structure of a-Si:H is less than that in the electronic structure of a-Si (Fig. 4.12b). Therefore, we did not find any correlation between the number of dangling bonds in the atomic structure of a-Si:H and the density of midgap states in the electronic structure of a-Si:H. This mid-gap state reduction may be at-

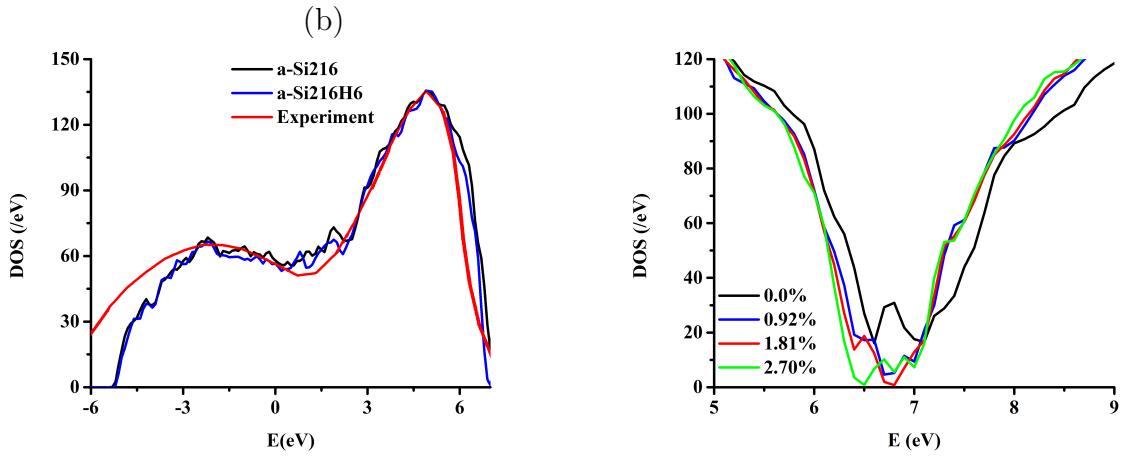

Figure 4.12: Calculated EDOS of a) the valence band of a-Si and a-Si:H in comparison with photoemision experiment [8] and b) a-Si:H close to the band gap for different H concentrations 0% (a-Si216), 0.92% (a-Si216H2), 1.82% (a-Si216H4), and 2.70% (a-Si216H6).

tributed to increasing structural order (Table. 4.1) of the network by H insertion [98]. Increasing the structural order leads to strain release from the whole a-Si structure and leads to the replacement of weak strained Si-Si bonds (which could be the source of midgap states) by strong Si-Si bonds. Another reason for midgap state reduction may be due to the replacement of relatively weak Si-Si bonds by strong Si-H bonds [141]. The formation of strong Si-H bonds results from the interaction of the the shallow orbital of a-Si in the valence and conduction band edges with the H orbitals, which instead create deeper electronic states in the valence and conduction bands. To this end, we believe that the change in excess energy stored in the amorphous network relative to the c-Si gives a better description of the a-Si atomic network than the number of dangling bond, as proposed in previous studies [147].

Due to the the presence of structural defects in the atomic structure of an amorphous material, the mobility of holes and electrons in the states close to the valence and conduction band edges are much lower compared to the nonlocalized extended states within the valence and conduction bands, where the carriers are con-

sidered free. The energy separation of localized and nonlocalized states is rather sharp and, consequently, this dividing energy is termed the mobility edge [109]. The energy difference between the valence-band mobility edge and conduction-band mobility edge is the so-called mobility gap. Electronic transport in a-Si and a-Si:H is strongly affected by the carriers inside the localized states within the mobility gap. Hence, in this section, we investigate the orbital localization in a-Si and a-Si:H and the structural defects that are responsible for orbital localization in the mobility gap of a-Si and H addition effects on this localization.

The localized properties of an eigenstate can be numerically quantified using the inverse participation ratio (IPR) [148]. The IPR for an eigenstate Ψ_n is given as

$$IPR(\Psi_n) = \frac{\Sigma_{i=1}^{N} a_{ni}^4}{(\Sigma_{i=1}^{N} a_{ni}^2)^2} \tag{4.6}$$

where a_{ni} is the coefficient of the i^{th} basis set orbital in the n^{th} Kohn-Sham orbital Ψ_n ($\Psi_n = \Sigma_{i=1}^{N} a_{ni}\phi_i$). The IPR for an ideally extended state is zero, and for an ideally localized state (on a one basis orbital) is one. Therefore, higher IPR signifies a higher degree of localization. Here, the Kohn-Sham wavefunctions for a-Si structures were obtained using DFT calculation, and in order to quantify the localization properties, the IPR values were computed from Eqn. 4.6.

Figure 5.4 shows the calculated IPR of a-Si in comparison with a-Si:H for different H concentrations. As clearly seen, there is a relatively sharp transition between the high and low IPR values (localized and extended electronic states) identifying the existence of the mobility edges in both valence and conduction bands. The general form of the IPR plot is in agreement with previous theoretical and computational studies [122, 136]. Here, we consider the mobility gap of a-Si and all a-Si:H structures from 6.0-8.0 eV, since most highly localized states are located in this interval.

From the comparison between the IPR plots presented in Fig. 5.4, we note that

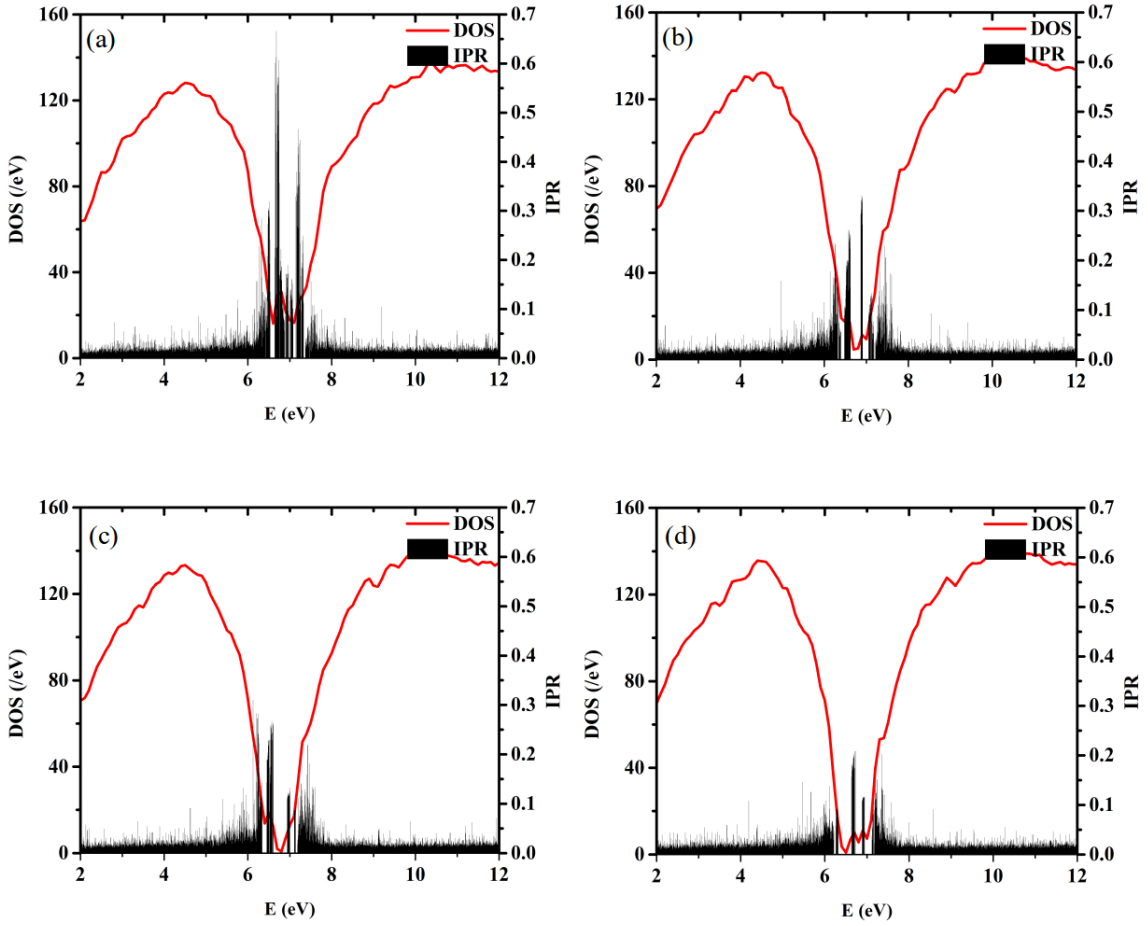

Figure 4.13: The calculated IPR of a-Si:H with a) 0% (a-Si216), b) 0.92% (a-Si216H2), c) 1.82% (a-Si216H4), d) 4.69%, and e) 2.70% (a-Si216H6) H atomic concentration.

the localization of the Kohn-Sham orbitals significantly decreases by the addition of hydrogen atoms. Since the H atoms add primarily to the atoms under bond strain, the decrease in orbital localization is primarily due to removing strained bonds rather than dangling bonds. Localized states strongly influence the effective carrier mobility in terms of scattering centers and hopping conduction [149]. Indeed, in the case of a-Si and a-Si:H, it has been experimentally shown that both the electron and hole mobilities are trapped controlled [150, 151]. Therefore a lower degree of localization is consistent with the observation of higher electron and hole mobility in a-Si:H compared to a-Si experimentally [26, 109, 118, 144]. We note that H atoms change the

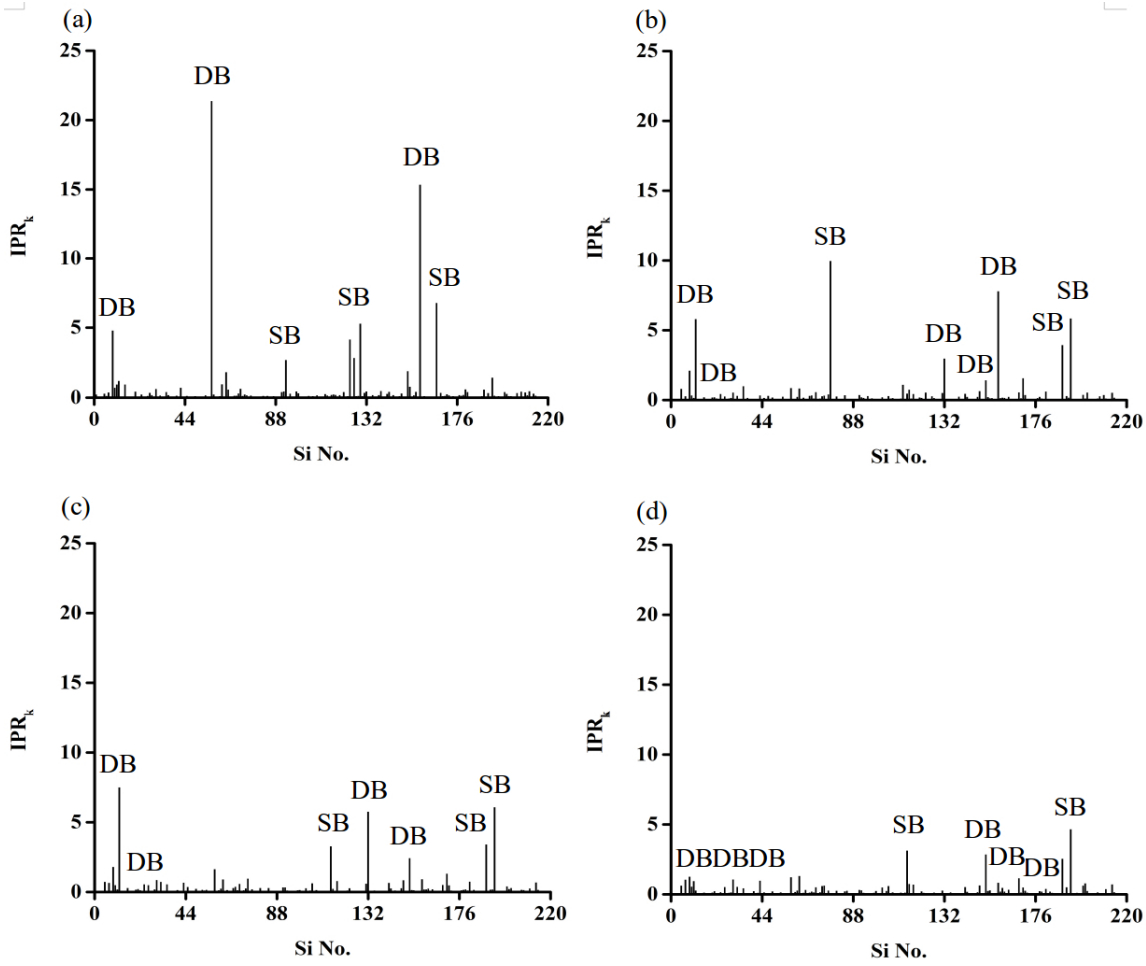

Figure 4.14: The relative contribution of each atom in the orbital localization of the modeled a-Si:H supercell with a) 0% (a-Si216), b) 0.92% (a-Si216H2), c) 1.82% (a-Si216H4), d) 4.69%, and e) 2.70% (a-Si216H6) H atomic concentration.

orbital localization inside the mobility gap much more than that outside the mobility gap. This shows that H atoms interact mostly with shallow orbitals close to the valence and conduction band edges of a-Si and is almost inert to the orbitals far from the valence and conduction band edges.

In order to investigate which structural defects are important in the orbital localization, the contribution of each atom in the localization of all the electronic

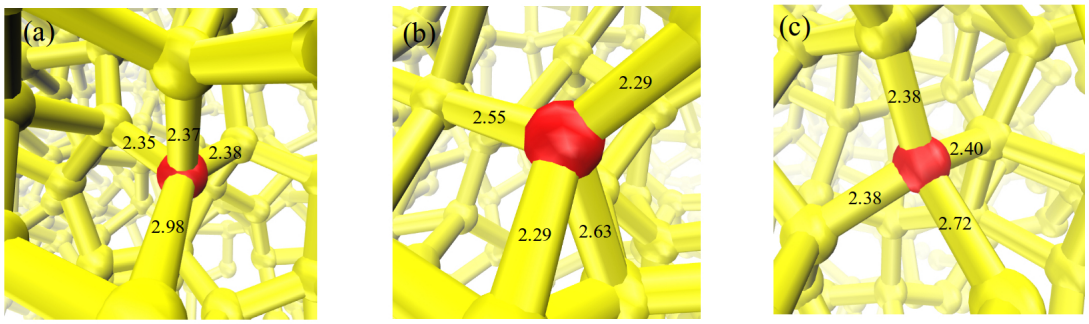

Figure 4.15: The position of a) Si#57 b) Si#158 and c) Si#9 atoms (illustrated with red color) in the a-Si216 supercell and the bond lengths associated with them. All the lengths are in angstrom unit.

states in the mobility gap (6.0-8.0 eV) of a-Si was calculated as follows:

$$IPR_k = \Sigma_{n=1}^{N} IPR_{nk}, \tag{4.7}$$

where N is the total number of electronic states in the mobility gap of a-Si, and IPR_{nk} is the contribution of the k^{th} atom of the system of the orbital localizations of n^{th} Kohn-Sham orbital. The IPR_{nk} can be calculated using the following equation:

$$IPR_{nk} = a_{ni}^4 / (\Sigma_{i=1}^{I} a_{ni}^2)^2, \tag{4.8}$$

where, as before, a_{ni} is the coefficient of i^{th} basis set orbital coming from the k^{th} atom in the n^{th} Kohn-Sham orbital Ψ_n ($\Psi_n = \Sigma_{i=1}^{N} a_{ni}\phi_i$). Figure 4.14 shows the IPR_k values for a-Si and a-Si:H with different hydrogen concentration. As seen, there are several strong peaks in the IPR_k graph of a-Si (Fig. 4.14a). Our structural analysis shows that the two strongest peaks are related to two of the DBs (Si#57 and Si#158) out of three DBs (Si#57, Si#158, and Si#9) present in the a-Si216 supercell (Fig. 4.15). This observation is in agreement with the common belief that dangling bonds cause localized states which could trap holes or electrons and act as recombination centers. However one of these two DBs (si#57) causes much more orbital localization than the other one (Si#158). The bond lengths associated with Si#57 are 2.35, 2.37, 2.38, and 2.98 Å (average deviation of 0.175 Å) and the bond

length involved with Si#158 are 2.29, 2.29, 2.55, and 2.63 Å (average deviation of 0.15 Å). Based on the defined cutoff (2.58 Å) and simulated bond lengths, both these atoms have one DB, but the length of the bonds which are assigned as DBs are different (Fig. 4.15a and 4.15b). The length of the DB for Si#158 is shorter than the one for Si#57. Although the assumption is that after a certain bond length cutoff there is no bond between two Si atoms, but as clearly seen, the shorter DB bond length could still result in relatively weak bonds between two Si atoms and consequently leads to less orbital localization. The third DB (Si#9) present in the supercell has bond lengths of 2.34, 2.38, 2.40, and 2.72 Å (average deviation of 0.115 Å) where its average bond length is smaller than the average bond length of Si#57, and is almost the same as the average bond length of Si#158, but with smaller average deviation from the ideal bond length (2.35 Å). This smaller average deviation and shorter average bond length together might be the reason for less contribution from Si#9 in the orbital localization compared to two other dangling bonds. The third strongest peak in the IPR_k graph of a-Si216 supercell is related to a Si atom (Si#166) under bond strain which is illustrated in Fig. 4.10a. As seen before, this Si atom was the most likely on participating in hydrogenation of the a-Si structure.

Figure 4.14b, 4.14c, and 4.14d show the IPR_k values after H addition to the a-Si supercell. In contrast to a-Si, strained bonds create more localization than dangling bonds in a-Si:H. However, regardless of the H position in the supercell, the contribution of all Si atoms in the orbital localization decreases as the H concentration increases in a-Si:H. As shown before, in almost all the most stable configurations of a-Si:H supercells, H atoms were bonded to Si atoms with strained bonds rather DBs, however this interaction still leads to a reduction in the orbital localization caused by the DBs, which are very far from the H position. This observation provides another indication of the global effect of H atoms on the whole amorphous structure. Based on

the number of DBs and IPR_k values of Fig. 4.14, it can be concluded that although the number of DBs of a-Si:H increases compared to a-Si, but the orbital localization actually decreases. Therefore, the number of DBs does not necessarily determine the orbital localization in an amorphous structure.

4.4 Generating the atomic structure of a-Si and a-Si:H containing lower excess energy

So far, we proved that excess energy of an amorphous material plays an important role in determining its electronic properties. This has been not previously considered as a critical property in generating a-Si models. Samples prepared by various experimental methods have excess energy ranging from 0.9 to 0.17 eV/atom [147, 152]. Available a-Si models using MD quenching often correspond to higher excess energy [153–158], suggesting that they might not be representative of the experimental a-Si structure. Therefore, we tried to decrease the excess energy of our modeled a-Si structures by modifying MD simulation. And then we performed the same DFT simulation as before on the supercell with low excess energy to investigate whether our results are affected by the amount of excess energy or not.

The same MD process as before was used in order to generate low strain a-Si supercell from c-Si. However, this time, different cooling rates were applied to obtain more ordered network of atoms. Theoretically, a slower cooling process of a liquid somehow provides enough amount of time to the atoms to find their more stable position in the final solid phase. In order to test this hypothesis, we calculated the excess energy of several supercells obtained from different cooling rates. Figure 4.16 shows the graph of the calculated excess energy vs used cooling time for generating a-Si supercell. As shown, we observe an initial exponential decrease in excess energy as cooling rate decreases, although we do not observe any significant change in excess energy after a certain cooling time. The best obtained excess energy by modifying the

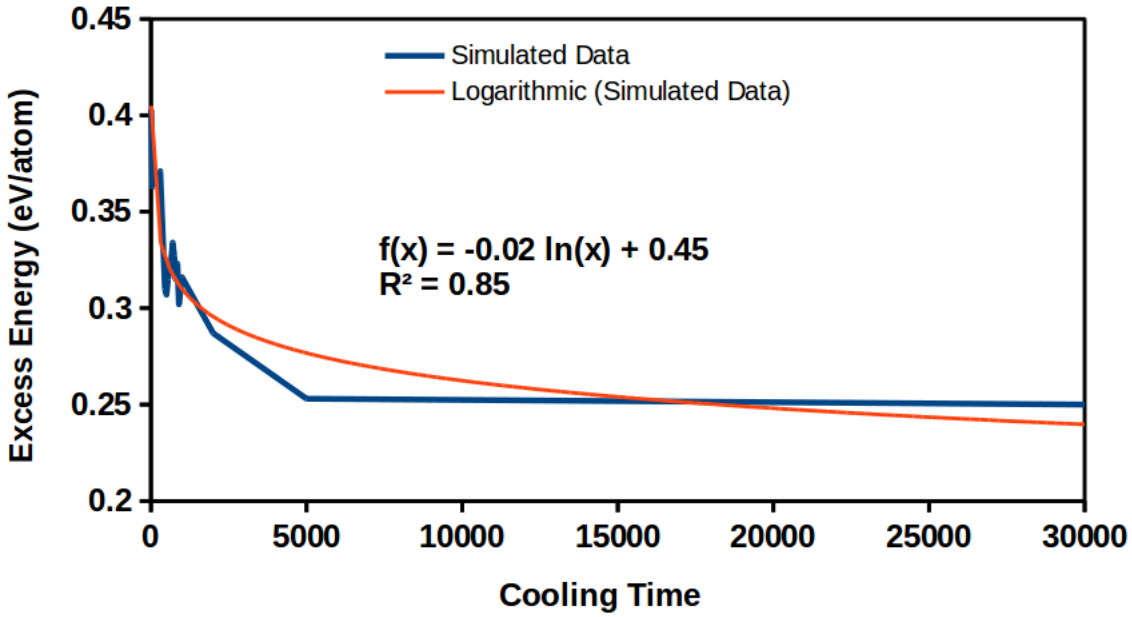

Figure 4.16: The excess energy vs cooling time for the supercells obtained from different cooling rates.

cooling rate is 0.25 eV/atom which is a significant improve compared to our previous supercell (0.36 eV/atom). For further reducing the excess energy of a-Si model, an extra step was added to the normal melting-cooling process which was to increase the temperature from 800 K (at the middle of cooling process) to 1600 K and then quenching to 300K with the same quenching rate as before. This extra step reduced the excess energy from 0.25 to 0.23 eV/atom. For further decrease of the excess energy, we added three Si atoms in their most stable configurations to the supercell, keeping the density of the supercell the same as before. The new supercell has an excess energy of 0.2 eV/atom which is fairly close to the upper end of experimental excess energy range (0.09-0.17 eV/atom). The supercell has four dangling bonds and no floating bonds. The average Si-Si bond length is 2.361 Å with an rms value of 0.0493 Å. The average Si-Si-Si bond angle is 108.47° with an rms value of 11.64° which is very close to the experimental angle distribution of 9-11°. As with the pervious supercells, the validity of the structures of this supercell was checked by calculating

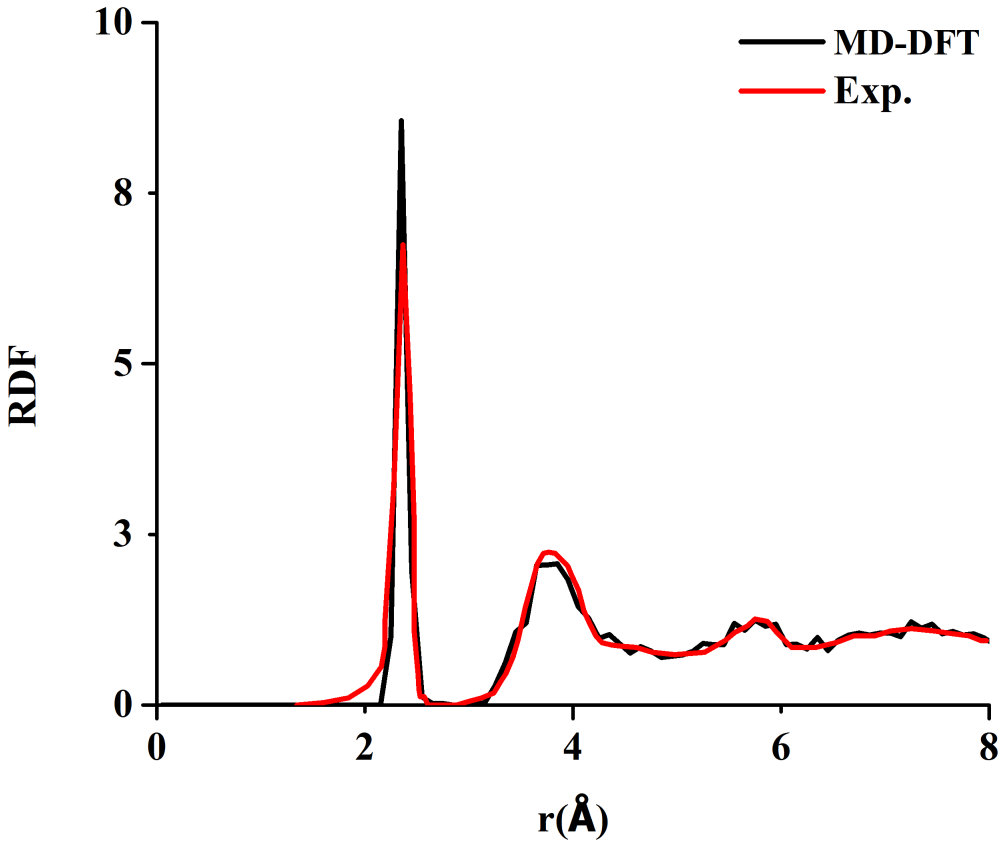

Figure 4.17: The calculated RDF (black lines) of a-Si with low excess energy in comparison with experimental RDF

the Radial Distribution Function (RDF). Figure 4.17 shows the calculated RDF of the a-Si model with low excess energy compared with the experimental results. In comparison with the calculated RDFs (Fig.s 4.2 and 4.9) obtained from our previous supercells, we observe a smoother and more realistic RDF for the case of supercell with lower excess energy.

In order to investigate the effect of H addition on the new supercell, the same method as before was used to add H atoms step by step. Figure 4.18 shows the position of the atoms in the new supercell which were the target of H attack in the most stable configurations. As seen, for five cases, H atoms prefer to add to the atoms bonded by highly strained bonds and only for one case H atom adds to a Si atom

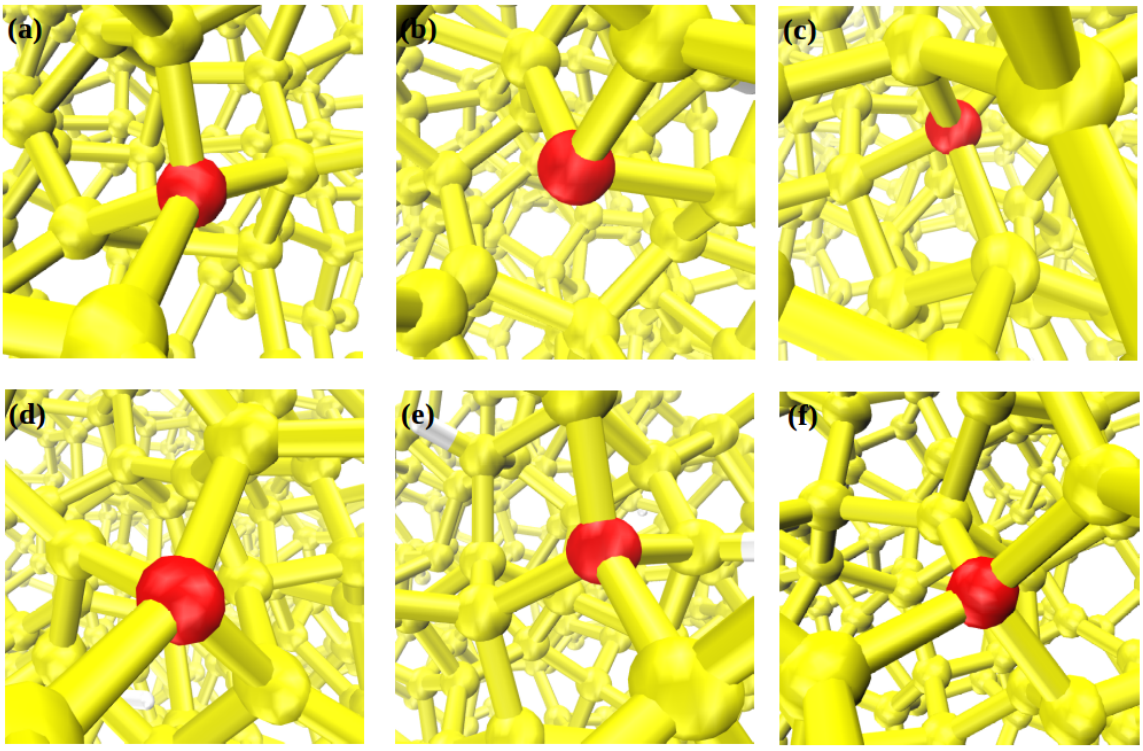

Figure 4.18: The position of Si atoms (red colored) in a-Si structure involved in H addition in a-Si:H with the H atomic percent of a) 0% (a-Si219), b) 0.46% (a-Si219H), c) 0.92% (a-Si219H2), d) 1.37% (a-Si219H3), e) 1.82% (a-Si219H4), and f) 2.26% (a-Si219H5).

with a dangling bond. This result is consistent with our previous results, where we observed that atoms bonded by highly strained bonds (SBs) are most significantly affected by the addition of H, in terms of the lowest energy configuration, with similar if not greater importance to that of dangling bonds in passivating a-Si.

In order to investigate the electronic properties of a-Si and H atom effects, the same electronic structure calculations on a-Si and on the most stable configurations of a-Si:H were performed. Figure 4.19a illustrates the calculated electronic density of states (EDOS) plot of the a-Si and a-Si:H valence band compared to photoemission experimental results, where a good agreement is observed between experimental and computational results in terms of the height and location of the two characteristic

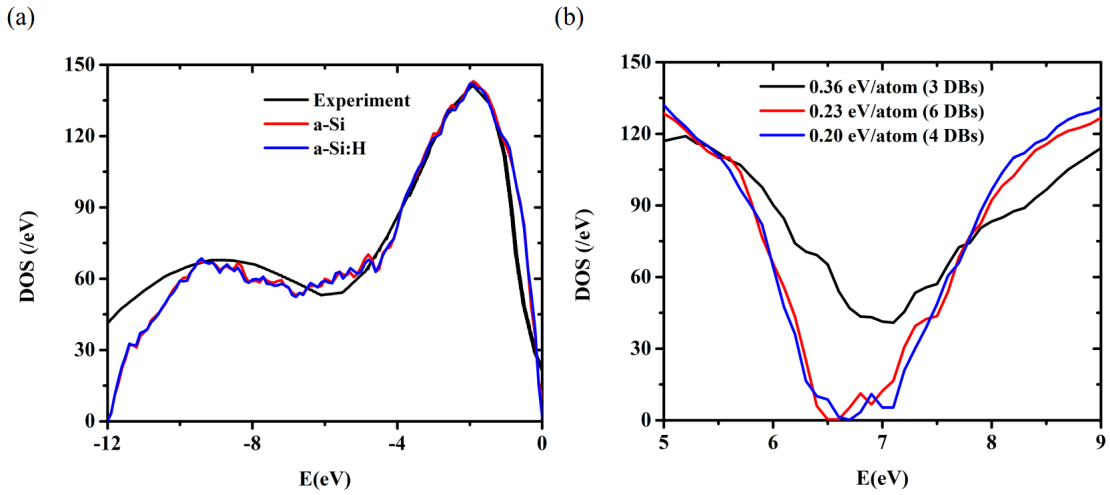

Figure 4.19: Calculated EDOS of a) the valence band of a-Si and a-Si:H in comparison with photoemision experiment and b) a-Si close to the band gap with different strain.

peaks of a-Si and a-Si:H.

From the Fig. 4.19a, its noticeable that the effect of hydrogenation is small on the EDOS of the valence band of a-Si. However, looking in detail at the EDOS close to the valence band edge, it reveals that adding H atoms to the a-Si structure noticeably changes the electronic structure around the band gap. This change mostly includes a decrease in the mid-gap state density, and consequently an increase in the band gap which is in agreement with experimental trends (although the actual Si bandgap is smaller than the experimental value due to well-known issues of normal DFT). The decrease in the mid-gap state density with H has been attributed to the passivation of the dangling bonds, the argument being that the insertion of H into a-Si effectively decreases the number of dangling bonds and consequently removes the mid-gap states in the a-Si EDOS. However, we find the actual picture is more complicated. As mentioned before, the two dangling bonds in all the a-Si:H supercells remains the same after inserting third H, however the density of midgap states in the electronic structure of a-Si:H is zero (Fig. 4.20a). Therefore, we found that

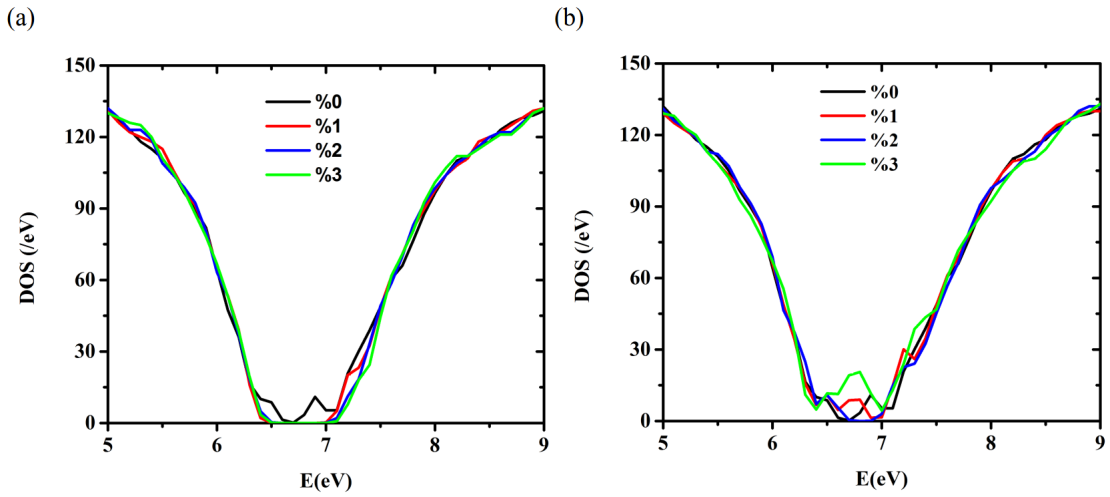

Figure 4.20: Calculated EDOS of a-Si:H close to the band gap for different H concentrations 0% (a-Si216), 1% (a-Si216H2), 2% (a-Si216H4), and 3% (a-Si216H6) in a) least energetic and b) randomly H addition

the number of dangling bonds in the atomic structure of a-Si and a-Si:H does not necessarily determine the density of midgap states in the electronic structure. Here, the observed mid-gap state reduction can be attributed to increasing structural order of the network by better annealing processes or H insertion. Increasing the structural order leads to strain release from the whole a-Si structure and leads to the replacement of weak strained Si-Si bonds (which could be the source of midgap states) by strong Si-Si bonds. Another reason for midgap state reduction can be due to the replacement of relatively weak Si-Si bonds by strong Si-H bonds. The formation of strong Si-H bonds results from the interaction of the the shallow orbital of a-Si in the gap or the valence and conduction band edges with the H orbitals, which instead create deeper electronic states in the valence and conduction bands. To this end, we believe that the change in excess energy stored in the amorphous network relative to the c-Si gives a better description of the a-Si atomic network than the number of dangling bond, as proposed in previous studies.

For further improving our finding in the importance of strain in creating

midgap states, we create two other different supercell using the same mentioned MD simulation but with different condition. Figure 4.19b shows the EDOS of the mentioned supercells with their excess energy. From this figure, we observe that although the number of dangling bonds in the case of less strain structure is more than the number of dangling bonds in the case of the structure with the highest strain, the density of midgap states is significantly less for the less strained structure. The same results in the importance of strains in hydrogenation process were observed, when H atoms were added to the mentioned supercell in the most stable configurations.

In addition to adding H atoms step by step in the most stable configurations, we randomly add H atoms to the a-Si219 supercell. This H addition is mostly equivalent to the kinetic conditions which is applied in an experimental setup for adding H addition in a-Si material, like Plasma Enhanced Chemical Vapor Depositions (PECVD) method. Figure 4.20b shows the EDOS of a-Si:H due to this H addition compared to that of a-Si. As seen from the figure, the random addition of H atoms not only significantly decrease the density of midgap states but also increases the states in some cases. We found that these configurations are less stable than their most stable configurations by 3.16, 3.61, and 8.82 eV for a-Si219H2, a-Si219H4, and a-Si219H6, respectively. The number of DBs in these configurations are 4, 3, and 7 for a-Si219H2, a-Si219H4, and a-Si219H6, respectively. By comparing the mentioned number of DBs in a-Si:H and those of a-Si, we determine again that there is no clear DBs and the density of midgap sates. To this end, by comparing Figure 4.20a and 4.20b, we realize that adding H atoms to a-Si material in more thermodynamic based condition leads to better quality a-Si:H compared to random H addition.

As before, in order to investigate which structural defects are important in the orbital localization, the contribution of each atom in the localization of all the

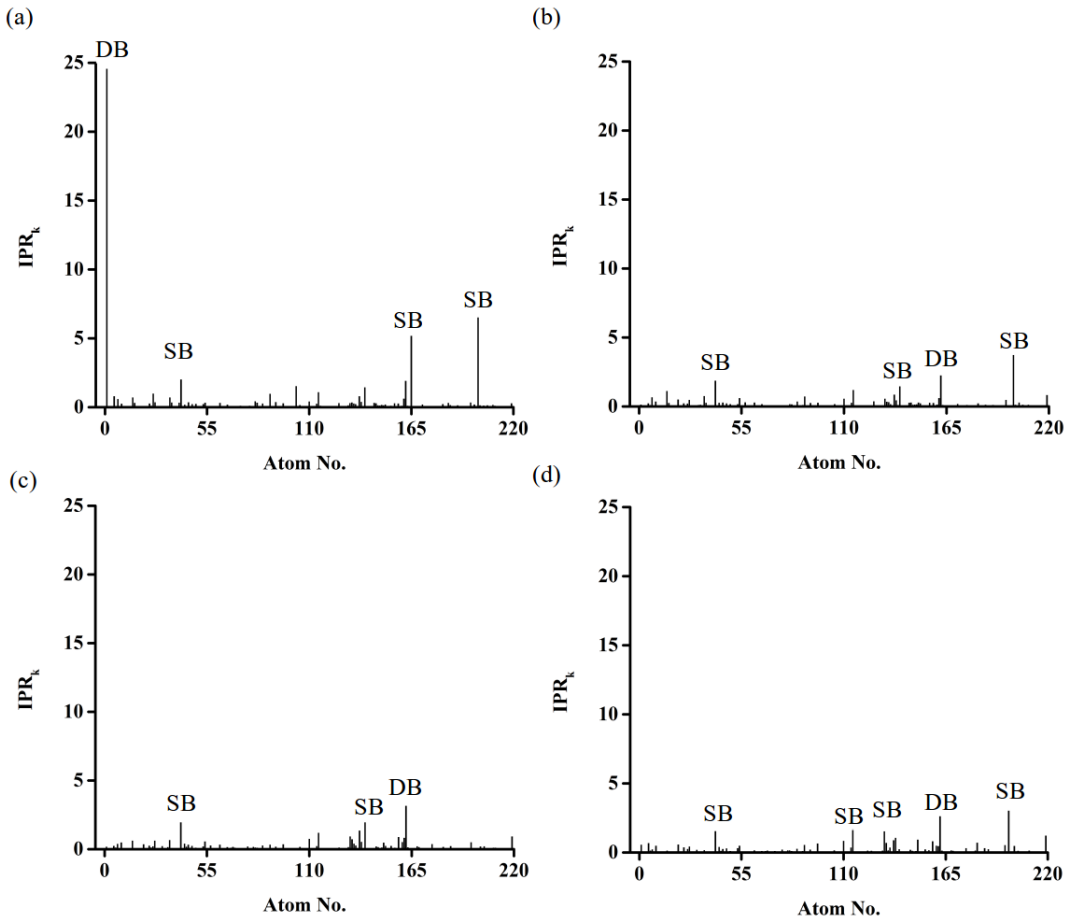

Figure 4.21: The relative contribution of each atom in the orbital localization of the modeled a-Si:H supercell with a) 0% (a-Si219), b) 1% (a-Si219H2), c) 2% (a-Si219H4), d) 3% (a-Si219H6) H atomic concentration.

electronic states in the mobility gap (6.0-8.0 eV) of our new a-Si model was calculated using Eq. 4.4. Figure 4.21 shows the IPRk values for a-Si and a-Si:H with different hydrogen concentrations. As seen, there are several strong peaks in the IPRk graph of a-Si (Fig. 4.21a). Our structural analysis shows that the strongest peak is related to one of the DBs (Si#1) out of three DBs (Si#1, Si#103, and Si#137, Si#162) present in the a-Si219 supercell. This observation is in agreement with the common belief that dangling bonds cause localized states which could trap holes or electrons and act as recombination centers. However, one of these four DBs (Si#1) causes much more

orbital localization than the other ones.

Consistent with the a-Si case, strained bonds still create higher or similar localization compared to dangling bonds in a-Si:H. However, regardless of the H position in the supercell, the contribution of all Si atoms in the orbital localization decreases as the H concentration increases in a-Si:H. As shown before, in almost all the most stable configurations of a-Si:H supercells, H atoms were bonded to Si atoms with strained bonds rather DBs, however this interaction still leads to a reduction in the orbital localization caused by the DBs, which are over long distances from the H position.

Chapter 5

H BONDING CONFIGURATION EFFECT ON THE ELECTRONIC PROPERTIES OF A-SI:H/C-SI HETEROSTRUCTURE

Through the inclusion of a thin layer of a-Si:H on a high quality c-Si substrate, the a-Si:H/c-Si heterojunction solar cells (HIT cells) have achieved the world efficiency record of 26.6% for n-type Si wafers [11], As discussed in Chapter 1. The key to the success of HIT devices is using a a-Si:H layer as a passivating and semiconducting film on top of c-Si [26, 159, 160]. The a-Si:H layer reduces the recombination rate of both photo-generated carriers and the dark current by passiviating defect states at the surface of c-Si, and controls the photo-generated carriers transport by creating a proper band bending (band offset) at the interface. Engineering these two electronic properties (defect states distribution and band bending) is extremely important to future improvement of the efficiency of HIT cells. H incorporation in different conditions during plasma enhanced chemical vapor deposition of a-Si:H offer a unique way to engineer the mentioned electronic properties [29, 161–166]. Due to different fabrication conditions, different H bonding configurations might be generated in a-Si:H layer and at the interface. A better understanding of these H bonding configurations on the electronic structure of a-Si:H/c-Si heterojunctions will aim to improve the device performance. In the current work, we present our first principle study on the electronic properties of a-Si:H/c-Si(001) heterojunction containing different H concentrations with different bonding configurations.

Despite the wide literature concerning the simulation and the study of the amorphous phase, both pure and hydrogenated, either from first principles and by means of semiempirical approaches, we are not aware of many direct simulations of

A full version of this work will be submitted in Physical Review B journal in December 2018.

the a-Si:H/c-Si electronic structure particularly in different H bonding configurations [97, 98, 167]. Tosolini et al. studied the atomic structure of the interface between a-Si:H and c-Si using combined tight-bonding molecular dynamics simulations and first principle calculations. In another work, Nolan et al. have investigated the electronic property changes in a-Si:H and c-Si of a-Si:H/c-Si junction which are perturbed by interface formation on three unreconstructed silicon surfaces, namely (100), (110) and (111). Recently, by combining magnetic resonance measurement and DFT calculations, George et al. studied the origin atomic structure of interface states[32]. In these works in general, the authors mostly focused on the atomic structure and electronic properties of a-Si:H/c-Si heterostructures, while the relation between these properties and the H bonding configurations was not examined in detail.

In this chapter, we present the results of our first principle calculations performed on a-Si:H/c-Si heterostructure models obtained from Si(100) surfaces. These models were initially generated from partially melting and quenching part of the Si on a Si (100) surface using again MD simulation and optimized for different H bonding configurations using DFT methods. The electronic properties of the simulated structures are calculated in order to clarify several questions concerning the sensitivity on H bonding of the interface state density and band bending at the a-Si:H/c-Si. Our results show that the hydrogen amount and configuration play a key role in the electronic properties.

5.1 Method

5.1.1 Generation of the a-Si:H/c-Si structures

For modeling a-Si:H/c-Si heterostructures, we used periodically repeated supercells containing one interface for each phase and therefore two interfaces. We simulated the most common interface, which is that of an a-Si:H thin layer deposited on a (001)

c-Si substrate. To this end, tetragonal 001 supercell containing 256 Si atoms were cleaved from c-Si structure crystallized in diamond form with the experimental lattice constant of 5.43Å(a_0). The dimensions of the supercell are $a = b = 2a_0$ and $c = 8a_0$. We set fixed values for the lateral dimensions a and b and set a variable c/a ratio according to the experimental density of a-Si:H at given H concentrations [145, 168]. Once a reasonable supercell is determined, the melting and quenching process was performed on the 8 upper layers of the supercell within the constant volume, constant temperature ensemble. In practice, we start with a melting simulation at 3000 K for 10 ps using a time step of 0.1 ps. Subsequently, the obtained structure is rapidly quenched close to room temperature (300 K) using a cooling rate of $6 \times 10^{12} K/s$. The chosen cooling rate here is consistent with previous used cooling rates in many Refs. [122, 134, 169] which were between 10^{11} and $10^{15} K/s$. This cooling rate allowed the formation of a disordered a-Si phase interfaced with a crystalline phase after quenching from the melt. After quenching, the a-Si/c-Si interface were annealed for 25 ps at 300 K. Finally, the obtained interface was fully optimized by DFT.

Hydrogenated a-Si structures were obtained by adding H atoms step by step to the amorphous constituent of a-Si/c-Si structure resulting from MD simulations and DFT optimization. In each step, only one H atom was added to the most stable configuration obtained from the previous step. In order to obtain stable configurations at different H concentrations (in each step), we tried all possible configurations of adding a H atom to each Si atom in a-Si phase. The number of Si atoms corresponding to the a-Si phase was 128, and therefore for each H addition, we generated 128 different configurations by bonding H to a given Si atom. After optimizing all the configurations using DFT, the configuration with the lowest energy was considered as the stablest one at that given H concentration, and was used for further calculations.

5.2.1 *Atomic and Electronic Structural Characterization of The Numerical Samples*

Since the atomic structure of a material is a key factor in determining its properties, we first analyzed the atomic structure of our supercells generated by MD and optimized by DFT method. The upper panel of Fig. 5.1 shows the ball-and-stick representation of the atomic structure of the a-Si/c-Si supercell. The supercell contains 256 Si atoms with 128 Si atoms in a-Si phase. After repeating in 3D space, we found ten floating bonds and four dangling bonds (Table. 5.1) per supercell with a cutoff Si-Si bond length of 2.58 Å, which is 10% longer than experimental Si-Si bond length (2.35 Å). The structure mostly displays stable 5, 6 or 7 folded rings and there is no big voids or holes inside. The average Si-Si bond length is 2.37 Å with an rms of 0.04 Åand the average Si-Si-Si bond angle is 107.78 ° with an rms of 12.36 °. As a comparison, the Si-Si bond length is 2.35 Å and Si-Si-Si bond angle is 109.47 ° in the crystalline form of Si. As mentioned earlier, H atoms were gradually added to a-Si/c-Si supercell in different bonding configuration to obtain a-Si:H/c-Si supercells. Table. 5.1 illustrates the number of dangling bonds (DBs) and floating bonds (FBs) per supercell in the most stable configuration of a-Si:H/c-Si heterostructures in different atomic percent of H concentration. As is clearly seen, the number of DBs and FBs per supercell reduces as the H concentration increases. This observation is consistent with the common belief that H incorporation in the fabrication of a-Si results in passivating DBs and FBs. Interestingly, the number of FBs decreases more rapidly than that of DBs by adding H atoms to the supercells, revealing that FBs cause more instability compared to DBs. All DBs and FBs in the a-Si:H/c-Si heterostructure disappear when the concentration of H reaches 6.25% in the supercell. Here we focus on DFT results obtained from the structure with a H concentration of 6.25%.

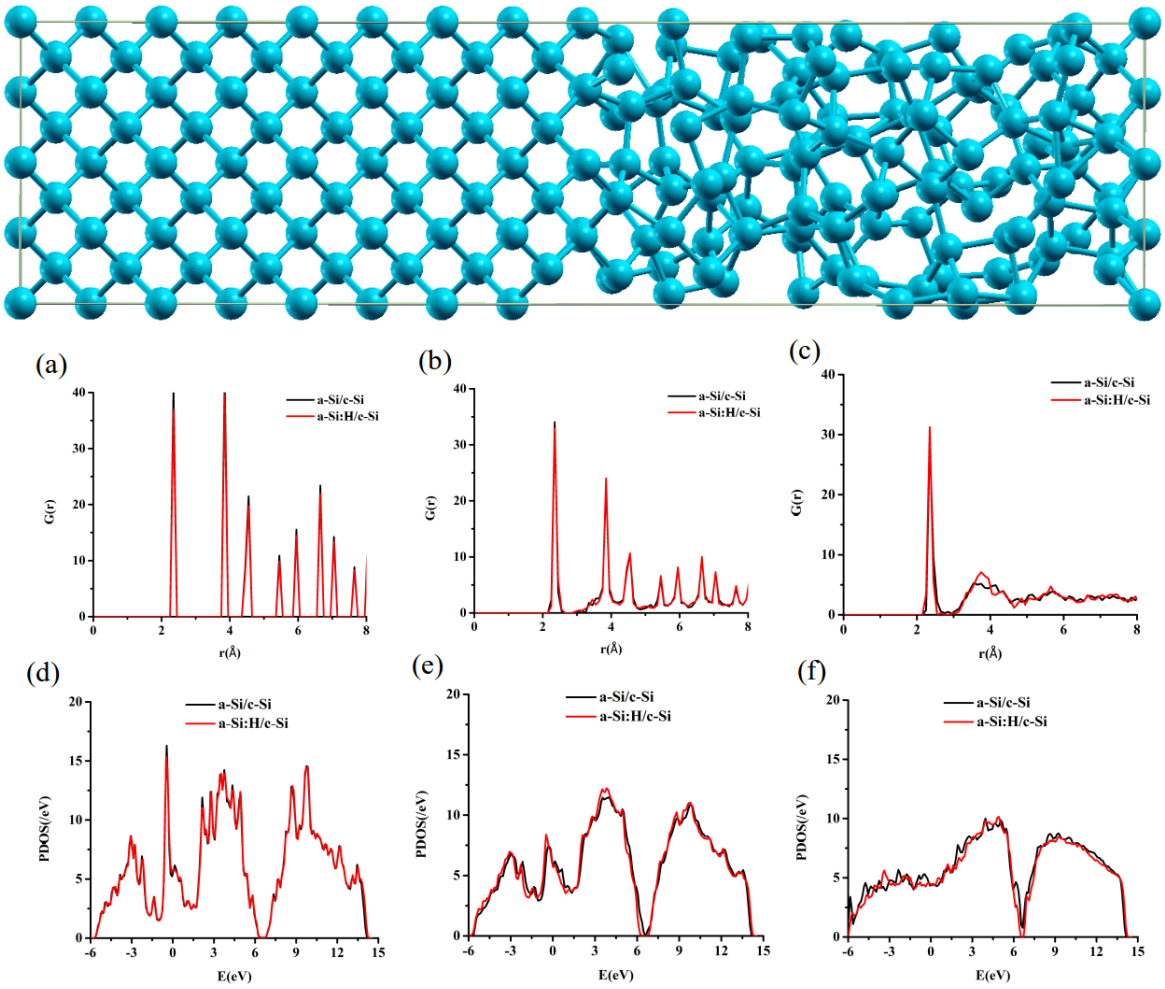

Figure 5.1: The atomic structure of modeled a-Si/c-Si supercell. The layer resolved RDF of a) c-Si, b) interface and c) a-Si. The projected Density of States (PDOS) plot of d) c-Si, e) interface and f) a-Si of a-Si/c-Si in comparison with those of a-Si:H/c-Si.

Table 5.1: The number of dangling bonds (DB) and floating bond (FB) in a-Si:H/c-Si heterostructure per supercell in different atomic percent of H concentration (at%).

at%	**DB**	**FB**
0	4	10
0.78	4	5
1.56	4	2
2.34	3	2
3.12	2	2
3.91	3	0
4.69	2	0
5.47	0	1
6.25	0	0

In order to check the validity of our atomic structure, we compute the region resolved Si-Si RDF of the heterostructure along the growth direction z. Here, a region is defined as a specific region of the supercell with the dimension of $a = b = c = a_0$. The RDF is a criterion to determine the order of particles' position in a system. Since RDF is experimentally accessible to measure, it provides a strong tool for checking the validity of computationally created structures.

The middle panel of the Fig. 5.1 displays the computed region resolved Si-Si RDF obtained from the modeled supercells. We expect to observe sharp peaks at the RDF for crystalline materials due to periodic atomic structure, while broadened and coalesced peaks appear in amorphous materials due to the presence of weak short range order and the lack of long range order. As discussed in Chapter 3, consistent with this argument, we obtained very sharp peaks in the RDF of the crystalline region, and broadened peaks for the RDF of the amorphous region (Fig. 5.1). Although the amplitude of the RDF peaks does not give quantitative information because of the statistical noise due to the limited size of the supercell, the RDF peak location can provide valid information for comparison purposes. As seen, the peak locations in the computed RDFs are consistent with the peak locations in the measured RDFs

for both the case of bulk crystalline and amorphous Si [6, 7]. In addition, the RDF at the interface gives us a visual indication of the transition between amorphous and crystalline regions. The region resolved RDFs obtained from a-Si:H/c-Si are similar to ones from a-Si/c-Si with this being difference that in the presence of hydrogen atoms, the atomic order of the amorphous layer and the interface region are improved. This atomic order enhancement is particularly clear in the second RDF peak of a-Si:H in comparison with that of a-Si.

As a result of the atomic structure differences, c-Si and a-Si or a-Si:H have different electronic structure. The c-Si electronic structure contains three characteristic peaks in the valance band and a clear energy gap between valence band and conduction band, with no midgap states in the energy gap. In contrast to c-Si, the a-Si or a-Si:H electronic structure contains two characteristic peaks in the valance band, the well known tail states, and midgap states in the forbidden gap of its crystalline counterpart. These band tail states and midgap states are highly sensitive to incorporation of hydrogen in the fabrication of a-Si. The aforementioned electronic properties are related to c-Si and a-Si(a-Si:H) in the bulk phase, but here we compared them with the computed projected density of states (PDOS) in the crystalline and amorphous region of the modeled supercell in order to furtuer verify the reliability of the generated structures. The PDOSs were computed in a middle section of the c-Si and a-Si or a-Si:H supercell, at the maximum distance from the interfaces. The lower panel of Fig. 5.1 shows the computed PDOSs. For the c-Si region, the PDOS shows the three characteristic peaks of c-Si bulk and a clear separation between the valence and conduction bands. On the other hand, the PDOS of a-Si or a-Si:H shows a deviation from the c-Si PDOS by converting three to two characteristic peaks and by the appearance of valence and conduction band tails as well as midgap states due to the presence of undercoordinated Si and strained Si-Si bonds [118]. As seen, the PDOS in

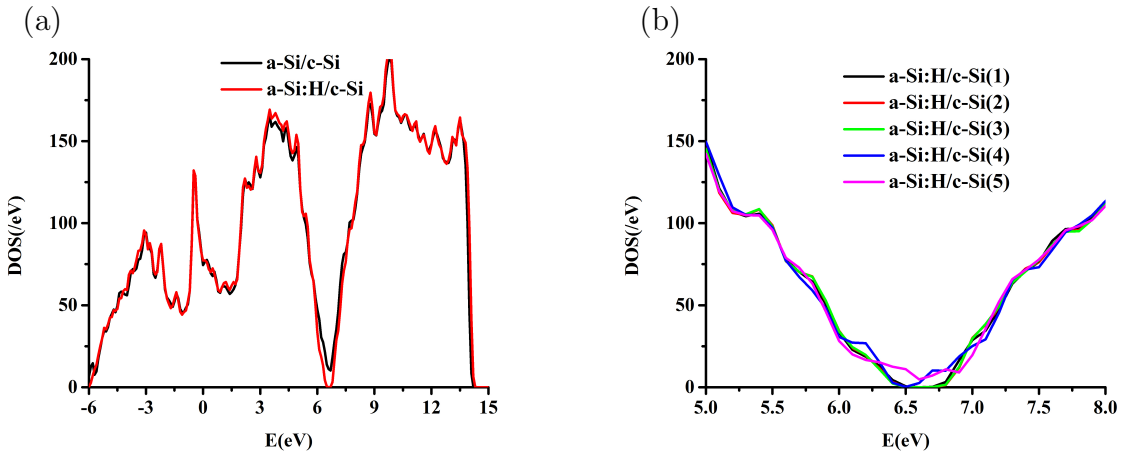

Figure 5.2: a) The total EDOS of a-Si:H/c-Si in comparison with a-Si/c-Si b) the EDOS of a-Si:H/c-Si with different H bonding configuration close to the band gap.

the c-Si regions has the typical form of bulk c-Si and the PDOS in the a-Si regions is typical of bulk a-Si. On the other hand, our computed PDOS in the interface region contains a combination of electronic properties of c-Si and a-Si(a-Si:H). While the conduction band of interface PDOS shows three characteristic peaks coming from the c-Si part, the peaks are broadened and somehow collapsed due to the presence of the a-Si part. The band gap of the interface PDOS contains some midgap states, but not as much as the PDOS of a-Si or a-Si:H.

After confirming the reliability of our structures, we now focus on the total EDOS of a-Si/c-Si and a-Si:H/c-Si. The left panel of Fig. 5.2 shows the total EDOS diagram of a-Si/c-Si in comparison with that of a-Si:H/c-Si in its most stable configuration, for a H concentration of 6.25%. At first glance, it is obvious that H atoms in their most stable bonding configurations decrease the density of midgap and tail states. Our structure analyzis indicates that this decrease is not only due to H bonding to Si atoms with dangling bonds, but also due to H bonding to Si atoms under high bond length or angle strain. This finding is not unexpected, since Si-Si strained bonds are not only by themselves one of the main source of midgap and band tail

states [118], but also the main source of DBs and FBs due to causing high disorder in the a-Si network. Consistent with this argument, we find that in some cases, H atom addition to the Si-Si strained bonds results in removing DBs and FBs which are considerably far away from the added H location. Interestingly, as seen from Fig. 5.2a, H atoms tend to mostly remove the midgap states rather than the band tail states. This observation indicates that midgap states cause more instability than tail states. By looking in more detail at the EDOS diagrams of a-Si:H/c-Si, one can figure out that the reduction in midgap states due to H passivation is associated with an increase in the density of states at the band edges or into the main valence and conduction band as the consequence of the conservation theorem for the number of eigenstates [170]. Despite all these changes in the electronic structure of a-Si/c-Si due to H addition, the general form of the electronic structure is persevered which confirms we used a low enough H concentration for generating the a-Si:H/c-Si. To this end, neither the exchange-correlation functional or the size of supercell here are sufficient to precisely determine the density and position of the midgap and tail states, but our calculations still offer a good model to predict and analyzis the basic change of the electronic structure due to H addition, which could be comparable with experimental results.

In order to investigate how the H bonding configuration affects the electronic structure, we also examined the electronic structure of the four next most stable configurations of a-Si:H/c-Si heterostructure for a H concentration of 6.25% (8 H atoms in the amorphous region of our supercell). Since we observed small changes in the EDOS plot outside the band gap of the a-Si:H/c-Si supercell, for these configurations we only present EDOS close to the normal band gap. Figure 5.2 shows the EDOS plot close to the band gap of the most stable configuration in comparison with that of the four next stable configurations. As shown, the density of midgap and band tail states are highly sensitive to the H bonding configuration. In comparison to the

three most stable configurations, the H atom creates midgap and tail states in the forth and fifth most stable configurations. Our structure analyzis show that these two configurations, in contrast to the most stable one, contain DBs and FBs (one DB and one FB for forth stable configuration and two FBs for fifth stable configuration). Therefore, H atoms may be the source of DBs and FBs in less stable configurations.

5.2.2 Density of defect states and orbital localization in a-Si:H/c-Si heterojunction

There is no doubt that defect states in semiconductors are one of the most critical physical issues strongly affecting the efficiency of optoelectronic devices including solar cells. These states play a key role in carrier recombination, carrier trapping, and carrier transport [171–175, 175–179]. Since the atomic structure dramatically changes along the growth direction of a-Si:H/c-Si interfaces, it is expected that the density of defect states and the localization of electronic states also change along that direction. In this section, we investigate how the density of defect states and the orbital localization changes as the phase gradually changes from crystalline Si to amorphous, and as H atoms are injected to the system.

In several first principle studies, the density of defect states has been calculated by projecting the density of midgap states along simulated supercells [180–182]. Here, we use the same approach in order to calculate the density of defect states. The band-gap region is calculated by performing DFT calculations on a c-Si supercell with the same size of the modeled a-Si/c-Si supercell. The band gap region extends from 6.2 eV to 7 eV. Figure 5.3 indicates the projected density of states in this band gap range along the z direction of the a-Si/c-Si supercell in comparison with that of a-Si:H/c-Si supercell with different H bonding configurations. it is notable that regardless of the H bonding configuration, the local density of defect states decreases as H is inserted into the a-Si/c-Si heterostructure. As expected, the density is zero in the crystalline

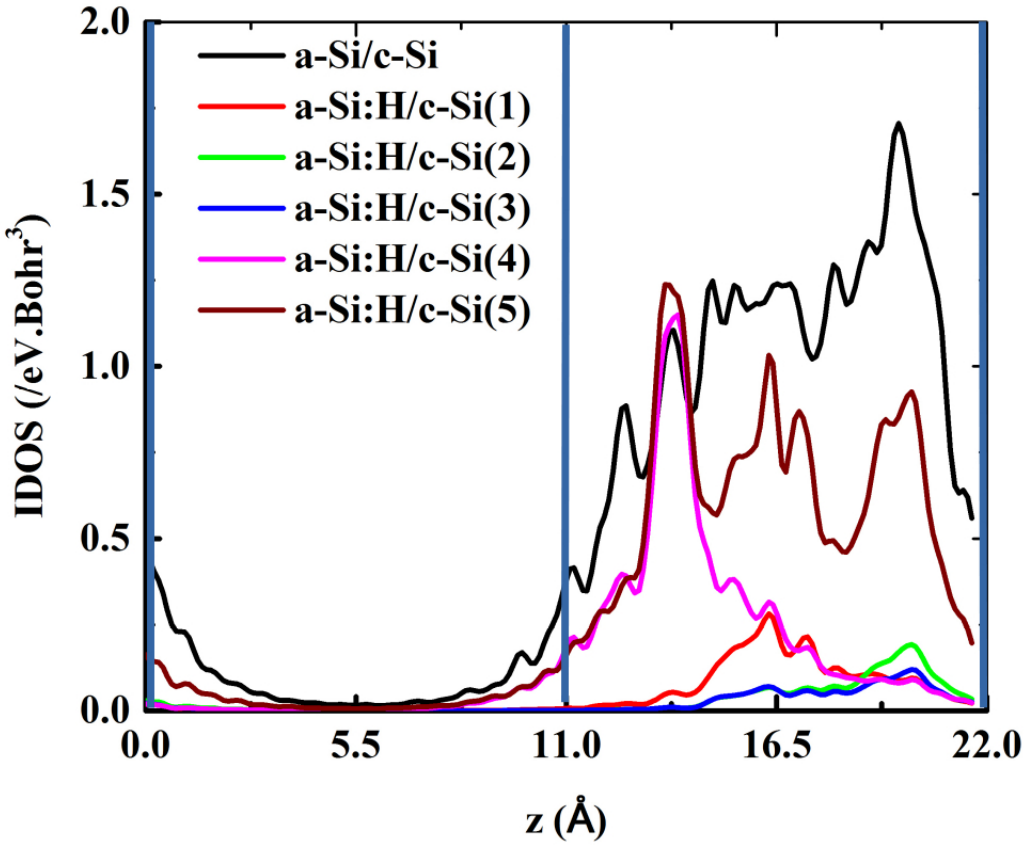

Figure 5.3: The local density of defect states for a-Si/c-Si in comparison with a-Si:H/c-Si with different H bonding configuration. a-Si:H/c-Si(n) is standing for nth stable configuration of a-Si:H/c-Si supercell with 6.25% H atomic concentration. The vertical blue lines shows the location of the interfaces.

part of heterojunction and unexpectedly, continues to be zero at the interface for the most stable configurations and reaches its maximum in the middle of a-Si:H layer. This finding is in contrast to the common picture for the case of crystalline heterojunctions between dissimilar materials that the maximum defect state density exists at the interface. In the case of a heterojunction between a crystalline and an amorphous form of the same material, the low defect state density at the interface shows that a-Si:H layer, in its most stable configuration, is an effective passivation layer on the top of the c-Si substrate with low interface density, at the interface,

reaching a maximum defect state density in the middle of a-Si:H layer, which agree with the observation that most efficiency drop in HIT cells is due to parasitic loss, consistent with experimental reports [28]. Since interface states negatively impact the open circuit voltage in solar cells, the low interface state density here explains the high open circuit voltage in HIT cells. Interestingly, we find that the low density of defect states at the interface is not due to H bonding to the interface atoms. In most of the cases, we observe that H atoms preferably bond to atoms in the middle of a-Si layer, probably due to high density of defect states at the middle of a-Si layer in a-Si/c-Si heterojunction, which cause a defect state density reduction not only in the a-Si layer but also at the interface. This result shows that H atoms do not only have local impact in an amorphous network, they can cause nonlocal changes in the structure. We observe that in the most stable configurations, the local density of defect states are lower than that in the less stable configurations. This finding shows that the annealing process in the presence of H atoms can positively impact the quality of a-Si:H/c-Si heterojunction if H can find its most stable configuration, in consistent with recent experimental results [183].

it is obvious that the computed density of defect states depends on the defined band gap. Instead of considering the band gap of c-Si constituent of c-Si/a-Si:H heterostructure, we can use the band gap region of a-Si:H constituent for computing density of defect states. The band gap of an amorphous material is defined as the energy difference between the mobility edge of the valence band and that of the conduction band. Due to the localized nature of band-tail states from structural defects, the mobility of electrons and holes at these states is much lower as compared to the nonlocalized states in the valence and conduction band, where the carriers are considered free. The energy separation of localized and nonlocalized states is rather sharp and, consequently, this dividing energy has been termed mobility edge

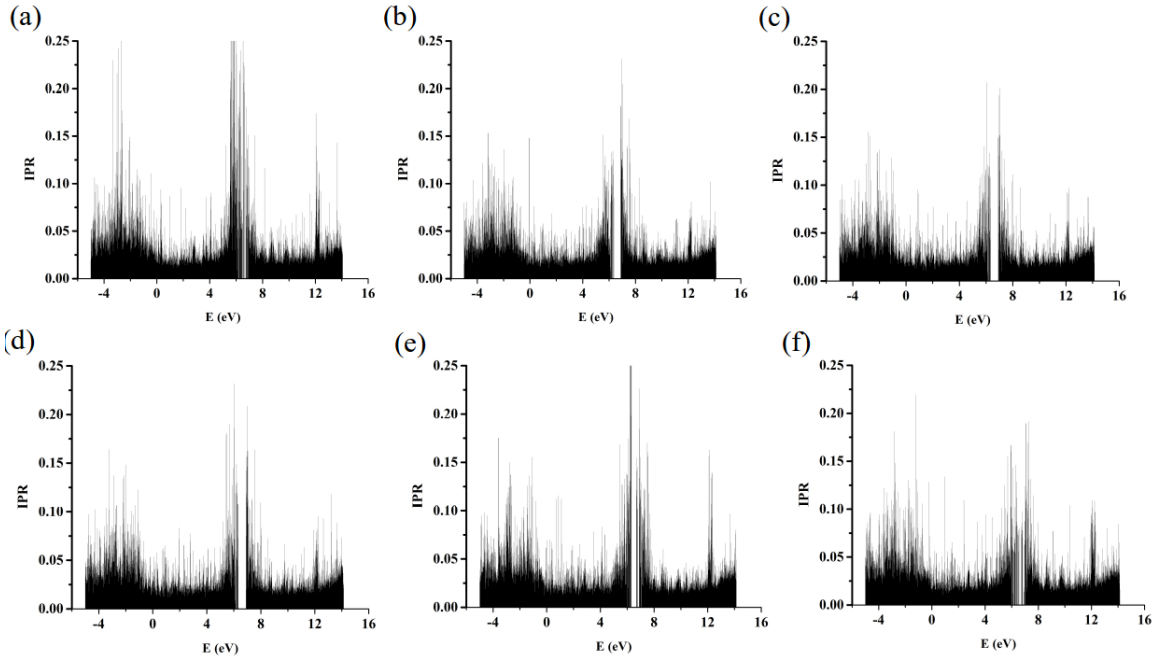

Figure 5.4: a) The IPR of the electronic states of a-Si/c-Si supercell. The IPR of the electronic states of a-Si:H/c-Si supercell in b)first c)second d)third e)forth and f)fifth stable configuration.

[109]. As the energy separation of localized and nonlocalized states is sharp, electronic transport in a-Si:H is dominated by the carriers in the states just below the valence-band mobility edge and just above the conduction-band mobility edge; hence for electronic transport, the mobility gap is the amorphous equivalent of the band gap.

The localization of the Kohn-Sham orbitals was studied in detail for computer generated a-Si:H/c-Si structures considered here using a quantity named inverse participation ratio (IPR), defined earlier in Chapter 4. Figure 5.4 plots the calculated IPR of all the Kohn-Sham orbitals obtained via DFT versus their energy for a-Si/c-Si and a-Si:H/c-Si in its first five stable configurations. it is very obvious from the figure that regardless of the H bonding configuration, H addition decreases strongly the localization of electronic states in the a-Si:H/c-Si heterostructure. According to the Anderson model, this localization decrease is due to the decrease in disorder of

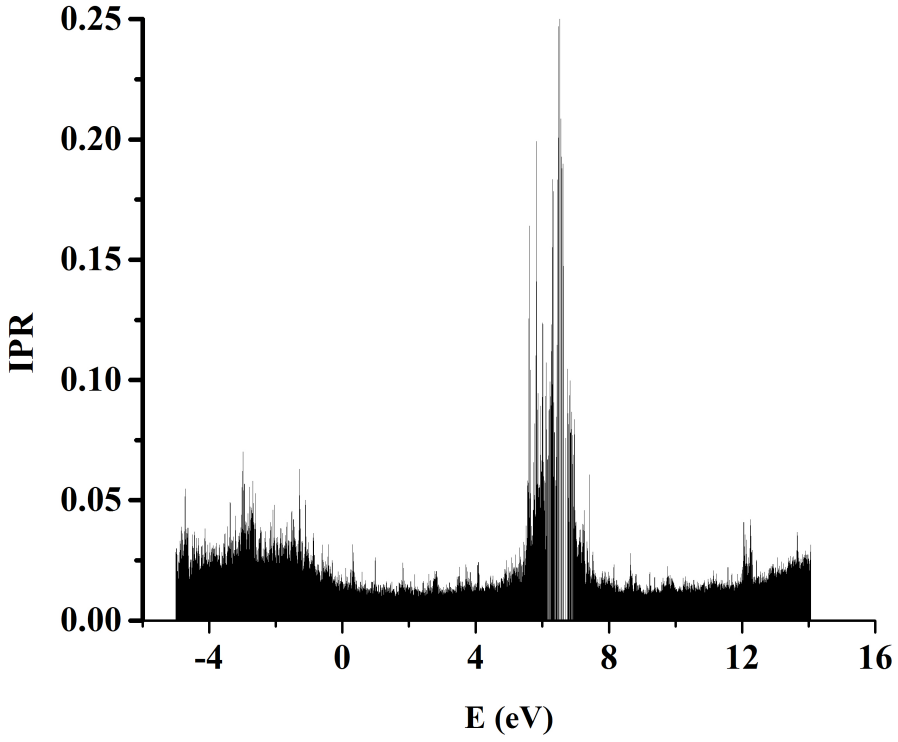

Figure 5.5: The average IPR of the electronic states of a-Si/c-Si supercell.

the atomic structure. With a comparison between the IPR plots of different configurations of a-Si:H/c-Si heterostructures, it reveals that the localization of orbitals slowly increases as the energy of the configuration increases. This observation can be attributed to the increase of disorder as the energy of the configuration increases. it is worth to noting that the localization of orbitals in the valance band is lower than that in the conduction band for the most stable configuration of a-Si:H/c-Si. Whereas, the localization of conduction band orbitals becomes higher compared to valence band orbitals as the energy of the configuration increases. If this localization is a dominant factor, aside from the valance and conduction band offsets in determining carriers flow, it shows that a-Si:H/c-Si could behave more as a hole selective

in the more stable configurations and as an electron selective layer in the less stable configurations.

We assign a mobility edge to the valence and conduction band where a sharp transition between localized and nonlocalized states occurs. As seen in Fig. 5.4, due to the noisy nature of the IPR, this transition is not clear; therefore we use a moving average filter to remove the noise. As an example, Fig. 5.5 shows the localization plot after averaging for a-Si/c-Si. We define a transition as a sharp transition when $dIPR/dE$ is more than 100 /eV. Based on our definition, we find a mobility gap of 5.8-7.3, 5.7-7.2, 5.8-7.5, 5.5-7.3, 5.5-7.5, and 5.9-7.5 eV for a-Si/c-Si, a-Si:H(1), a-Si:H/c-Si(2), a-Si:H/c-Si(3), a-Si:H/c-Si(4), a-Si:H/c-Si(5), respectively. Therefore, the value of the bandgap are 1.5 and 1.7 eV for a-Si/c-Si and a-Si:H/c-Si (on average), respectively. These bandgap value are in close agreement with experimental bangap measured from a-Si and a-Si:H materials. it is worth to notify that except for the last configuration, the value of the mobility gap of a-Si:H/c-Si increases as the energy of the configuration increases.

Based on the obtained mobility gaps, we compute the density of localized defect states by projecting the density of states within the mobility gap along the z direction of our supercells. We only projected the electronic states which were located in a-Si or the interface part of our supercells. Figure 5.6 shows the density of localized-defect states obtained from the aforementioned approach. Figure 5.3 also shows that the density of localized-defect of a-Si/c-Si is higher than that of a-Si:H/c-Si in all configurations. Except for the last configuration, the density of localized-defect states increases as the energy of configuration increases. The failure in the general trend for last configuration might be due to wrongly estimating its mobility gap.

By analyzing the Kohn-sham orbitals of localized states, we find that most

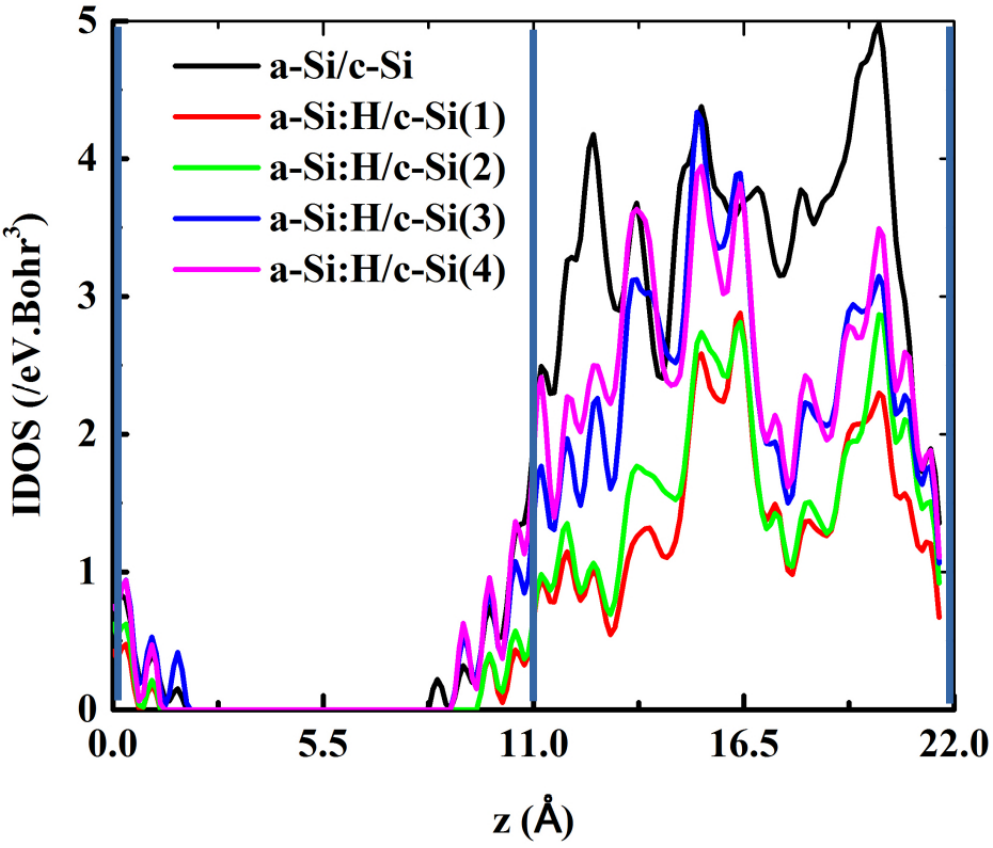

Figure 5.6: The local density of localized-defect states obtained from mobility edges for a-Si/c-Si in comparison with a-Si:H/c-Si with different H bonding configuration. a-Si:H/c-Si(n) is standing for nth stable configuration of a-Si:H/c-Si supercell with 6.25% H atomic concentration. The blue vertical lines are showing the location of the interfaces.

of defect-induced energy levels in the mobility gap of both a-Si/c-Si and a-Si:H/c-Si heterostructures are because of the atomic p-states of Si atoms. it is well known that the strong spacial localization of the structural point defects creates atom-like states with sharply peaked eigenstates. The strong degree of localization combined with sharply peaked in-gap states could potentially cause the absorption or emission of single photons from those defect. For all types of defects we found that the electronic states that are induced by the defects are strongly localized on atoms forming the defect and on the shell of atoms surrounding the defect, and do not significantly reach

out much further in space. In the electronic energy spectrum the defect states occur as deep levels in the bulk band gap, as shallow levels very close to the band edges, and as well as in-between bulk states.

As a result of this section, no matter how H atoms bind to the Si atoms, they may still reduce the density of localized-defect states in the a-Si/c-Si heterostructure. Moreover, by comparing configurations with different stability, we find that this density of localized defect states may be strongly affected by the local H bonding configuration.

5.2.3 Band Bending of a-Si:H/c-Si Heterostructure

Recently, there has also been an increasing interest in understanding the inversion phenomenon at the amorphous (a-Si) and crystalline (c-Si) interface in a HIT cell. The band diagram of a HIT cell based on a-Si:H/(n)c-Si heterostructure shows a relative large band bending ($e\phi$) at the interface such that the interface region is strongly inverted. This inversion can significantly affect the exchange of electrons or holes between the conduction or valence bands at the interface and consequently affect charge carrier transport. Since experimentally there is no simple method to distinguish the inverted carrier-induced signal from that of the majority-carrier defect states, investigating the band bending besides the density of defect states is theoretically important. Therefore, in this section, we focus on the band-bending of a-Si/c-Si heterostructure and H insertion on it in different configuration.

The determination of band bending between two materials can be performed through band diagram calculations. On the other hand the band diagram calculations can be obtained using either the projected local density of states calculation (PDOS) or the potential line-up method. Although both methods are capable of providing insight on how the alignment between two materials should be, we only

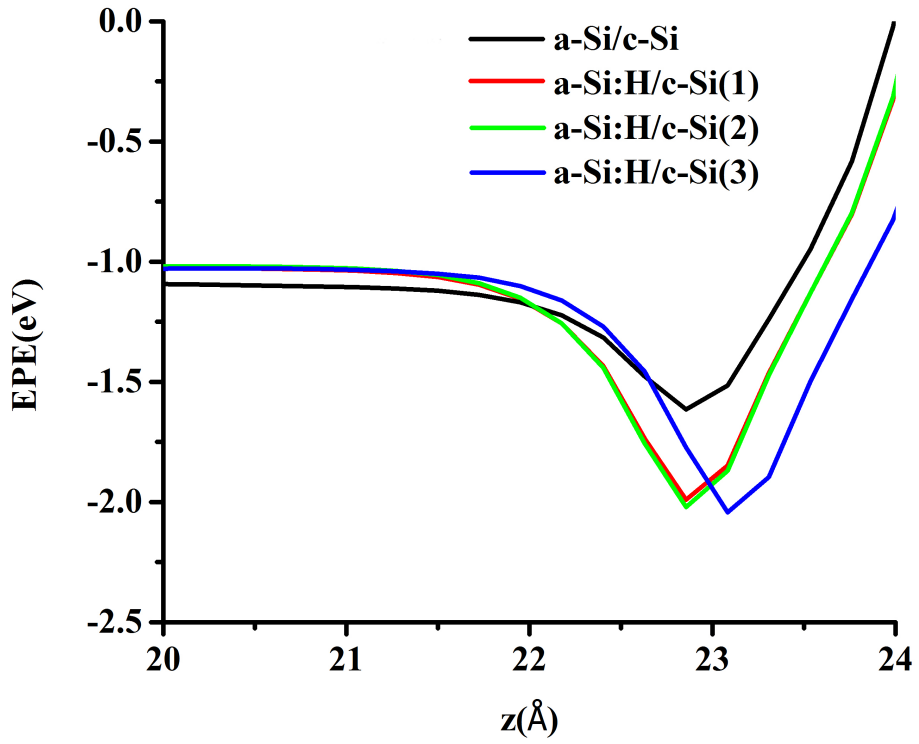

Figure 5.7: a) The IPR of the electronic states of a-Si/c-Si supercell. The IPR of the electronic states of a-Si:H/c-Si supercell in a)first b)second c)third d)forth and e)fifth stable configuration.

used the potential line-up method in this work for calculating the band alignment of the a-Si:H/c-Si heterojunction, since the PDOS calculation requires higher demand of convergence parameters, especially for complicated systems [184]. Here we only focus on the valence band alignment since DFT is more accurate for the valence band calculation rather than the conduction band which represents excited states. Figure 5.7 shows the macroscopic average of the electrostatic potential along the z direction of a-Si/c-Si in comparison with that of a-Si:H/c-Si for different H bonding configurations. We did not include the band diagram of the fourth and fifth most stable configurations of the a-Si:H/c-Si heterostructure in Fig. 5.7, since the electrostatic

potential energy (EPE) is linearly changing through the c-Si phase for those configuration. As seen from the figure, the general form of the macroscopic average EPE plot is the same for a-Si/c-Si and all the configurations of a-Si:H/c-Si. it is obvious that regardless of the H bonding configuration, the band bending of a-Si/c-Si heterostructure increases when H is inserted. Based on these graphs, we computed the value of the band bending as 0.963, 1.000, and 1.014 eV for the first, second, and third most stable configurations, respectively. Therefore, the band bending value changes a few tens of meV when the H bonding configuration changes. This change in band bending value is in close agreement with experimental results [29].

Chapter 6

ELECTRONIC STRUCTURE OF GAP/SI HETEROJUNCTION AND THE ROLE OF HYDROGEN PASSIVATION

The integration of GaP with Si solar cells provides a route to increased efficiency by serving as a buffer for the integration of III-V solar cells [185–187] or as a component of a carrier selective contact [188]. For example, GaP has served as the buffer layer in III-V solar cells for Si-based tandems which use direct heteroepitaxial growth of III-V films on Si substrates [189, 190]. In addition, selective carrier approaches with GaP can allow high efficiency by reducing the absorption in comparison with amorphous Si (a-Si) and ITO layers [191, 192]. Moreover, the use of GaP as a selective contact in replacing a-Si allows selective contact structures to be applied to Si-based tandems.

To achieve high efficiency, the GaP/Si interface should have low recombination and minimize the introduction of defects. Ideally, a lattice-matched heterojunction is desirable in order to avoid defect formation at the interface due to strain, and GaP is an attractive candidate [193–195] for III-V/Si-based device technology since it is nearly lattice matched (99.96%) to Si. For nearly lattice-matched heterojunctions, structural mismatch contributions in the electronic structure such as strain and dislocation formation should be negligible [196]. However, the electronic mismatch due to the heterovalent nature of the GaP/Si interface is a fundamental issue. The atomic bonds between electronically dissimilar materials with an excess or deficiency of electrons strongly affects the quality of the electronic properties of the interface.

Electronic mismatch at the GaP/Si interface takes place due to its heterovalent nature, and can be explained in the framework of the electron counting model (ECM) [13]. In particular, for GaP/Si(001), there are two different heterovalent bonds, Si-Ga

A full version of this work has been submitted in Progress in Photovoltaic journal in Jun 2018.

or Si-P, which have 1+3/4 or 1+5/4 electrons, respectively. Since a covalent bond consists of two shared electrons, every heterovalent Si-Ga or Si-P bond accepts 1/4 or donates 1/4 of an electron. The result of this excess or deficiency of electrons, in contrast to an isovalent interface, is a charge accumulation in the near-interface region, and a strong electric field at an abrupt heterovalent interface [197**?**] consisting of only Si-Ga bonds for the Ga-polar interface or only Si-P bonds for the P-polar interface in the (001) orientation. Charge-neutral (compensated) interfaces have been suggested for intermixed interfacial layers where the number of Si-Ga and Si-P becomes equal at the interface [198]. In addition to charge neutrality benefits, it has also shown that the intermixed interfacial layers are energetically more favorable than their abrupt interface counterparts [199, 200].

The electron excess or deficiency at the polar interfaces of GaP/Si(001) could cause interface states in the forbidden gap of the electronic structure [200] These interface states have been theoretically predicted in the fundamental band gap for other polar-nonpolar heterojunctions such as GaAs/Si [201], GaAs/Ge [202], and ZnSe/Ge [203] and have been experimentally investigated for GaAs/ZnSe [204] and ZnSe/Ge [205]. In particular, interface states were found even in compensated heterovalent interfaces [200, 206] These interface states can impede charge transport through the interface and reduce the carrier lifetime, hence detrimentally affecting device functionality [65, 198, 207–209]. The passivation of interface states has always been an important consideration for realizing high performance heterojunctions [210–217]. Despite the importance of interface states in device functionality, to the best of our knowledge, the density and distribution of interface states in the electronic structure of the GaP/Si(001) heterojunction has not been thoroughly investigated.

In the present chapter, the atomic and electronic band structure of the GaP/Si(001)

heterojunction are investigated using first principles calculations. In particular, we focus on the density of defect states and charge at the interface for different interface configurations. Since it is well known that hydrogen (H) plays an essential role in the passivation of undesirable surface and interface states [109, 218–222], we investigate the effect of H addition to the heterojunction on the electronic structure and interface state density distribution within the band gap for abrupt interfaces, and compare the results with different types of intermixed interfaces.

In the following section we provide the technical details concerning the generation of the atomistic structure of GaP/Si heterojunctions with and without H atoms, with the use of a periodically repeated supercell approach. In the next section, we discuss the results of the interaction of H atoms with the atomic structure of GaP/Si heterojunction, where we present ab initio results for the electronic structure calculations, and we compare the densities of states (DOS), integrated densities of states (IDOS), electrostatic potential energy and charge density obtained for GaP/Si with and without H atoms, and considering different configurations of interface mixing. The last section then summarizes the results and presents the conclusions of this study.

6.1 Methods

We performed both structural optimization and electronic structure calculations at the density functional level of theory (DFT) implemented in the Quantum Espresso 5.2.1 software package [223]. The exchange and correlation energies were estimated by the Perdew-Burke-Ernzerhof (PBE) [105, 146] generalized gradient approximation as used in previous work on GaP/Si interfaces [200, 224]. The Broyden-Fletcher-Goldfarb-Shanno (BFGS) quasi-Newton algorithm, based on the trust radius procedure, was used to obtain optimized structures. The atomic structure of the supercells

was taken as optimized when the interatomic forces become smaller than 10^2 eV/Å. The core and valence electron interactions were described by a Norm-Conserving Pseudopotential function. Unless otherwise stated, an energy cutoff of 160 eV was employed for the plane-wave basis set, and a 16164 k-point mesh was used with the Monkhorst-Pack grid method for the Brillouin-zone sampling in all the calculations. A Gaussian fixed method was applied to determine the band occupations and electronic density of states.

In order to model the atomic structure of GaP/Si, we chose a supercell containing 16 atomic layers. We initially constructed this supercell using tetragonal 001 supercells containing 32 Ga and P atoms, which were cleaved from a crystalline GaP structure in the zinc blende form with an experimental lattice constant of 5.45 Å (a_0), at room temperature. The atoms within the second half of the supercell were completely replaced by Si atoms in order to obtain the GaP/Si supercell (Fig. 6.1). The dimensions of the supercell were $a = b = a_0$ and $c = 4a_0$. Following the previous studies [184, 225, 226], the supercell was purposefully chosen to be longer in the z direction to ensure that the interfaces do not see each other, and that the electronic structure of each material is recovered in the middle of its own side. We checked the latter condition by performing projected density of states (PDOS) analysis. After obtaining a supercell, we fixed the volume of the supercell, and then performed DFT calculations on the supercell so as to optimize the atomic structure and obtain the electronic properties.

We checked the accuracy of our DFT method by carrying out calculations of the charge density, electrostatic potential, and valence band offset of the well-known AlAs/GaAs heterojunction modeled by our supercell approach where we found a good agreement between our results and the obtained results in the previous study

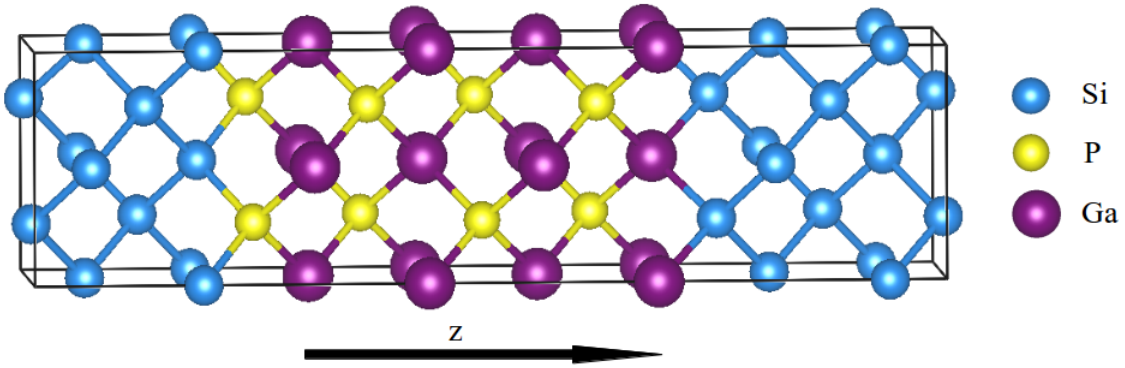

Figure 6.1: The atomic structure of the GaP/Si(001) supercell. The purple, yellow, and blue atoms correspond to Ga, P, and Si atoms, respectively. The arrow shows the z direction. The supercell consists of two types of interfaces: P-Si and Ga-Si.

[226]. We also found good agreement between our calculated and experimental valence band offsets for the GaP/Si heterojunction, as discussed in next section. Test calculations were also performed with the Becke-Lee-Yang-Parr (BLYP) exchange-correlation functional rather than the PBE functional on the GaP/Si supercell, where we found negligible difference in the general form of the electronic structure. Calculations were also carried out on AlP/Si heterojunctions in order to check the robustness of our results for other III-V/Si heterojunctions, where we found similar results for AlP/Si supercells as for GaP/Si.

In order to obtain the supercell structure of hydrogenated GaP/Si (GaP/Si:H) with 3% H (at.%=3), a single hydrogen atom was added to a fully relaxed supercell of GaP/Si with 32 atoms. Since the hydrogen atom can initially bond to any of the 32 atoms in the supercell, we carried out ion relaxation calculations at the DFT level on all the 32 possible configurations. The configuration with the lowest energy obtained from the ion relaxation calculations was then chosen as the most stable configuration. A similar procedure was performed for finding the most stable configuration of GaP/Si:H with 6% H, with the only difference being that a second hydrogen atom was added to the most stable configuration of GaP/Si:H with 3% H and the lowest

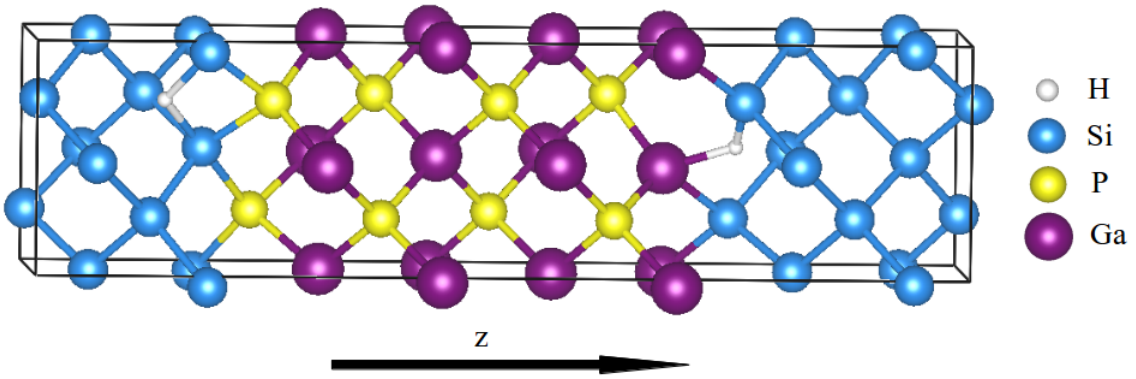

Figure 6.2: The atomic structure of the energetically most stable configuration of the GaP/Si:H supercell with H at.%=6. The purple, yellow, blue, and white atoms correspond to Ga, P, Si, and H atoms, respectively. At the P-Si interface, H atoms are only bonded to Si atoms due to the presence of the excess electron on the P atoms, but at the Ga-Si interface, H atoms are bonded to both Ga and Si atoms due to the deficiency of electrons in Ga atoms.

energy configuration found by a similar approach. The same strategy was used for generating GaP/Si:H with higher hydrogen concentrations (8.5% and 11.0%). Here, the atomic percentage of H is calculated for the whole supercell. For example, in the case of two H atoms in the supercell, since there are 34 atoms in the supercell, the H concentration is 6% (2/34×100%). In fact, the calculated concentration mentioned here is a volumetric concentration. However, since we have only 2 atoms in each xy plane of the supercell, for each H atom located at the interface, the surface atomic concentration of H would be 50%, if they are located there, which turns out to be the case in terms of the most energetically favorable positions for the H atoms.

6.2 Results

Figure 6.2 shows the GaP/Si:H supercell with 6% H, in its most stable configuration. In this energetically favored configuration, H atoms are only bonded to the atoms located at the interface layers. This H addition behavior is not unexpected. The presence of thermodynamically quite stable crystalline forms of GaP and Si on both sides of the interface implies that the H atoms in the most stable configurations bond

to atoms close to the interface, where the symmetry is broken.

The GaP/Si (001) supercell modeled in this study consists of two different types of interfaces, as shown in Fig. 6.1. 1 and 2. At one interface, P atoms only bond to Si atoms, while at the other, Ga atoms only bond to Si atoms. The relaxed bond lengths for P-Si and Ga-Si were found to be 2.42 Å and 2.30 Å, which are slightly different from the ideal bond lengths in bulk GaP and Si (2.35 Å). These bond lengths correspond to a 2% contraction of the P-Si bond and 3% expansion of the Ga-Si bond relative to the bond lengths present in bulk GaP and Si. The presence of these strained bonds explains why H preferentially bonds to interface atoms rather than bulk atoms in the supercell in terms of the lowest energy state.

As mentioned earlier, the interfaces of the GaP/Si(001) heterojunctions are heterovalent since the P-Si interface consists of group V and group IV bonding configuration, while the Ga-Si interface consists of group III and group IV bonding configuration. Therefore, there is a 1/4 electron excess for the Si-P interface and a 1/4 electron deficiency for the Si-Ga interface. This electron excess/deficiency is equivalent to a floating/dangling bond, which is a source of instability in the atomic structure. This instability could be another reason for preferential H bonding at the interface of GaP/Si heterojunctions. Due to the excess electron on P atoms, H is only bonded to the Si atoms of the P-Si bond, but due to the electron deficiency of Ga, H bonds to the Ga (with the bond length of 1.82 Å) and Si (with the bond length of 1.58 Å) atoms of the Ga-Si bond. As seen in Fig. 6.2, the H atom makes a bridge between two atoms at the interface, consistent with the ECM model discussed in the introduction. It is well known that H atoms bridge between two atoms in a molecule or a network of atoms under high strain, which lead to higher stability. There are many stable compounds with such H bonding [227]; some well known ones are Di-

borane (B_2H_6), Digallane (Ga_2H_6), polymeric hydride of Aluminum ($(AlH_3)_n$) and hydrogenated amorphous Silicon (a-Si:H). We observe that this H addition causes the average P-Si and Ga-Si bond length to become longer and shorter, respectively, with respect to their un-hydrogenated form.

Figure 6.3 shows the energy phase diagram of the supercell during the H addition process. As seen in Fig. 3, the GaP/Si(001) initially gets more stable after each H addition. However we observe that at 6% H (when each interface gets one H atom, Fig. 6.2), the highest stability (2.4 eV) is realized. For the case of having one H atom (3%) in the supercell, in the most stable configuration, the H atom bonds to the Ga-Si interface. For the case of having two H atoms (6%) in the supercell, in the most stable configuration, H atom bonds to the P-Si interface. Finally, the third and fourth H atom bonds to the Ga-Si interface and to the third H, respectively. This result shows that after adding the fourth H atom, there is no bond between this fourth H atom and either of the interfaces; instead the extra H atom makes a bond with the third inserted H atom to form a H2 molecule close to the interface, implying that we have reach a saturation point. Therefore, we stopped the H addition after inserting fourth H atom in the supercell, as there was no further benefit. It is worth noting that the energy difference between the first and the second most stable configurations is 0.20, 0.15, 0.19, and 0.27 eV for the case of having one, two, three, and four H atoms in the supercell, respectively.

As mentioned earlier, the details of the electronic properties of heterojunctions are extremely important for their functionality. In order to investigate the effect of H addition on the electronic structure, we carried out electronic structure calculations on GaP and Si in the bulk phase and also on GaP/Si and GaP/Si:H (with 6% H) heterojunctions. Figure 6.4a illustrates the electronic density of states (EDOS) of

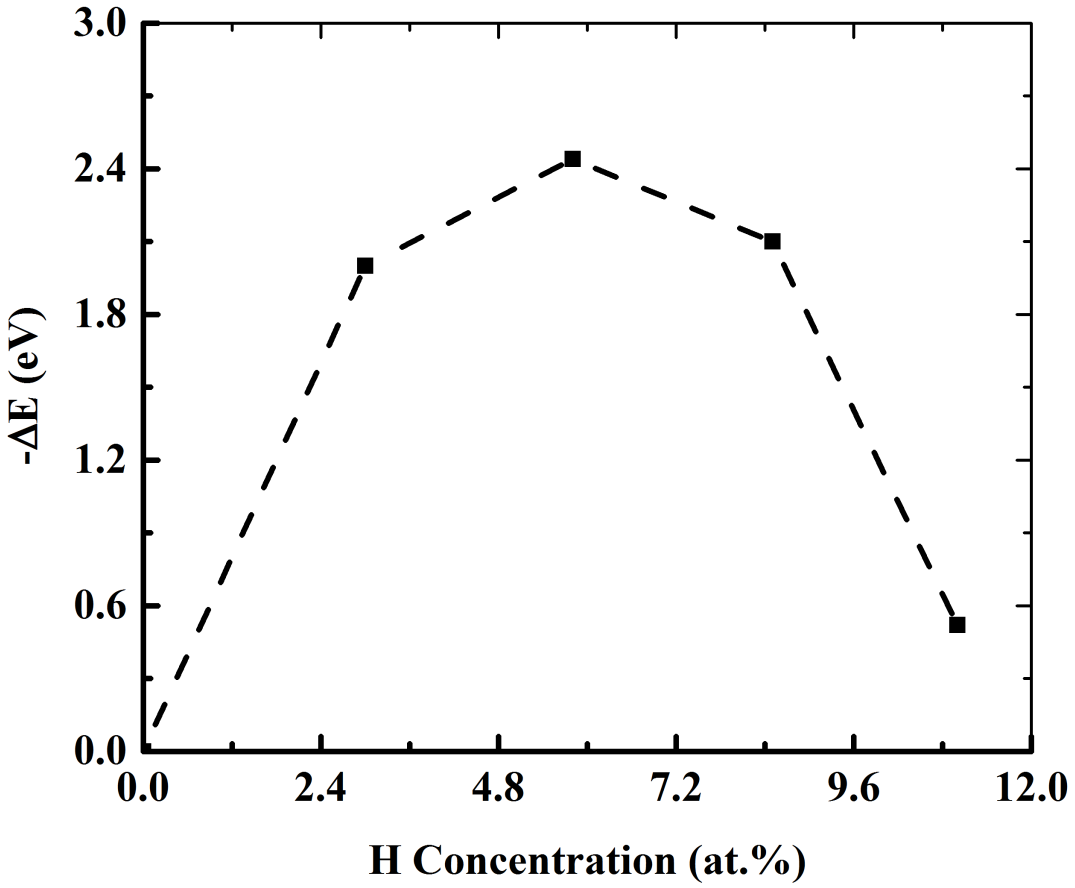

Figure 6.3: The energy phase diagram of GaP/Si(001) supercell during H addition. E is the energy change after each H addition.

bulk GaP and Si calculated using the DFT method described in the previous section. As seen in Fig. 6.4a, both the crystalline forms of bulk GaP and Si show clear valence band to conduction band energy gaps, and no states in the gaps, as expected. Since both GaP and Si are semiconductor materials, their Fermi energy levels are located at their respective valence band edges. The band-gap regions are 0.0-1.82 eV and 0.96-1.62 eV for bulk GaP and Si, respectively. Therefore, the bandgaps of GaP and Si overlap in the energy range of the Si bandgap, corresponding to a type I heterojunction. The calculated band-gaps are 1.82 eV and 0.66 eV for GaP and Si, respectively, smaller than the experimental values due to the well-known band-gap underestimation problem in conventional DFT.

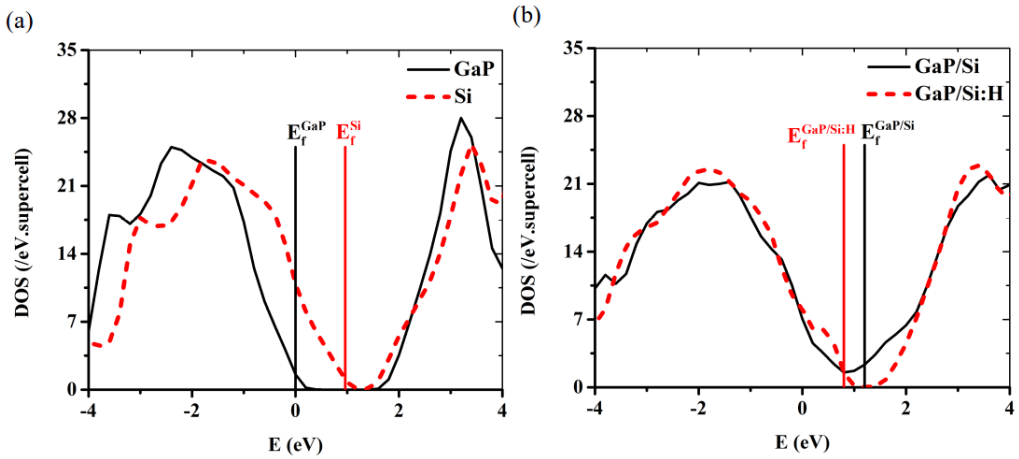

Figure 6.4: The electronic density of states of a) GaP vs. Si and b) GaP/Si vs. GaP/Si:H. Both GaP and Si have a clear band gap from 0.0-1.82 eV and 0.96-1.62 eV, respectively, and their Fermi energy levels are the edge of valence bands. Although the unpassivated GaP/Si hetrojunction contains many mid-gap states in the common forbidden band gap of its constituents, H modification of the interface reduces these mid-gap states, and shifts the Fermi energy level from forbidden gap to the valence band edge. We choose the reference energy to be the Fermi energy of the bulk GaP.

Figure 6.4b illustrates the EDOS of GaP/Si and GaP/Si:H heterojunction which are obtained from the DFT calculations performed on the GaP/Si(001) and GaP/Si:H supercell. In the simple picture, we expect that the EDOS of a GaP/Si heterojunction formed from crystalline GaP deposited on crystalline Si(001) should be a linear combination of the EDOS of bulk GaP and Si, which is what we observe in the electronically matched AlAs/GaAs supercell case. In comparing between the calculated EDOS plot of GaP/Si (Fig. 6.4b) and bulk GaP and Si (Fig. 4a), we see that the general form of the EDOS plot of the GaP heterojunction is almost a combination of the EDOS of its constituents. The main difference is that there is no bandgap, and that mid gap states exist in the overlap gap (0.96-1.62) between GaP and Si. As seen, the Fermi energy level is located in the forbidden gap. A comparison of the EDOS of the most stable configuration of GaP/Si:H with that of the GaP/Si heterojunction in Fig. 6.4b shows that the addition of hydrogen to the

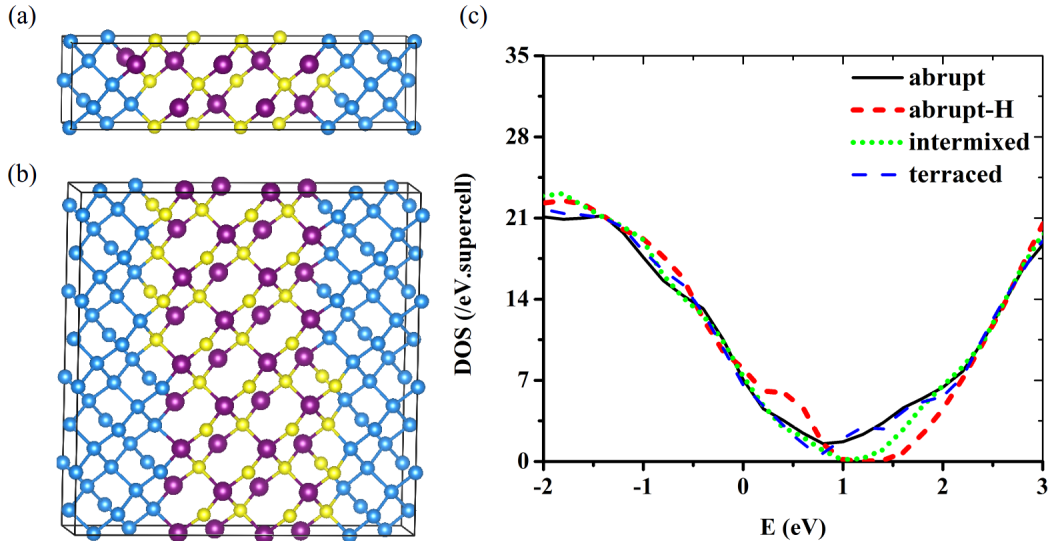

Figure 6.5: The atomic structure of the GaP/Si(001) supercell with a) the intermixed interface and b) with terraced interface. The purple, yellow, and blue atoms correspond to Ga, P, and Si atoms, respectively. C) The electronic density of states of GaP/Si(001) with different interface atomic structure.

interface atoms significantly reduces the mid-gap state density. This H addition shifts the Fermi energy level to lower energies from the mid-gap to the valence band edge.

Although it has been experimentally demonstrated that the GaP/Si(001) interface is typically abrupt [228], it has been proposed that the intermixed [229, 230] or terraced [231] GaP/Si(100) heterojunctions is thermodynamically more favorable than the abrupt one. Therefore, we performed the same calculations on intermixed (compensated) and terraced interfaces in order to compare the EDOS of the abrupt and hydrogenated structures with those of compensated and terraced interfaces. Figures 6.5a and 6.5b illustrate the supercells that we constructed for generating compensated and terraced interfaces, respectively. Figure 6.5c shows the EDOS obtained from compensated and terraced interfaces in comparison with that of an abrupt interface with and without H passivation. As seen in Fig. 6.5c we obtained the highest midgap state reduction for the hydrogenated abrupt interface as well as with the un-

hydrogenated fully compensated (intermixed) interface, as compared with the abrupt non-compensated interface. This reduction in interface state density with intermixing has been reported earlier [231], and as can be seen, the integrated density of states at midgap is roughly similar between the hydrogenated and the intermixed case, although there are differences in the distribution with energy. In fact, over the range of energies corresponding the Si bandgap (0.96-1.62 eV), the density of states of the hydrogenated abrupt interface is consistently lower than the intermixed case. Interestingly, for any amount of terracing at the interface, the interface state density degrades to that of the uncompensated abrupt interface, signifying that the advantages of intermixing are lost once terraces start to form. Our calculations showed that the hydrogenated abrupt GaP/Si(001) heterojunctions is more stable than the intermixed and terraced ones by 0.04 and 0.03 eV/atom, respectively. This higher stability could explain the relatively lower midgap state density for hydrogenated abrupt interface compared to those of intermixed and terraced interfaces. Hydrogenation of the intermixed interface has no substantial effect in reducing the midgap states, as expected since the intermixing already provides charge rebalancing. However, hydrogenation of the terraced interfaces, based on preliminary studies, did not significantly improve the midgap state density.

In order to investigate the atomic origin of the mid-gap states at the GaP/Si interface with and without hydrogenation, we performed an integrated densities of states (IDOS) analysis. The range of energy used for calculating the IDOS corresponds to the bulk bandgap of Si, 0.96-1.62 eV. The IDOS plot is depicted in Fig. 6.6. As seen, almost all the mid-gap states stem from the atoms at the interface. The presence of these mid-gap states in the EDOS of the GaP/Si heterojunction may be explained by an electron excess or deficiency, depending on the interface atom, as discussed earlier. The electron excess and deficiency cause floating and dangling

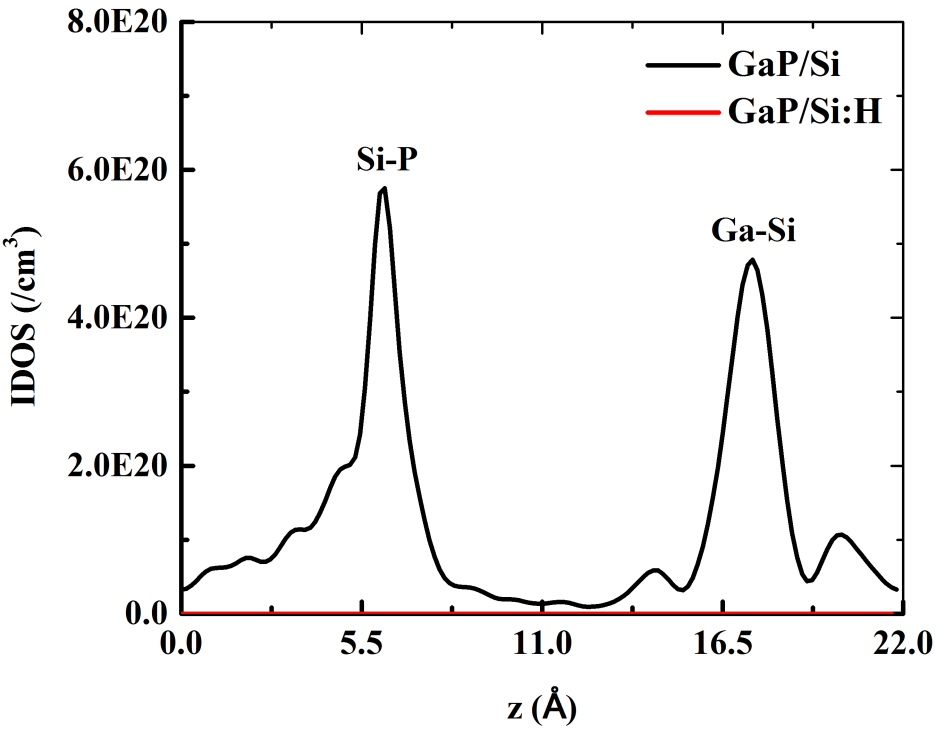

Figure 6.6: The integrated density of state (IDOS) of GaP/Si(001) in the (001) direction for the range of common forbidden gap of bulk GaP and Si. The two sharp peaks reveal the significant contribution of the atoms close to the P-Si and Ga-Si interfaces in creating mid-gap state density in the electronic structure of GaP/Si heterojunction.

bonds, respectively, which are the most important sources of defect states in the bulk, surface and interface of materials. These bonds usually result in a high density of electronic state in the forbidden gap. H atoms, on the other hand, can significantly reduce the mid-gap state density by passivating these floating and dangling bonds. As shown in Fig. 6.6, the IDOS with H reduces to zero on this linear plot.

We also examined the effect of H addition on the electron charge density distribution at the interface of GaP/Si. Figure 6.7a, b show the planar average of the electron charge density for abrupt Si-P, abrupt Ga-Si, and hydrogenated interface structures. The density was averaged in the plane (XY) over the two atomic layers and

divided by the volume of the supercell and the total number of Ga, P, and Si atoms (32) plotted along the (001) (z) direction. As shown in Fig. 6.7a, there is an electron charge accumulation at the P-Si interface and an electron charge depletion at the Ga-Si interface of GaP/Si(001), which produces band bending at the uncompensated interfaces, and a high electric field in the supercell. By adding H to the interface, this electron charge accumulation and depletion (Figs. 6.7a and 6.7b) changes to a typical macroscopic interface dipole [226]. This change can significantly influence the electrostatic potential line-up along the supercell and consequently change the band offset.

Figures 6.7c and 6.7d illustrate the macroscopic electrostatic potential energy dependency of the GaP/Si heterojunction along the (001) direction of the GaP/Si supercells without and with H, respectively. As can be seen, for supercells without hydrogen, the electrostatic potential energy shows a strong linear variation from one interface to another, whereas in the H containing system, the electrostatic potential energy is constant in the bulk. This linear dependency of the electrostatic potential might be the reason for the observation of different valence band offsets in GaP/Si(001) heterojunctions experimentally [200, 232–236]. The linear dependence of electrostatic potential is due to the large amount of partial charges accumulating at the interfaces [196, 200, 224]. However, the addition of H and the resulting dipole nature to the interface leads to a constant electrostatic potential. Based on the electrostatic potential energy change including the interface dipole contribution, we find the GaP/Si:H valence band offset to be 1.12 eV. Although there are a wide range of reported band offsets for the GaP/Si(001) heterojunction, our calculated band offset is consistent with the measured band offset reported by Sakata et al. and Roychowdhury et al. [232, 233]. The calculated valence band offset is consistent with the fact that the GaP on Si layer may serve as a carrier selective contact [237]. In terms of

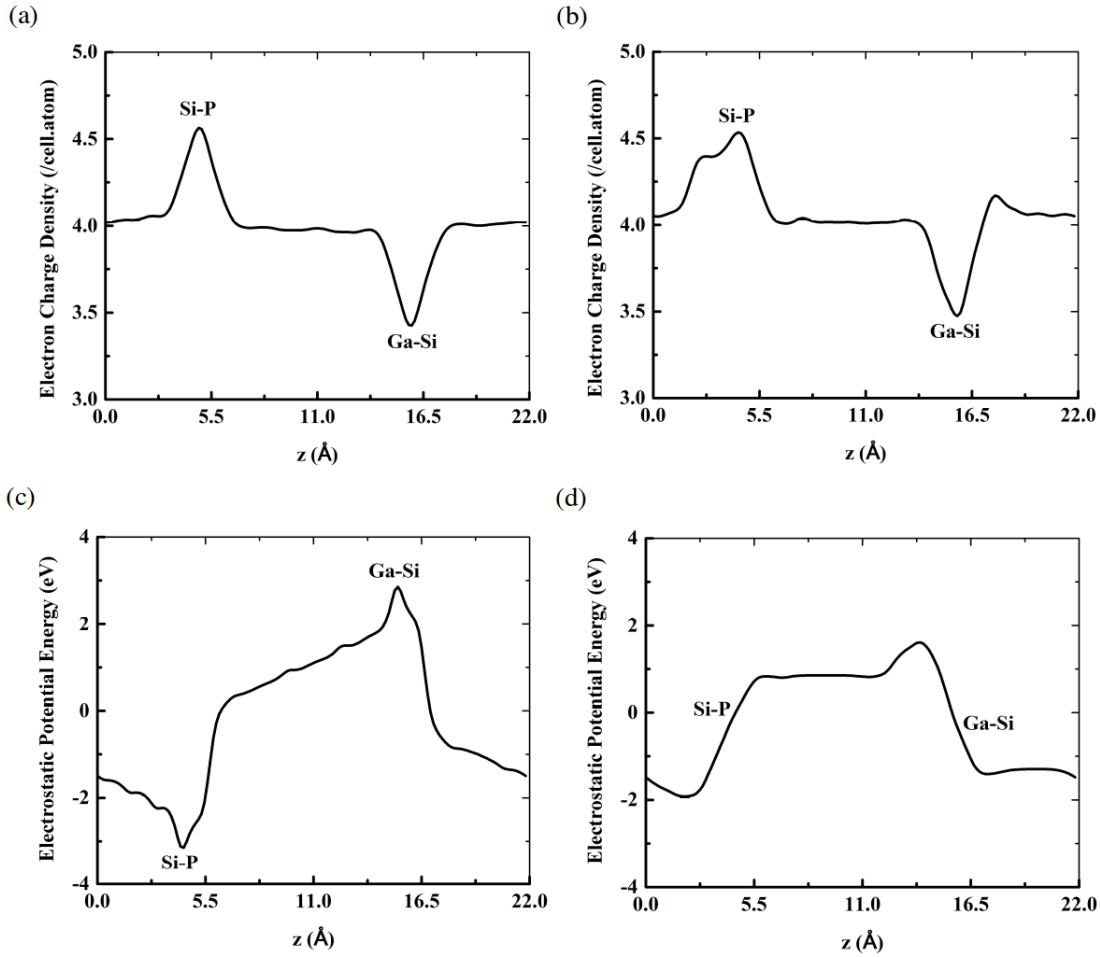

Figure 6.7: The macroscopic averaged number of electrons per cell per atom of GaP/Si(001) in the (001) direction for (a) without H and (b) with H. The macroscopic averaged electrostatic potential of GaP/Si(001) in the (001) direction for (c) without H and (d) with H. The Si-P and Ga-Si interfaces lie at 5.35 and 15 , respectively. The electronic charge density shape and electrostatic potential energy shape at the interfaces significantly vary with inserting H atoms.

this application, we believe that H atoms may tune the band offset of GaP/Si(001) heterojunction, by changing the charge distribution and passivating interface states.

Chapter 7

SUMMARY AND CONCLUSION

As the first part of my work, a well-defined MD-DFT method was perfomed to obtain the stable configuration of a-Si and a-Si:H. A good agreement between the calculated and experimental RDF indicates the validity of our structures to model the electronic properties of a-Si and a-Si:H. we found that, in the stable configurations, the addition of hydrogen atoms to a-Si leads to a decrease in midgap and band tail state density not only by passivating dangling bonds but also by removing strained-bonds. The calculated IPR factors using Kohn-Sham wavefunctions obtained from DFT calculations performed on different a-Si structures also indicated the importance of strained-bond in creating localized states. We found that the hydrogen atoms addition could extremely decrease the localization of orbitals in the mobility gap in the stable configurations but could be a source of extra midgap states and orbital localization in the less stable configurations. Based on the calculated localization in valance and conduction band tails, we also realized that a-Si:H can behave as different type of selective barriers in different H concentrations and different atomic configurations. Therefore, our results show the crucial importance of H concentration and annealing process in fabrication of a-Si:H-based HIT solar cells with high open circuit voltage.

As the second part of my work, the stable configuration of a-Si/c-Si and a-Si:H/c-Si were obtained using the previous MD-DFT method. The calculated RDF and DOS plots were in good agreement with experimental results which indicates the validity of our structures to model the electronic properties of a-Si/c-Si and a-Si:H/c-Si. The computed DOS plots obtained from DFT calculations performed on different configuration of a-Si:H/c-Si structures indicated H inserting always decrease the density of state in the forbidden gap and band tails but the amount of this

reduction depends on the H binding configuration. We found that in the most stable configurations we have the most in-gap and band-tail state reduction. By calculating IPR factors using Kohn-Sham wavefunctions and projecting DOS inside the band gap and mobility gap, we found that both H presence and its binding configuration are critical in determining the density of localized-defect states specially at the interface. Using band diagram calculation based on potential line-up method, we also found that although the hydrogen atoms similarly change the general form of band-diagram of a-Si/c-Si heterostructure for the all configuration, but the amount of band-bending depends on the configuration with the amount several tens of meV. Therefore, our results show the crucial importance of H concentration and annealing process in fabrication of a-Si:H-based HIT solar cells with high open circuit voltage.

As third part of my work, DFT calculation was performed on GaP/Si(001) hetrojunction as a prototype of lattice match III-V on Si hetrojunction in order to study their electronic properties. Low recombination and low defect GaP/Si interfaces are important in increasing the efficiency of Si-based solar cells. Despite being closely lattice matched, our results show that the abrupt GaP/Si interface contains a high-density interface states. These interfaces are improved with the addition of H, which substantially reduces the interface state density. The addition of hydrogen also changes the electrostatic potential at the interface, reducing the magnitude of the peaks. We also compared the electronic properties of the abrupt GaP/Si(001) heterojunction with and without H passivation to that of intermixed and terraced interfaces. We find that the hydrogenated abrupt GaP/Si(001) interface is thermodynamically more stable than both the intermixed and terraced interfaces. The reduction in the density of midgap states is similar between the H-passivated abrupt interface and the fully intermixed case of alternating cation and anions, with the H-passivated interface having a lower interface state density in the range of the Si

bandgap. However, any degree of terracing leads to high midgap density of states, similar to the abrupt unhydrogenated case. Overall, our results could explain the experimental results which to date giving relatively low open circuit voltages due to high recombination at the GaP/Si interfaces without either inter-diffusion or an a-Si interlayer [192, 238–240]. Further, the results show that the inclusion of hydrogen at the interface would be highly beneficial for realizing a low density of states at the interface, reducing recombination. In addition, we believe that the presence of H could provide additional stabilization of the GaP/Si (001) interface, which could reduce other structural defects such as antiphase disorder, micro-twins, dislocations, imperfect 3D nucleation/rough, etc., leading to improved photovoltaic performance.

REFERENCES

[1] "International technology roadmap for photovoltaic results 2016 incl. maturity report," http://www.itrpv.net/Reports/Downloads/, accessed: November 2017.

[2] C. Battaglia, A. Cuevas, and S. De Wolf, "High-efficiency crystalline silicon solar cells: status and perspectives," *Energy & Environmental Science*, vol. 9, no. 5, pp. 1552–1576, 2016.

[3] J. C. Bean, "Silicon-based semiconductor heterostructures: column iv bandgap engineering," *Proceedings of the IEEE*, vol. 80, no. 4, pp. 571–587, 1992.

[4] A. Franciosi and C. G. Van de Walle, "Heterojunction band offset engineering," *Surface Science Reports*, vol. 25, no. 1-4, pp. 1–140, 1996.

[5] W. Oldham and A. Milnes, "Interface states in abrupt semiconductor heterojunctions," *Solid-State Electronics*, vol. 7, no. 2, pp. 153–165, 1964.

[6] K. Laaziri, S. Kycia, S. Roorda, M. Chicoine, J. Robertson, J. Wang, and S. Moss, "High resolution radial distribution function of pure amorphous silicon," *Physical Review Letters*, vol. 82, no. 17, p. 3460, 1999.

[7] R. Bellisent, A. Menelle, W. Howells, A. C. Wright, T. Brunier, R. Sinclair, and F. Jansen, "The structure of amorphous si: H using steady state and pulsed neutron sources," *Physica B: Condensed Matter*, vol. 156, pp. 217–219, 1989.

[8] J. Singh, "Influence of disorder on the electronic structure of amorphous silicon," *Physical Review B*, vol. 23, no. 8, p. 4156, 1981.

[9] D. M. Powell, M. T. Winkler, H. Choi, C. B. Simmons, D. B. Needleman, and T. Buonassisi, "Crystalline silicon photovoltaics: a cost analysis framework for determining technology pathways to reach baseload electricity costs," *Energy & Environmental Science*, vol. 5, no. 3, pp. 5874–5883, 2012.

[10] A. C. Goodrich, D. M. Powell, T. L. James, M. Woodhouse, and T. Buonassisi, "Assessing the drivers of regional trends in solar photovoltaic manufacturing," *Energy & Environmental Science*, vol. 6, no. 10, pp. 2811–2821, 2013.

[11] K. Yoshikawa, H. Kawasaki, W. Yoshida, T. Irie, K. Konishi, K. Nakano, T. Uto, D. Adachi, M. Kanematsu, H. Uzu *et al.*, "Silicon heterojunction solar cell with interdigitated back contacts for a photoconversion efficiency over 26%," *Nature Energy*, vol. 2, p. 17032, 2017.

[12] T. Saga, "Advances in crystalline silicon solar cell technology for industrial mass production," *NPG Asia Materials*, vol. 2, no. 3, pp. 96–102, 2010.

[13] S. W. Glunz, "Crystalline silicon solar cells with high efficiency," in *Advanced concepts in photovoltaics*, A. J. Nozik, G. Conibeer, and M. C. Beard, Eds. Royal Society of Chemistry.

[14] R. Frischknecht, R. Itten, P. Sinha, M. de Wild-Scholten, J. Zhang, V. Fthenakis, H. Kim, M. Raugei, and M. Stucki, "Life cycle inventories and life cycle assessment of photovoltaic systems," *International Energy Agency (IEA) PVPS Task*, vol. 12, no. 9, 2015.

[15] M. Tanaka, M. Taguchi, T. Matsuyama, T. Sawada, S. Tsuda, S. Nakano, H. Hanafusa, and Y. Kuwano, "Development of new a-si/c-si heterojunction solar cells: Acj-hit (artificially constructed junction-heterojunction with intrinsic thin-layer)," *Japanese Journal of Applied Physics*, vol. 31, no. 11R, p. 3518, 1992.

[16] J. Pankove and M. Tarng, "Amorphous silicon as a passivant for crystalline silicon," *Applied Physics Letters*, vol. 34, no. 2, pp. 156–157, 1979.

[17] M. Taguchi, K. Kawamoto, S. Tsuge, T. Baba, H. Sakata, M. Morizane, K. Uchihashi, N. Nakamura, S. Kiyama, and O. Oota, "Hittm cells-high-efficiency crystalline si cells with novel structure," *Progress in Photovoltaics*, vol. 8, no. 5, pp. 503–514, 2000.

[18] T. Wang, E. Iwaniczko, M. Page, D. Levi, Y. Yan, H. Branz, and Q. Wang, "Effect of emitter deposition temperature on surface passivation in hot-wire chemical vapor deposited silicon heterojunction solar cells," *Thin Solid Films*, vol. 501, no. 1, pp. 284–287, 2006.

[19] H. Fujiwara and M. Kondo, "Effects of a-si: H layer thicknesses on the performance of a-si: H/ c-si heterojunction solar cells," *Journal of Applied Physics*, vol. 101, no. 5, p. 054516, 2007.

[20] S. De Wolf and M. Kondo, "Abruptness of a-si: H/ c-si interface revealed by carrier lifetime measurements," *Applied Physics Letters*, vol. 90, no. 4, p. 042111, 2007.

[21] Y. Yan, M. Page, T. Wang, M. Al-Jassim, H. M. Branz, and Q. Wang, "Atomic structure and electronic properties of c-si/ a-si: H heterointerfaces," *Applied physics letters*, vol. 88, no. 12, p. 121925, 2006.

[22] M. Taguchi, A. Terakawa, E. Maruyama, and M. Tanaka, "Obtaining a higher voc in hit cells," *Progress in photovoltaics: research and applications*, vol. 13, no. 6, pp. 481–488, 2005.

[23] M. Taguchi, A. Yano, S. Tohoda, K. Matsuyama, Y. Nakamura, T. Nishiwaki, K. Fujita, and E. Maruyama, "24.7% record efficiency hit solar cell on thin silicon wafer," *IEEE Journal of Photovoltaics*, vol. 4, no. 1, pp. 96–99, 2014.

[24] T. Tiedje, E. Yablonovitch, G. D. Cody, and B. G. Brooks, "Limiting efficiency of silicon solar cells," *IEEE Transactions on electron devices*, vol. 31, no. 5, pp. 711–716, 1984.

[25] A. Richter, M. Hermle, and S. W. Glunz, "Reassessment of the limiting efficiency for crystalline silicon solar cells," *IEEE Journal of Photovoltaics*, vol. 3, no. 4, pp. 1184–1191, 2013.

[26] S. De Wolf, A. Descoeudres, Z. C. Holman, and C. Ballif, "High-efficiency silicon heterojunction solar cells: A review," *green*, vol. 2, no. 1, pp. 7–24, 2012.

[27] M. Taguchi, E. Maruyama, and M. Tanaka, "Temperature dependence of amorphous/crystalline silicon heterojunction solar cells," *Japanese Journal of Applied Physics*, vol. 47, no. 2R, p. 814, 2008.

[28] Z. C. Holman, A. Descoeudres, L. Barraud, F. Z. Fernandez, J. P. Seif, S. De Wolf, and C. Ballif, "Current losses at the front of silicon heterojunction solar cells," *IEEE Journal of Photovoltaics*, vol. 2, no. 1, pp. 7–15, 2012.

[29] T. Schulze, L. Korte, F. Ruske, and B. Rech, "Band lineup in amorphous/crystalline silicon heterojunctions and the impact of hydrogen microstructure and topological disorder," *Physical Review B*, vol. 83, no. 16, p. 165314, 2011.

[30] S. De Wolf, B. Demaurex, A. Descoeudres, and C. Ballif, "Very fast light-induced degradation of a-si: H/c-si (100) interfaces," *Physical Review B*, vol. 83, no. 23, p. 233301, 2011.

[31] S. De Wolf, C. Ballif, and M. Kondo, "Kinetics of a-si: H bulk defect and a-si: H/c-si interface-state reduction," *Physical Review B*, vol. 85, no. 11, p. 113302, 2012.

[32] B. George, J. Behrends, A. Schnegg, T. Schulze, M. Fehr, L. Korte, B. Rech, K. Lips, M. Rohrmüller, E. Rauls *et al.*, "Atomic structure of interface states in silicon heterojunction solar cells," *Physical review letters*, vol. 110, no. 13, p. 136803, 2013.

[33] T. Schulze, H. Beushausen, C. Leendertz, A. Dobrich, B. Rech, and L. Korte, "Interplay of amorphous silicon disorder and hydrogen content with interface defects in amorphous/crystalline silicon heterojunctions," *Applied Physics Letters*, vol. 96, no. 25, p. 252102, 2010.

[34] J. Holovskỳ, S. De Wolf, P. Jiříček, and C. Ballif, "Attenuated total reflectance fourier-transform infrared spectroscopic investigation of silicon heterojunction solar cells," *Review of Scientific Instruments*, vol. 86, no. 7, p. 073108, 2015.

[35] H. Fujiwara and M. Kondo, "Real-time monitoring and process control in amorphous/ crystalline silicon heterojunction solar cells by spectroscopic ellipsometry and infrared spectroscopy," *Applied Physics Letters*, vol. 86, no. 3, p. 032112, 2005.

[36] A. Descoeudres, L. Barraud, S. De Wolf, B. Strahm, D. Lachenal, C. Guérin, Z. Holman, F. Zicarelli, B. Demaurex, J. Seif *et al.*, "Improved amorphous/crystalline silicon interface passivation by hydrogen plasma treatment," *Applied Physics Letters*, vol. 99, no. 12, p. 123506, 2011.

[37] J. Geissbühler, S. De Wolf, B. Demaurex, J. P. Seif, D. T. Alexander, L. Barraud, and C. Ballif, "Amorphous/crystalline silicon interface defects induced by hydrogen plasma treatments," *Applied Physics Letters*, vol. 102, no. 23, p. 231604, 2013.

[38] R. Bartlome, S. De Wolf, B. Demaurex, C. Ballif, E. Amanatides, and D. Mataras, "Practical silicon deposition rules derived from silane monitoring during plasma-enhanced chemical vapor deposition a," *Journal of Applied Physics*, vol. 117, no. 20, p. 203303, 2015.

[39] L. Korte and M. Schmidt, "Investigation of gap states in phosphorous-doped ultra-thin a-si: H by near-uv photoelectron spectroscopy," *Journal of Non-Crystalline Solids*, vol. 354, no. 19, pp. 2138–2143, 2008.

[40] S. De Wolf and M. Kondo, "Nature of doped a-si: H/c-si interface recombination," *Journal of Applied Physics*, vol. 105, no. 10, p. 103707, 2009.

[41] C. Leendertz, N. Mingirulli, T. Schulze, J.-P. Kleider, B. Rech, and L. Korte, "Discerning passivation mechanisms at a-si: H/c-si interfaces by means of photoconductance measurements," *Applied Physics Letters*, vol. 98, no. 20, p. 202108, 2011.

[42] A. Descoeudres, Z. C. Holman, L. Barraud, S. Morel, S. De Wolf, and C. Ballif, "¿ 21% efficient silicon heterojunction solar cells on n-and p-type wafers compared," *IEEE Journal of Photovoltaics*, vol. 3, no. 1, pp. 83–89, 2013.

[43] M. Bivour, S. Schroeer, M. Hermle, and S. W. Glunz, "Silicon heterojunction rear emitter solar cells: Less restrictions on the optoelectrical properties of front side tcos," *Solar Energy Materials and Solar Cells*, vol. 122, pp. 120–129, 2014.

[44] R. Varache, O. N. Aguila, A. Valla, N. Nguyen, and D. Munoz, "Role of the front electron collector in rear emitter silicon heterojunction solar cells," *IEEE Journal of Photovoltaics*, vol. 5, no. 3, pp. 711–717, 2015.

[45] J. Geissbühler, S. De Wolf, A. Faes, N. Badel, Q. Jeangros, A. Tomasi, L. Barraud, A. Descoeudres, M. Despeisse, and C. Ballif, "Silicon heterojunction solar cells with copper-plated grid electrodes: status and comparison with silver

thick-film techniques," *IEEE Journal of Photovoltaics*, vol. 4, no. 4, pp. 1055–1062, 2014.

[46] J. B. Heng, J. Fu, B. Kong, Y. Chae, W. Wang, Z. Xie, A. Reddy, K. Lam, C. Beitel, C. Liao *et al.*, "¿ 23% high-efficiency tunnel oxide junction bifacial solar cell with electroplated cu gridlines," *IEEE Journal of Photovoltaics*, vol. 5, no. 1, pp. 82–86, 2015.

[47] L. Tous, S. N. Granata, P. Choulat, T. Bearda, A. Michel, A. Uruena, E. Cornagliotti, M. Aleman, R. Gehlhaar, R. Russell *et al.*, "Process simplifications in large area hybrid silicon heterojunction solar cells," *Solar Energy Materials and Solar Cells*, vol. 142, pp. 66–74, 2015.

[48] T. Mueller, S. Schwertheim, M. Scherff, and W. R. Fahrner, "High quality passivation for heterojunction solar cells by hydrogenated amorphous silicon suboxide films," *Applied Physics Letters*, vol. 92, no. 3, p. 033504, 2008.

[49] L. Mazzarella, S. Kirner, B. Stannowski, L. Korte, B. Rech, and R. Schlatmann, "p-type microcrystalline silicon oxide emitter for silicon heterojunction solar cells allowing current densities above 40 ma/cm2," *Applied Physics Letters*, vol. 106, no. 2, p. 023902, 2015.

[50] M. Boccard and Z. C. Holman, "Amorphous silicon carbide passivating layers for crystalline-silicon-based heterojunction solar cells," *Journal of Applied Physics*, vol. 118, no. 6, p. 065704, 2015.

[51] T. Koida, H. Fujiwara, and M. Kondo, "Hydrogen-doped in2o3 as high-mobility transparent conductive oxide," *Japanese Journal of Applied Physics*, vol. 46, no. 7L, p. L685, 2007.

[52] T. Koida, H. Fujiwara, and Kondo, "Reduction of optical loss in hydrogenated amorphous silicon/crystalline silicon heterojunction solar cells by high-mobility hydrogen-doped in2o3 transparent conductive oxide," *Applied physics express*, vol. 1, no. 4, p. 041501, 2008.

[53] F. Meng, J. Shi, Z. Liu, Y. Cui, Z. Lu, and Z. Feng, "High mobility transparent conductive w-doped in 2 o 3 thin films prepared at low substrate temperature and its application to solar cells," *Solar Energy Materials and Solar Cells*, vol. 122, pp. 70–74, 2014.

[54] E. Kobayashi, Y. Watabe, and T. Yamamoto, "High-mobility transparent conductive thin films of cerium-doped hydrogenated indium oxide," *Applied Physics Express*, vol. 8, no. 1, p. 015505, 2014.

[55] M. Morales-Masis, S. M. De Nicolas, J. Holovsky, S. De Wolf, and C. Ballif, "Low-temperature high-mobility amorphous izo for silicon heterojunction solar cells," *IEEE Journal of Photovoltaics*, vol. 5, no. 5, pp. 1340–1347, 2015.

[56] R. Rößler, C. Leendertz, L. Korte, N. Mingirulli, and B. Rech, "Impact of the transparent conductive oxide work function on injection-dependent a-si: H/c-si band bending and solar cell parameters," *Journal of Applied Physics*, vol. 113, no. 14, p. 144513, 2013.

[57] A. Tomasi, F. Sahli, J. P. Seif, L. Fanni, S. M. de Nicolas Agut, J. Geissbühler, B. Paviet-Salomon, S. Nicolay, L. Barraud, B. Niesen *et al.*, "Transparent electrodes in silicon heterojunction solar cells: Influence on contact passivation," *IEEE Journal of Photovoltaics*, vol. 6, no. 1, pp. 17–27, 2016.

[58] A. Tomasi, B. Paviet-Salomon, D. Lachenal, S. M. de Nicolas, A. Descoeudres, J. Geissbühler, S. De Wolf, and C. Ballif, "Back-contacted silicon heterojunction solar cells with efficiency¿ 21%," *IEEE Journal of Photovoltaics*, vol. 4, no. 4, pp. 1046–1054, 2014.

[59] G. Hautier, A. Miglio, G. Ceder, G.-M. Rignanese, and X. Gonze, "Identification and design principles of low hole effective mass p-type transparent conducting oxides," *Nature communications*, vol. 4, p. 2292, 2013.

[60] M. Bivour, S. Schröer, and M. Hermle, "Numerical analysis of electrical tco/a-si: H (p) contact properties for silicon heterojunction solar cells," *Energy Procedia*, vol. 38, pp. 658–669, 2013.

[61] B. Demaurex, S. De Wolf, A. Descoeudres, Z. Charles Holman, and C. Ballif, "Damage at hydrogenated amorphous/crystalline silicon interfaces by indium tin oxide overlayer sputtering," *Applied Physics Letters*, vol. 101, no. 17, p. 171604, 2012.

[62] B. Demaurex, J. P. Seif, S. Smit, B. Macco, W. E. Kessels, J. Geissbühler, S. De Wolf, and C. Ballif, "Atomic-layer-deposited transparent electrodes for silicon heterojunction solar cells," *IEEE Journal of Photovoltaics*, vol. 4, no. 6, pp. 1387–1396, 2014.

[63] Z. C. Holman, A. Descoeudres, S. De Wolf, and C. Ballif, "Record infrared internal quantum efficiency in silicon heterojunction solar cells with dielectric/metal rear reflectors," *IEEE Journal of Photovoltaics*, vol. 3, no. 4, pp. 1243–1249, 2013.

[64] M. Otto, M. Kroll, T. Käsebier, S.-M. Lee, M. Putkonen, R. Salzer, P. T. Miclea, and R. B. Wehrspohn, "Conformal transparent conducting oxides on black silicon," *Advanced Materials*, vol. 22, no. 44, pp. 5035–5038, 2010.

[65] K. Tanabe, K. Watanabe, and Y. Arakawa, "Iii-v/si hybrid photonic devices by direct fusion bonding," *Scientific reports*, vol. 2, p. 349, 2012.

[66] L. Kleinman, "Comment on the average potential of a wigner solid," *Physical Review B*, vol. 24, no. 12, p. 7412, 1981.

[67] P. Hohenberg and W. Kohn, "Inhomogeneous electron gas," *Physical review*, vol. 136, no. 3B, p. B864, 1964.

[68] W. Kohn and L. J. Sham, "Self-consistent equations including exchange and correlation effects," *Physical review*, vol. 140, no. 4A, p. A1133, 1965.

[69] W. Oldham and Milnes, "n-n semiconductor heterojunctions," *Solid-State Electronics*, vol. 6, no. 2, pp. 121–132, 1963.

[70] A. Richter, S. W. Glunz, F. Werner, J. Schmidt, and A. Cuevas, "Improved quantitative description of auger recombination in crystalline silicon," *Physical Review B*, vol. 86, no. 16, p. 165202, 2012.

[71] R. Hezel and K. Jaeger, "Low-temperature surface passivation of silicon for solar cells," *Journal of the Electrochemical Society*, vol. 136, no. 2, pp. 518–523, 1989.

[72] A. G. Aberle, "Surface passivation of crystalline silicon solar cells: a review," *Progress in Photovoltaics: Research and Applications*, vol. 8, no. 5, pp. 473–487, 2000.

[73] B. Richards, "Comparison of tio2 and other dielectric coatings for buried-contact solar cells: a review," *Progress in Photovoltaics: Research and Applications*, vol. 12, no. 4, pp. 253–281, 2004.

[74] E. Yablonovitch, D. Allara, C. Chang, T. Gmitter, and T. Bright, "Unusually low surface-recombination velocity on silicon and germanium surfaces," *Physical review letters*, vol. 57, no. 2, p. 249, 1986.

[75] D. Fenner, D. Biegelsen, and R. Bringans, "Silicon surface passivation by hydrogen termination: A comparative study of preparation methods," *Journal of Applied Physics*, vol. 66, no. 1, pp. 419–424, 1989.

[76] G. Higashi, Y. Chabal, G. Trucks, and K. Raghavachari, "Ideal hydrogen termination of the si (111) surface," *Applied Physics Letters*, vol. 56, no. 7, pp. 656–658, 1990.

[77] J. J. Boland, "Scanning tunnelling microscopy of the interaction of hydrogen with silicon surfaces," *Advances in Physics*, vol. 42, no. 2, pp. 129–171, 1993.

[78] S. Glunz, D. Biro, S. Rein, and W. Warta, "Field-effect passivation of the sio 2 si interface," *Journal of Applied Physics*, vol. 86, no. 1, pp. 683–691, 1999.

[79] B. Hoex, J. Gielis, M. Van de Sanden, and W. Kessels, "On the c-si surface passivation mechanism by the negative-charge-dielectric al 2 o 3," *Journal of Applied Physics*, vol. 104, no. 11, p. 113703, 2008.

[80] W. D. Eades and R. M. Swanson, "Calculation of surface generation and recombination velocities at the si-sio2 interface," *Journal of applied Physics*, vol. 58, no. 11, pp. 4267–4276, 1985.

[81] E. Yablonovitch, R. Swanson, W. Eades, and B. Weinberger, "Electron-hole recombination at the si-sio2 interface," *Applied Physics Letters*, vol. 48, no. 3, pp. 245–247, 1986.

[82] A. G. Aberle, S. Glunz, and W. Warta, "Impact of illumination level and oxide parameters on shockley–read–hall recombination at the si-sio2 interface," *Journal of Applied Physics*, vol. 71, no. 9, pp. 4422–4431, 1992.

[83] K. Yasutake, Z. Chen, S. Pang, and A. Rohatgi, "Modeling and characterization of interface state parameters and surface recombination velocity at plasma enhanced chemical vapor deposited sio2–si interface," *Journal of applied physics*, vol. 75, no. 4, pp. 2048–2054, 1994.

[84] O. Schultz, S. Glunz, and G. Willeke, "Accelerated publication: Multicrystalline silicon solar cells exceeding 20% efficiency," *Progress in Photovoltaics: Research and Applications*, vol. 12, no. 7, pp. 553–558, 2004.

[85] T. Lauinger, J. Schmidt, A. G. Aberle, and R. Hezel, "Record low surface recombination velocities on 1 ω cm p-silicon using remote plasma silicon nitride passivation," *Applied Physics Letters*, vol. 68, no. 9, pp. 1232–1234, 1996.

[86] M. Kerr, J. Schmidt, A. Cuevas, and J. Bultman, "Surface recombination velocity of phosphorus-diffused silicon solar cell emitters passivated with plasma enhanced chemical vapor deposited silicon nitride and thermal silicon oxide," *Journal of applied physics*, vol. 89, no. 7, pp. 3821–3826, 2001.

[87] H. Mäckel and R. Lüdemann, "Detailed study of the composition of hydrogenated sin x layers for high-quality silicon surface passivation," *Journal of applied physics*, vol. 92, no. 5, pp. 2602–2609, 2002.

[88] A. G. Aberle, "Overview on sin surface passivation of crystalline silicon solar cells," *Solar energy materials and solar cells*, vol. 65, no. 1, pp. 239–248, 2001.

[89] I. Martın, M. Vetter, A. Orpella, J. Puigdollers, A. Cuevas, and R. Alcubilla, "Surface passivation of p-type crystalline si by plasma enhanced chemical vapor deposited amorphous sic x: H films," *Applied Physics Letters*, vol. 79, no. 14, pp. 2199–2201, 2001.

[90] S. Janz, S. Riepe, M. Hofmann, S. Reber, and S. Glunz, "Phosphorus-doped sic as an excellent p-type si surface passivation layer," *Applied Physics Letters*, vol. 88, no. 13, p. 133516, 2006.

[91] G. Agostinelli, A. Delabie, P. Vitanov, Z. Alexieva, H. Dekkers, S. De Wolf, and G. Beaucarne, "Very low surface recombination velocities on p-type silicon wafers passivated with a dielectric with fixed negative charge," *Solar Energy Materials and Solar Cells*, vol. 90, no. 18, pp. 3438–3443, 2006.

[92] B. Hoex, S. Heil, E. Langereis, M. Van de Sanden, and W. Kessels, "Ultralow surface recombination of c-si substrates passivated by plasma-assisted atomic layer deposited al 2 o 3," *Applied Physics Letters*, vol. 89, no. 4, p. 042112, 2006.

[93] G. Dingemans and W. Kessels, "Status and prospects of al2o3-based surface passivation schemes for silicon solar cells," *Journal of Vacuum Science & Technology A: Vacuum, Surfaces, and Films*, vol. 30, no. 4, p. 040802, 2012.

[94] S. Olibet, E. Vallat-Sauvain, and C. Ballif, "Model for a-si: H/c-si interface recombination based on the amphoteric nature of silicon dangling bonds," *Physical Review B*, vol. 76, no. 3, p. 035326, 2007.

[95] J. Zhao, A. Wang, and M. A. Green, "24· 5% efficiency silicon pert cells on mcz substrates and 24· 7% efficiency perl cells on fz substrates," *Progress in Photovoltaics: Research and Applications*, vol. 7, no. 6, pp. 471–474, 1999.

[96] R. A. Street, *Hydrogenated amorphous silicon*. Cambridge University Press, 2005.

[97] M. Tosolini, L. Colombo, and M. Peressi, "Atomic-scale model of c-si/a-si:h interfaces," *Physical Review B*, vol. 69, no. 7, p. 075301, 2004.

[98] M. Nolan, M. Legesse, and G. Fagas, "Surface orientation effects in crystalline–amorphous silicon interfaces," *Physical Chemistry Chemical Physics*, vol. 14, no. 43, pp. 15 173–15 179, 2012.

[99] A. Aparna, V. Brahmajirao, and T. Karthikeyan, "Review on synthesis and characterization of gallium phosphide," *Procedia materials science*, vol. 6, pp. 1650–1657, 2014.

[100] X. Lu, X. Gao, C. Li, J. Ren, X. Guo, and P. La, "Electronic structure and optical properties of doped gallium phosphide: A first-principles simulation," *Physics Letters A*, vol. 381, no. 35, pp. 2986–2992, 2017.

[101] J. Tersoff, "Modeling solid-state chemistry: Interatomic potentials for multicomponent systems," *Physical Review B*, vol. 39, no. 8, p. 5566, 1989.

[102] A. D. Becke, "Density-functional thermochemistry. i. the effect of the exchange-only gradient correction," *The Journal of chemical physics*, vol. 96, no. 3, pp. 2155–2160, 1992.

[103] C. Lee, W. Yang, and R. G. Parr, "Development of the colle-salvetti correlation-energy formula into a functional of the electron density," *Physical Review B*, vol. 37, no. 2, p. 785, 1988.

[104] R. Krishnan, J. S. Binkley, R. Seeger, and J. A. Pople, "Self-consistent molecular orbital methods. xx. a basis set for correlated wave functions," *The Journal of Chemical Physics*, vol. 72, no. 1, pp. 650–654, 1980.

[105] J. P. Perdew, K. Burke, and M. Ernzerhof, "Generalized gradient approximation made simple," *Physical review letters*, vol. 77, no. 18, p. 3865, 1996.

[106] L. J. Bartolotti and K. Flurchick, "An introduction to density functional theory," *Reviews in computational chemistry*, vol. 7, pp. 187–260, 1996.

[107] A. D. Becke, "Density-functional exchange-energy approximation with correct asymptotic behavior," *Physical review A*, vol. 38, no. 6, p. 3098, 1988.

[108] H. J. Monkhorst and J. D. Pack, "Special points for brillouin-zone integrations," *Physical review B*, vol. 13, no. 12, p. 5188, 1976.

[109] R. Street, *Technology and applications of amorphous silicon*. Springer Science & Business Media, 2013, vol. 37.

[110] M. J. Powell, "The physics of amorphous-silicon thin-film transistors," *IEEE Transactions on Electron Devices*, vol. 36, no. 12, pp. 2753–2763, 1989.

[111] J. Poortmans and V. Arkhipov, *Thin film solar cells: fabrication, characterization and applications*. John Wiley & Sons, 2006, vol. 5.

[112] L. E. Antonuk, J. M. Boudry, C.-W. Kim, M. Longo, E. Morton, J. Yorkston, and R. A. Street, "Signal, noise, and readout considerations in the development of amorphous silicon photodiode arrays for radiotherapy and diagnostic x-ray imaging," in *Medical Imaging'91, San Jose, CA*. International Society for Optics and Photonics, 1991, pp. 108–119.

[113] J. Mort, F. Jansen, S. Grammatica, M. Morgan, and I. Chen, "Field-effect phenomena in hydrogenated amorphous silicon photoreceptors," *Journal of Applied Physics*, vol. 55, no. 8, pp. 3197–3198, 1984.

[114] D. E. Carlson and C. R. Wronski, "Amorphous silicon solar cell," *Applied Physics Letters*, vol. 28, no. 11, pp. 671–673, 1976.

[115] T. Shimizu, "Staebler-wronski effect in hydrogenated amorphous silicon and related alloy films," *Japanese Journal of Applied Physics*, vol. 43, no. 6R, p. 3257, 2004.

[116] E. Stratakis, E. Spanakis, P. Tzanetakis, H. Fritzsche, S. Guha, and J. Yang, "Photoinduced stress in hydrogenated amorphous silicon films," *Applied Physics Letters*, vol. 80, no. 10, p. 1734, 2002.

[117] T. Gotoh, S. Nonomura, M. Nishio, S. Nitta, M. Kondo, and A. Matsuda, "Experimental evidence of photoinduced expansion in hydrogenated amorphous silicon using bending detected optical lever method," *Applied Physics Letters*, vol. 72, no. 23, p. 2978, 1998.

[118] P. Khomyakov, W. Andreoni, N. Afify, and A. Curioni, "Large-scale simulations of a-si: H: The origin of midgap states revisited," *Physical Review Letters*, vol. 107, no. 25, p. 255502, 2011.

[119] M. Stutzmann, W. Jackson, and C. Tsai, "Light-induced metastable defects in hydrogenated amorphous silicon: A systematic study," *Physical Review B*, vol. 32, no. 1, p. 23, 1985.

[120] H. M. Branz, "Hydrogen collision model: Quantitative description of metastability in amorphous silicon," *Physical Review B*, vol. 59, no. 8, p. 5498, 1999.

[121] L. K. Wagner and J. C. Grossman, "Microscopic description of light induced defects in amorphous silicon solar cells," *Physical Review Letters*, vol. 101, no. 26, p. 265501, 2008.

[122] K. Jarolimek, R. De Groot, G. De Wijs, and M. Zeman, "First-principles study of hydrogenated amorphous silicon," *Physical Review B*, vol. 79, no. 15, p. 155206, 2009.

[123] D. C. Allan, J. Joannopoulos, and W. B. Pollard, "Electronic states and total energies in hydrogenated amorphous silicon," *Physical Review B*, vol. 25, no. 2, p. 1065, 1982.

[124] R. Car and M. Parrinello, "Structural, dymanical, and electronic properties of amorphous silicon: an ab initio molecular-dynamics study," *Physical Review Letters*, vol. 60, no. 3, p. 204, 1988.

[125] F. Buda, G. L. Chiarotti, R. Car, and M. Parrinello, "Structure of hydrogenated amorphous silicon from ab initio molecular dynamics," *Physical Review B*, vol. 44, no. 11, p. 5908, 1991.

[126] P. Fedders and D. Drabold, "Hydrogen and defects in first-principles molecular-dynamics-modeled a-si: H," *Physical Review B*, vol. 47, no. 20, p. 13277, 1993.

[127] B. Tuttle and J. B. Adams, "Structure of a-si: H from harris-functional molecular dynamics," *Physical Review B*, vol. 53, no. 24, p. 16265, 1996.

[128] P. Klein, H. M. Urbassek, and T. Frauenheim, "Tight-binding molecular-dynamics study of a- s i: H: Preparation, structure, and dynamics," *Physical Review B*, vol. 60, no. 8, p. 5478, 1999.

[129] A. A. Valladares, F. Alvarez, Z. Liu, J. Sticht, and J. Harris, "Ab initio studies of the atomic and electronic structure of pure and hydrogenated a-si," *The European Physical Journal B-Condensed Matter and Complex Systems*, vol. 22, no. 4, pp. 443–453, 2001.

[130] K. Winer and F. Wooten, "Structure and vibrational spectra of a model of a-si: H with periodic boundary conditions," *Physica Status Solidi (b)*, vol. 124, no. 2, pp. 473–480, 1984.

[131] N. Mousseau and L. J. Lewis, "Computer models for amorphous silicon hydrides," *Physical Review B*, vol. 41, no. 6, p. 3702, 1990.

[132] J. Holender, G. Morgan, and R. Jones, "Model of hydrogenated amorphous silicon and its electronic structure," *Physical Review B*, vol. 47, no. 7, p. 3991, 1993.

[133] I. Kwon, R. Biswas, and C. Soukoulis, "Molecular-dynamics simulations of defect formation in hydrogenated amorphous silicon," *Physical Review B*, vol. 45, no. 7, p. 3332, 1992.

[134] M. Ishimaru, S. Munetoh, and T. Motooka, "Generation of amorphous silicon structures by rapid quenching: A molecular-dynamics study," *Physical Review B*, vol. 56, no. 23, p. 15133, 1997.

[135] I. Štich, R. Car, and M. Parrinello, "Amorphous silicon studied by ab initio molecular dynamics: Preparation, structure, and properties," *Physical Review B*, vol. 44, no. 20, p. 11092, 1991.

[136] M. Legesse, M. Nolan, and G. Fagas, "A first principles analysis of the effect of hydrogen concentration in hydrogenated amorphous silicon on the formation of strained si-si bonds and the optical and mobility gaps," *Journal of Applied Physics*, vol. 115, no. 20, p. 203711, 2014.

[137] J. March, *Advanced organic chemistry: reactions, mechanisms, and structure*. John Wiley & Sons,, 1992.

[138] D. Cremer and E. Kraka, "A description of the chemical bond in terms of local properties of electron density and energy," *Croat. Chem. Acta*, vol. 57, no. 6, pp. 1259–1281, 1984.

[139] M. Powell and S. Deane, "Improved defect-pool model for charged defects in amorphous silicon," *Physical Review B*, vol. 48, no. 15, p. 10815, 1993.

[140] M. J. Powell and S. C. Deane, "Defect-pool model and the hydrogen density of states in hydrogenated amorphous silicon," *Physical Review B*, vol. 53, no. 15, p. 10121, 1996.

[141] J. Nelson, *The physics of solar cells*. World Scientific Publishing Co Inc, 2003.

[142] G. Cody, T. Tiedje, B. Abeles, B. Brooks, and Y. Goldstein, "Disorder and the optical-absorption edge of hydrogenated amorphous silicon," *Physical Review Letters*, vol. 47, no. 20, p. 1480, 1981.

[143] P. Fedders, D. Drabold, and S. Nakhmanson, "Theoretical study on the nature of band-tail states in amorphous si," *Physical Review B*, vol. 58, no. 23, p. 15624, 1998.

[144] Y. Hayashi, D. Li, A. Ogura, and Y. Ohshita, "Role of i-asi: H layers in asi: H/csi heterojunction solar cells," *IEEE Journal of Photovoltaics*, vol. 3, no. 4, pp. 1149–1155, 2013.

[145] A. Smets, W. Kessels, and M. Van de Sanden, "Vacancies and voids in hydrogenated amorphous silicon," *Applied physics letters*, vol. 82, no. 10, pp. 1547–1549, 2003.

[146] W. Lei, D. Liu, X. Chen, P. Zhu, Q. Cui, and G. Zou, "Ferromagnetic properties of y-doped aln nanorods," *The Journal of Physical Chemistry C*, vol. 114, no. 37, pp. 15 574–15 577, 2010.

[147] A. Pedersen, L. Pizzagalli, and H. Jónsson, "Optimal atomic structure of amorphous silicon obtained from density functional theory calculations," *New J. Phys*, vol. 19, p. 063018, 2017.

[148] J. Dong and D. Drabold, "Atomistic structure of band-tail states in amorphous silicon," *Physical Review Letters*, vol. 80, no. 9, p. 1928, 1998.

[149] N. W. Ashcroft and N. D. Mermin, *Solid state physics*. Holt, Rinehart and Winston, 1976.

[150] A. Moore, "Electron and hole drift mobility in amorphous silicon," *Applied Physics Letters*, vol. 31, no. 11, pp. 762–764, 1977.

[151] J. Marshall, R. Street, and M. Thompson, "Electron drift mobility in amorphous si: H," *Philosophical magazine B*, vol. 54, no. 1, pp. 51–60, 1986.

[152] D. Drabold, "Silicon: the gulf between crystalline and amorphous," *physica status solidi (RRL)–Rapid Research Letters*, vol. 5, no. 10-11, pp. 359–360, 2011.

[153] E. Holmström, B. Haberl, O. H. Pakarinen, K. Nordlund, F. Djurabekova, R. Arenal, J. S. Williams, J. E. Bradby, T. C. Petersen, and A. Liu, "Dependence of short and intermediate-range order on preparation in experimental and modeled pure a-si," *Journal of Non-Crystalline Solids*, vol. 438, pp. 26–36, 2016.

[154] K. B. Borisenko, B. Haberl, A. C. Liu, Y. Chen, G. Li, J. S. Williams, J. E. Bradby, D. J. Cockayne, and M. M. Treacy, "Medium-range order in amorphous silicon investigated by constrained structural relaxation of two-body and four-body electron diffraction data," *Acta Materialia*, vol. 60, no. 1, pp. 359–375, 2012.

[155] M. Durandurdu, D. A. Drabold, and N. Mousseau, "Approximate ab initio calculations of electronic structure of amorphous silicon," *Physical Review B*, vol. 62, no. 23, p. 15307, 2000.

[156] P. Voyles, N. Zotov, S. Nakhmanson, D. Drabold, J. Gibson, M. Treacy, and P. Keblinski, "Structure and physical properties of paracrystalline atomistic models of amorphous silicon," *Journal of Applied Physics*, vol. 90, no. 9, pp. 4437–4451, 2001.

[157] N. Bernstein, J. Feldman, and M. Fornari, "Structural model of amorphous silicon annealed with tight binding," *Physical Review B*, vol. 74, no. 20, p. 205202, 2006.

[158] H. M. Shodja, M. Tabatabaei, and K. Esfarjani, "First principles molecular dynamics studies of elastic constants, ideal tensile strength, chemistry of crack initiation, and surface and cohesive energies in amorphous silicon," *Philosophical Magazine*, vol. 94, no. 25, pp. 2913–2936, 2014.

[159] E. Yablonovitch, T. Gmitter, R. Swanson, and Y. Kwark, "A 720 mv open circuit voltage sio x: c-si: Sio x double heterostructure solar cell," *Applied Physics Letters*, vol. 47, no. 11, pp. 1211–1213, 1985.

[160] W. Peter *et al.*, *Physics of Solar Cells: From Principles to New Concepts*. John Wiley & Sons, 2008.

[161] M. E. Stückelberger, "Hydrogenated amorphous silicon: Impact of process conditions on material properties and solar cell efficiency," *École Polytech Fédérale De Lausanne*, 2014.

[162] T. Brown, C. Bittencourt, M. Sebastiani, and F. Evangelisti, "Electronic states and band lineups in c-si (100)/a-si 1- x c x: H heterojunctions," *Physical Review B*, vol. 55, no. 15, p. 9904, 1997.

[163] A. Fantoni, Y. Vigranenko, M. Fernandes, R. Schwarz, and M. Vieira, "Influence of the band offset on the performance of photodevices based on the c-si/a-si: H heterostructure," *Thin Solid Films*, vol. 383, no. 1, pp. 314–317, 2001.

[164] S. Gall, R. Hirschauer, M. Kolter, and D. Bräunig, "Spectral characteristics of a-si: Hc-si heterostructures," *Solar energy materials and solar cells*, vol. 49, no. 1, pp. 157–162, 1997.

[165] M. Schmidt, L. Korte, A. Laades, R. Stangl, C. Schubert, H. Angermann, E. Conrad, and K. Maydell, "Physical aspects of a-si: H/c-si hetero-junction solar cells," *Thin Solid Films*, vol. 515, no. 19, pp. 7475–7480, 2007.

[166] W. van Sark, L. Korte, and F. Roca, *Physics and technology of amorphous-crystalline heterostructure silicon solar cells*. Springer, 2012.

[167] M. Peressi, L. Colombo, and S. de Gironcoli, "Role of defects in the electronic properties of amorphous/crystalline si interface," *Physical Review B*, vol. 64, no. 19, p. 193303, 2001.

[168] J. Custer, M. O. Thompson, D. Jacobson, J. Poate, S. Roorda, W. Sinke, and F. Spaepen, "Density of amorphous si," *Applied Physics Letters*, vol. 64, no. 4, pp. 437–439, 1994.

[169] I. Stich, R. Car, and M. Parrinello, "Amorphous silicon studied by ab initio molecular dynamics: Preparation, structure, and properties," *Physical Review B*, vol. 44, pp. 11 092–11 104, 1991.

[170] K. W. Böer, *Handbook of the physics of thin-film solar cells*. Springer Science & Business, 2014.

[171] J. Shi, H. Cui, Z. Liang, X. Lu, Y. Tong, C. Su, and H. Liu, "The roles of defect states in photoelectric and photocatalytic processes for zn x cd 1- x s," *Energy & Environmental Science*, vol. 4, no. 2, pp. 466–470, 2011.

[172] J. Nowotny, "Titanium dioxide-based semiconductors for solar-driven environmentally friendly applications: impact of point defects on performance," *Energy & Environmental Science*, vol. 1, no. 5, pp. 565–572, 2008.

[173] M. K. Nowotny, L. R. Sheppard, T. Bak, and J. Nowotny, "Defect chemistry of titanium dioxide. application of defect engineering in processing of tio2-based photocatalysts," *The Journal of Physical Chemistry C*, vol. 112, no. 14, pp. 5275–5300, 2008.

[174] C. Janet, S. Navaladian, B. Viswanathan, T. Varadarajan, and R. Viswanath, "Heterogeneous wet chemical synthesis of superlattice-type hierarchical zno architectures for concurrent h2 production and n2 reduction," *The Journal of Physical Chemistry C*, vol. 114, no. 6, pp. 2622–2632, 2010.

[175] P.-T. Hsiao, Y.-L. Tung, and H. Teng, "Electron transport patterns in tio2 nanocrystalline films of dye-sensitized solar cells," *The Journal of Physical Chemistry C*, vol. 114, no. 14, pp. 6762–6769, 2010.

[176] J. V. Li, R. S. Crandall, I. L. Repins, A. M. Nardes, and D. H. Levi, "Applications of admittance spectroscopy in photovoltaic devices beyond majority-carrier trapping defects," in *Photovoltaic Specialists Conference (PVSC), 2011 37th IEEE*. IEEE, 2011, pp. 000 075–000 078.

[177] H.-S. Duan, H. Zhou, Q. Chen, P. Sun, S. Luo, T.-B. Song, B. Bob, and Y. Yang, "The identification and characterization of defect states in hybrid organic–inorganic perovskite photovoltaics," *Physical Chemistry Chemical Physics*, vol. 17, no. 1, pp. 112–116, 2015.

[178] Y. Liu, P. Stradins, H. Deng, J. Luo, and S.-H. Wei, "Suppress carrier recombination by introducing defects: The case of si solar cell," *Applied Physics Letters*, vol. 108, no. 2, p. 022101, 2016.

[179] P. Muralidharan, D. Vasileska, S. M. Goodnick, and S. Bowden, "A kinetic monte carlo approach to study transport in amorphous silicon/crystalline silicon hit cells," in *Photovoltaic Specialist Conference (PVSC), 2015 IEEE 42nd*. IEEE, 2015, pp. 1–4.

[180] J. Kunstmann, T. B. Wendumu, and G. Seifert, "Localized defect states in mos2 monolayers: Electronic and optical properties," *physica status solidi (b)*, vol. 254, no. 4, 2017.

[181] T. B. Ngwenya, A. Ukpong, and N. Chetty, "Defect states of complexes involving a vacancy on the boron site in boronitrene," *Physical Review B*, vol. 84, no. 24, p. 245425, 2011.

[182] I. Santos, M. Cazzaniga, G. Onida, and L. Colombo, "Atomistic study of the structural and electronic properties of a-si: H/c-si interfaces," *Journal of Physics: Condensed Matter*, vol. 26, no. 9, p. 095001, 2014.

[183] A. Neumüller, O. Sergeev, S. J. Heise, S. Bereznev, O. Volobujeva, J. F. L. Salas, M. Vehse, and C. Agert, "Improved amorphous silicon passivation layer for heterojunction solar cells with post-deposition plasma treatment," *Nano Energy*, vol. 43, pp. 228–235, 2018.

[184] C.-K. Tan and N. Tansu, "First-principle natural band alignment of gan/dilute-as ganas alloy," *AIP Advances*, vol. 5, no. 1, p. 017129, 2015.

[185] M. Umeno, T. Soga, K. Baskar, and T. Jimbo, "Heteroepitaxial technologies on si for high-efficiency solar cells," *Solar energy materials and solar cells*, vol. 50, no. 1-4, pp. 203–212, 1998.

[186] S. R. Kurtz, P. Faine, and J. Olson, "Modeling of two-junction, series-connected tandem solar cells using top-cell thickness as an adjustable parameter," *Journal of Applied Physics*, vol. 68, no. 4, pp. 1890–1895, 1990.

[187] T. J. Grassman, C. Ratcliff, A. M. Carlin, J. A. Carlin, L. Yang, M. J. Mills, and S. A. Ringel, "Iii-v/gap epitaxy on si for advanced photovoltaics and green light emitters," *ECS Transactions*, vol. 50, no. 9, pp. 321–332, 2013.

[188] H. Wagner, T. Ohrdes, A. Dastgheib-Shirazi, B. Puthen-Veettil, D. König, and P. P. Altermatt, "A numerical simulation study of gallium-phosphide/silicon heterojunction passivated emitter and rear solar cells," *Journal of Applied Physics*, vol. 115, no. 4, p. 044508, 2014.

[189] M. Sobolev, A. Lazarenko, E. Nikitina, E. Pirogov, A. Gudovskikh, and A. Y. Egorov, "Mbe growth of gap on a si substrate," *Semiconductors*, vol. 49, no. 4, pp. 559–562, 2015.

[190] H. Kawanami, "Heteroepitaxial technologies of iii–v on si," *Solar Energy Materials and Solar Cells*, vol. 66, no. 1-4, pp. 479–486, 2001.

[191] S. Limpert, K. Ghosh, H. Wagner, S. Bowden, C. Honsberg, S. Goodnick, S. Bremner, A. Ho-Baillie, and M. Green, "Results from coupled optical and electrical sentaurus tcad models of a gallium phosphide on silicon electron carrier selective contact solar cell," in *Photovoltaic Specialist Conference (PVSC), 2014 IEEE 40th.* IEEE, 2014, pp. 0836–0840.

[192] C. Zhang, N. N. Faleev, L. Ding, M. Boccard, M. Bertoni, Z. Holman, R. R. King, and C. B. Honsberg, "Hetero-emitter gap/si solar cells with high si bulk lifetime," in *2016 IEEE 43rd Photovoltaic Specialists Conference (PVSC).* IEEE, 2016, pp. 1950–1953.

[193] V. Narayanan, S. Mahajan, N. Sukidi, K. Bachmann, V. Woods, and N. Dietz, "Orientation mediated self-assembled gallium phosphide islands grown on silicon," *Philosophical Magazine A*, vol. 80, no. 3, pp. 555–572, 2000.

[194] H. Döscher, B. Borkenhagen, G. Lilienkamp, W. Daum, and T. Hannappel, "Iii–v on silicon: Observation of gallium phosphide anti-phase disorder by low-energy electron microscopy," *Surface Science*, vol. 605, no. 15-16, pp. L38–L41, 2011.

[195] C. Zhang, Y. Kim, N. N. Faleev, and C. B. Honsberg, "Improvement of gap crystal quality and silicon bulk lifetime in gap/si heteroepitaxy," *Journal of Crystal Growth*, vol. 475, pp. 83–87, 2017.

[196] O. Romanyuk, T. Hannappel, and F. Grosse, "Atomic and electronic structure of gap/si (111), gap/si (110), and gap/si (113) interfaces and superlattices studied by density functional theory," *Physical Review B*, vol. 88, no. 11, p. 115312, 2013.

[197] M. Pashley, "Electron counting model and its application to island structures on molecular-beam epitaxy grown gaas (001) and znse (001)," *Physical Review B*, vol. 40, no. 15, p. 10481, 1989.

[198] W. Harrison, E. Kraut, J. Waldrop, and R. Grant, "Polar heterojunction interfaces," *Physical Review B*, vol. 18, no. 8, p. 4402, 1978.

[199] D. Bylander and L. Kleinman, "Huge electric fields in ge/gaas (001) and (111) superlattices and their effect on interfacial stability," *Physical Review B*, vol. 41, no. 6, p. 3509, 1990.

[200] O. Romanyuk, O. Supplie, T. Susi, M. May, and T. Hannappel, "Ab initio density functional theory study on the atomic and electronic structure of gap/si (001) heterointerfaces," *Physical Review B*, vol. 94, no. 15, p. 155309, 2016.

[201] M. Di Ventra, C. Berthod, and N. Binggeli, "Heterovalent interlayers and interface states: An ab initio study of ga as/ si/ ga as (110) and (100) heterostructures," *Physical Review B*, vol. 71, no. 15, p. 155324, 2005.

[202] T. Saito and T. Ikoma, "Role of interface states in band structures of short-period (gaas) n/(ge 2) n [001] superlattices under a zero-field model," *Physical Review B*, vol. 45, no. 4, p. 1762, 1992.

[203] J. Pollmann and S. T. Pantelides, "Electronic structure of the ge-gaas and ge-znse (100) interfaces," *Physical Review B*, vol. 21, no. 2, p. 709, 1980.

[204] T. Yasuda, "Interface, surface and bulk anisotropies of heterostructures," *Thin Solid Films*, vol. 313, pp. 544–551, 1998.

[205] G. Margaritondo, F. Cerrina, C. Capasso, F. Patella, P. Perfetti, C. Quaresima, and F. Grunthaner, "Znse ge heterojunction interface states in the energy region of the valence band discontinuity," *Solid state communications*, vol. 52, no. 5, pp. 495–498, 1984.

[206] M. Peressi, F. Favot, G. Cangiani, and A. Baldereschi, "Interface states at znse/ge heterojunctions: the role of atomic interdiffusion and disorder," *Applied physics letters*, vol. 81, no. 27, pp. 5171–5173, 2002.

[207] P. Mehr, X. Zhang, W. Lepkowski, C. Li, and T. J. Thornton, "Soi mesfets on high-resistivity, trap-rich substrates," *Solid-State Electronics*, vol. 142, pp. 47–51, 2018.

[208] A. Beyer, J. Ohlmann, S. Liebich, H. Heim, G. Witte, W. Stolz, and K. Volz, "Gap heteroepitaxy on si (001): Correlation of si-surface structure, gap growth conditions, and si-iii/v interface structure," *Journal of Applied Physics*, vol. 111, no. 8, p. 083534, 2012.

[209] S. L. Wright, H. Kroemer, and M. Inada, "Molecular beam epitaxial growth of gap on si," *Journal of applied physics*, vol. 55, no. 8, pp. 2916–2927, 1984.

[210] A. Goetzberger, E. Klausmann, and M. Schulz, "Interface states on semiconductor/insulator surfaces," *Critical Reviews in Solid State and Material Sciences*, vol. 6, no. 1, pp. 1–43, 1976.

[211] M. Ishii and Y. Taga, "Time-of-flight scattering and recoiling spectrometry study of plasma-cleaned silicon surface," *Japanese journal of applied physics*, vol. 33, no. 7S, p. 4186, 1994.

[212] C. B. Park, T. Yokoyama, T. Nishimura, K. Kita, and A. Toriumi, "Molecular ordering and interface state modification for reducing bias-induced threshold voltage shift in pentacene field-effect transistors," *Journal of the Electrochemical Society*, vol. 155, no. 8, pp. H575–H581, 2008.

[213] W. Kao, A. Ali, E. Hwang, S. Mookerjea, and S. Datta, "Effect of interface states on sub-threshold response of iii–v mosfets, mos hemts and tunnel fets," *Solid-State Electronics*, vol. 54, no. 12, pp. 1665–1668, 2010.

[214] M. Wu, Z. Han, and V. Van, "Conductor-gap-silicon plasmonic waveguides and passive components at subwavelength scale," *Optics Express*, vol. 18, no. 11, pp. 11 728–11 736, 2010.

[215] A. Murakoshi, M. Iwase, H. Niiyama, M. Tomita, and K. Suguro, "Improvement of p–n junction leakage and reduction in interface state density in transistors by cryo implantation technology," *Japanese Journal of Applied Physics*, vol. 52, no. 10R, p. 105501, 2013.

[216] A. Murakoshi, M. Iwase, H. Niiyama, M. Koike, and K. Suguro, "Reduction of surface roughness and defect density by cryogenic implantation of arsenic," *Japanese Journal of Applied Physics*, vol. 53, no. 6, p. 066507, 2014.

[217] P. Stradins, S. Essig, W. Nemeth, B. Lee, D. Young, A. Norman, Y. Liu, J. Luo, E. Warren, A. Dameron *et al.*, "Passivated tunneling contacts to n-type wafer silicon and their implementation into high performance solar cells," *Technical Digest WCPEC-6*, 2014.

[218] J. I. Pankove and N. M. Johnson, *Hydrogen in semiconductors*. Academic press, 1991.

[219] J. Lyons and C. Van de Walle, "Surprising stability of neutral interstitial hydrogen in diamond and cubic bn," *Journal of Physics: Condensed Matter*, vol. 28, no. 6, p. 06LT01, 2016.

[220] C. G. Van de Walle and J. Neugebauer, "Universal alignment of hydrogen levels in semiconductors, insulators and solutions," *Nature*, vol. 423, no. 6940, pp. 626–628, 2003.

[221] J. Goss, R. Jones, M. Heggie, C. Ewels, P. Briddon, and S. Öberg, "Theory of hydrogen in diamond," *Physical Review B*, vol. 65, no. 11, p. 115207, 2002.

[222] L. Wang and A. Zunger, "Phosphorus and sulphur doping of diamond," *Physical Review B*, vol. 66, no. 16, p. 161202, 2002.

[223] P. Giannozzi, S. Baroni, N. Bonini, M. Calandra, R. Car, C. Cavazzoni, D. Ceresoli, G. L. Chiarotti, M. Cococcioni, I. Dabo *et al.*, "Quantum espresso: a modular and open-source software project for quantum simulations of materials," *Journal of Physics: Condensed Matter*, vol. 21, no. 39, p. 395502, 2009.

[224] A. Kley and J. Neugebauer, "Atomic and electronic structure of the gaas/znse (001) interface," *Physical Review B*, vol. 50, no. 12, p. 8616, 1994.

[225] W. E. Pickett, S. G. Louie, and M. L. Cohen, "Self-consistent calculations of interface states and electronic structure of the (110) interfaces of ge-gaas and alas-gaas," *Physical Review B*, vol. 17, no. 2, p. 815, 1978.

[226] A. Baldereschi, S. Baroni, and R. Resta, "Band offsets in lattice-matched heterojunctions: a model and first-principles calculations for gaas/alas," *Physical review letters*, vol. 61, no. 6, p. 734, 1988.

[227] P. Laszlo, "A diborane story," *Angewandte Chemie International Edition*, vol. 39, no. 12, pp. 2071–2072, 2000.

[228] Y. Ping Wang, J. Stodolna, M. Bahri, J. Kuyyalil, T. Nguyen Thanh, S. Almosni, R. Bernard, R. Tremblay, M. Da Silva, A. Letoublon *et al.*, "Abrupt gap/si hetero-interface using bistepped si buffer," *Applied Physics Letters*, vol. 107, no. 19, p. 191603, 2015.

[229] I. Lucci, S. Charbonnier, L. Pedesseau, M. Vallet, L. Cerutti, J.-B. Rodriguez, E. Tournié, R. Bernard, A. Létoublon, N. Bertru *et al.*, "Universal description of iii-v/si epitaxial growth processes," *Physical Review Materials*, vol. 2, no. 6, p. 060401, 2018.

[230] P. Kumar and C. H. Patterson, "Dielectric anisotropy of the gap/si (001) interface from first-principles theory," *Physical review letters*, vol. 118, no. 23, p. 237403, 2017.

[231] C. Zhang, A. Boley, N. Faleev, D. J. Smith, and C. B. Honsberg, "Investigation of defect creation in gap/si (0 0 1) epitaxial structures," *Journal of Crystal Growth*, vol. 503, pp. 36–44, 2018.

[232] I. Sakata and H. Kawanami, "Band discontinuities in gallium phosphide/crystalline silicon heterojunctions studied by internal photoemission," *Applied physics express*, vol. 1, no. 9, p. 091201, 2008.

[233] R. Roychowdhury, S. Kumar, A. Wadikar, C. Mukherjee, K. Rajiv, T. Sharma, and V. Dixit, "Role of surface energy on the morphology and optical properties of gap micro & nano structures grown on polar and non-polar substrates," *Applied Surface Science*, vol. 419, pp. 957–967, 2017.

[234] R. Saive, C. Chen, H. Emmer, and H. Atwater, "Gap/si heterojunction solar cells," California Institute of Technology, Tech. Rep., 2015.

[235] O. Supplie, M. M. May, G. Steinbach, O. Romanyuk, F. Grosse, A. Nagelein, P. Kleinschmidt, S. Bruckner, and T. Hannappel, "Time-resolved in situ spectroscopy during formation of the gap/si (100) heterointerface," *The journal of physical chemistry letters*, vol. 6, no. 3, pp. 464–469, 2015.

[236] K. Ishioka, K. Brixius, A. Beyer, A. Rustagi, C. J. Stanton, W. Stolz, K. Volz, U. Höfer, and H. Petek, "Coherent phonon spectroscopy characterization of electronic bands at buried semiconductor heterointerfaces," *Applied Physics Letters*, vol. 108, no. 5, p. 051607, 2016.

[237] C. Zhang, E. Vadiee, R. R. King, and C. B. Honsberg, "Carrier-selective contact gap/si solar cells grown by molecular beam epitaxy," *Journal of Materials Research*, vol. 33, no. 4, pp. 414–423, 2018.

[238] M. Feifel, T. Rachow, J. Benick, J. Ohlmann, S. Janz, M. Hermle, F. Dimroth, and D. Lackner, "Gallium phosphide window layer for silicon solar cells," *IEEE Journal of Photovoltaics*, vol. 6, no. 1, pp. 384–390, 2016.

[239] T. Grassman, J. Carlin, B. Galiana, F. Yang, M. Mills, and S. Ringel, "Mocvd-grown gap/si subcells for integrated iii–v/si multijunction photovoltaics," *IEEE Journal of Photovoltaics*, vol. 4, no. 3, pp. 972–980, 2014.

[240] M. Feifel, J. Ohlmann, J. Benick, T. Rachow, S. Janz, M. Hermle, F. Dimroth, J. Belz, A. Beyer, K. Volz *et al.*, "Movpe grown gallium phosphide–silicon heterojunction solar cells," *IEEE J. Photovolt.*, vol. 7, no. 2, p. 502, 2017.